

Nanosilicon anodes for high performance rechargeable batteries

Zheng-Long Xu^{1,4}, Xianming Liu², Yongsong Luo³, Limin Zhou⁴ and Jang-Kyo Kim^{1*}

¹Department of Mechanical and Aerospace Engineering, The Hong Kong University of Science and Technology, Clear Water Bay, Kowloon, Hong Kong, China

²College of Chemistry and Chemical Engineering, Luoyang Normal University, Luoyang 471022, China

³Key Laboratory of Advanced Micro/Nano Functional Materials, Xinyang Normal University, Xinyang 464000, China

⁴Department of Mechanical Engineering, The Hong Kong Polytechnic University, Hung Hom, Hong Kong, China

Abstract

Taking advantage of an extremely high theoretical capacity of 4200 mAhg^{-1} , silicon has been considered one of the most promising anode materials for lithium ion batteries. Nevertheless, it also has many challenging issues, such as large volume expansion, poor electrical conductivity and the formation of unstable solid electrolyte *interphase* layers. To address these challenges, much effort has been directed towards developing new strategies, such as designing novel nanosilicon and hybridizing with other functional materials. This paper is dedicated to identifying the current state-of-the-art fabrication methods of nanosilicon, including ball milling, chemical vapor deposition, metal-assisted chemical etching and magnesiothermic reduction, as well as the design principles and the selection criteria for fabricating high performance Si nanostructures. The critical factors determining the electrical conductivity, structural stability and active material content are elucidated as important criteria for designing Si-based composites. The structural evolution and reaction mechanisms of nanosilicon electrodes studied by *in situ* experiments are discussed, offering new insights into how advanced Si electrodes can be designed. Emerging applications of Si electrodes in

other rechargeable batteries, such as Li-S, Li-O₂ and Na-ion batteries are also summarized. The challenges encountered for future development of reliable Si electrodes for real-world applications are proposed.

Keywords: Nanosilicon, Li-ion storage, Fundamental understanding, Rechargeable batteries.

*Corresponding author: Email: mejkkim@ust.hk; Fax: +852-2358-1543; Tel: +852-2358-7207.

Contents

1. Introduction.....	7
1.1 Anodes for LIBs.....	7
1.2 Basic principles of Si and Si anodes	8
1.3 Opportunities and challenges of Si anodes	12
2. Methodologies to improve the electrochemical performance of Si anodes.....	14
2.1 Advantages of nanostructured electrode materials	14
2.2 Fabrication of nanostructured Si materials: methods to prepare nanosilicon	16
2.2.1 Ball milling	16
2.2.2 Chemical vapor deposition	17
2.2.3 Metal assisted chemical etching.....	21
2.2.4 Magnesiothermic reduction	23
2.2.5 Other approaches	28
2.2.6 Summary of fabrication methods and design principles of nanosilicon	30
2.3 Hybridization of nanosilicon with functional materials.....	32
2.3.1 Silicon/carbon composites	33

2.3.2 Silicon/conducting polymer composites	38
2.3.3 Silicon/metal (oxides) composites	39
2.3.4 Discussion on Si-based composite electrodes.....	41
2.4 Disadvantages of nanosilicon anodes and potential solutions	44
3. Fundamental understanding of Si anodes (based on <i>in-situ</i> experiments).....	45
3.1 <i>In-situ</i> transmission electron microscopy examination.....	46
3.1.1 Lithiation mechanisms	46
3.1.2 Lithiation kinetics	48
3.1.3 Effects of coating layers.....	49
3.1.4 Properties of lithiated silicon	51
3.2 Other <i>in-situ</i> techniques	53
3.2.1 <i>In-situ</i> atomic force microscopy	53
3.2.2 <i>In-situ</i> scanning electron microscopy	54
3.2.3 Other <i>in situ</i> techniques	55
4. Application of Si anodes in rechargeable batteries beyond LIBs	56
4.1 Li-sulfur batteries.....	56
4.2 Li-O ₂ batteries	58
4.3 Na-ion batteries	59
4.4 Remaining issues of Si anodes beyond LIBs	60
5. Perspectives of Si anodes for practical applications	62
6. Conclusions.....	66

Nomenclature

Acronyms

AFM	Atomic force microscope
a-Si	Amorphous silicon
BM	Ball milling
CE	Coulombic efficiency
CNF	Carbon nanofiber
CNT	Carbon nanotube
c-Si	Crystalline silicon
CTAB	Cetyltrimethylammonium bromide
CV	Cyclic voltammetry
CVD	Chemical vapor deposition
DFT	Density functional theory
DWSiNT	Double-walled Si-SiO _x nanotube
EC	Ethylene carbonate
EDS	Energy dispersive spectrometer
EIS	Electrochemical impedance spectroscopy
EV	Electric vehicle
FEC	Fluoroethylene carbonate
F-Si	Ferrosilicon
FTIR	Fourier transform infrared spectroscopy
G	Graphene
GF	Graphene foam
GO	Graphene oxide
ICE	Initial Coulombic efficiency
LIB	Li-ion battery
LOB	Li-O ₂ battery
LSB	Li-sulfur battery
LTO	Li ₄ Ti ₅ O ₁₂
MACE	Metal-assisted chemical etching
MR	Magnesiothermic reduction
M-Si	Metallurgical silicon

MWCNT	Multi-walled carbon nanotube
NF	Nanofiber
NMR	Nuclear magnetic resonance
NP	Nanoparticle
NS	Nanosphere
NT	Nanotube
NW	Nanowire
PAN	Polyacrylonitrile
PANi	Polyaniline
PC	Propylene carbonate
PEDOT:PSS	Poly(3,4-ethylenedioxythiophene) doped with poly(4-styrenesulfonate)
PPy	Polypyrrole
PS	Polystyrene
SEI	Solid electrolyte interphase
SEM	Scanning electron microscopy
SIB	Sodium-ion battery
SWCNT	Single-walled carbon nanotube
TCG-Si	Templated carbon bridged oriented graphene-silicon
TEOS	Tetraethyl orthosilicate
TEM	Transmission electron microscope
VLS	Vapor-liquid-solid
XPS	X-ray photoelectron spectroscopy
XRD	X-ray diffraction
0D	Zero dimensional
1D	One dimensional
2D	Two dimensional
3D	Three dimensional

Symbols

τ	Li ion diffusion time
L_{ion}	Li ion diffusion length
D_{ion}	Li ion diffusion coefficient
G	Energy release rate
E	Young's modulus
σ	Representative stress
Z	Dimensional number of order unity
h	Feature size of material

Γ	Fracture energy
ΔG_r	Gibbs free energy change of forming $1/x$ units of Li_xSi
ΔG_r^0	Neat Gibbs free energy change
φ	External voltage applied to Si anode
σ_m^{Si}	Mean stress induced by Si core
Ω^{Si}	Volume per Si atom
$\sigma_m^{\text{Li}_x\text{Si}}$	Mean stress induced by lithiated Si
$\Omega^{\text{Li}_x\text{Si}}$	Volume per unit of Li_xSi

1. Introduction

1.1 Anodes for LIBs

Graphite has been the dominant source of anode materials for rechargeable Li-ion batteries (LIBs) for more than two decades owing to its many useful characteristics, such as low working potential, excellent cyclic stability, low cost and environmental friendliness. Nevertheless, the capacities of commercial electrodes are far from sufficient, i.e. graphite anode with a theoretical capacity of 372 mAh g^{-1} and lithium metal oxide cathodes with capacities less than 250 mAh g^{-1} , to satisfy today's demanding and emerging applications. Sophisticated mobile electronics, electric vehicles (EVs) and large-scale energy storage smart grids require much higher gravimetric/volumetric energy and power densities, longer life span and lower costs than the current LIBs can offer [1,2]. Thus, significant research efforts have been made to identify alternative electrode materials that can satisfy the aforementioned demanding requirements.

Anode materials for LIBs can be divided into three different groups depending on the reaction process, namely the insertion, conversion and alloying reactions [3,4], as summarized in Fig. 1. (i) The first group of electrode materials involves insertion where Li ions are intercalated into the d-spacing lattices of graphite or TiO_2 without causing pronounced volume changes of the hosts. The insertion of Li ions into the spinel $\text{Li}_4\text{Ti}_5\text{O}_{12}$ (LTO) transforms to rock-salt type $\text{Li}_7\text{Ti}_5\text{O}_{12}$ with about zero strain but a low specific capacity of 175 mAh g^{-1} . (ii) The electrode materials in the conversion group undergo a reversible reduction/oxidation process in the presence of Li ions. Anodes made from the transition metal oxides, such as Fe_3O_4 , FeO , Co_3O_4 and NiO , can exhibit both highly reversible capacities and high energy densities [5,6]. However, they have disadvantages of low initial Coulombic efficiencies, unstable solid electrolyte interphase (SEI) layers, poor cyclic stability due to the large volume expansion, large potential hysteresis and poor

electronic/ionic conductivities [7]. (iii) The typical electrode materials in the third group (**not the group III in the periodic table**) are metals to **which Li ions are electrochemically inserted** to form compound phases upon lithiation. The anode materials in this group, like Si, Sn, Ge, **Al, Mg and Sb**, are known for their extremely high capacities, especially compared to those in the insertion group. They have moderate operational potentials vs Li/Li⁺, which can avert the safety concern arising from the formation of Li dendrites and the energy penalty of battery cells [8]. The main challenge to the implementation of these anodes is their huge volume expansion occurring during the lithiation process [9]. The discharge/charge mechanisms of crystalline Si (c-Si) is schematically illustrated in Fig. 1 as an example for this group, showing that the c-Si undergoes large volume expansion and destroys the crystal structure during lithiation and transfers to amorphous Si (a-Si) upon delithiation, to be discussed later. Table 1 presents the comparison of electrochemical properties of different active materials in the three groups based on their reaction processes. The comparison unequivocally reveals that Si boasts the highest theoretical specific capacity of 4200 mAh g⁻¹ among all candidate materials, stimulating widespread research for real world applications.

1.2 Basic principles of Si and Si anodes

Si. The history of element Si can be traced back to 1823 when pure a-Si was prepared by purifying K₂SiF₆ in the warm potassium through exhaust filtering. In 1854, c-Si was first prepared by electrolysis of impure sodium-aluminum chloride with about 10 % Si. Later, large-scale production of c-Si was realized for commercial application by reducing silica with carbon at ~3000 °C [10]. c-Si possesses a diamond cubic close-packed structure (in Fd $\bar{3}$ m space group), which is similar to two identical face-centered cubic structure shifted along the bulk diagonal by 1/4 of its length. The lattice constant of a unit cell is 5.4307 Å and the Si-Si bond length is 2.3517 Å, as shown in Fig. 2a [10]. Fig. 2b presents the c-Si lattice along the <100>, <110> and <111> crystallographic directions, which are the origin of anisotropic

chemicophysical properties of Si materials [11]. Si is an intrinsic semiconductor with a band gap of 1.12 eV and an electrical conductivity of $\sim 10^{-3}$ S cm⁻¹ at room temperature. The conductivity of Si is sensitive to its chemical structure and can be effectively adjusted by introducing heteroatoms, in the so-called “doping” process. A Si atom has four valence electrons to form valence bonds with nearby Si atoms. When a Si atom is replaced with a phosphorus atom (in Column V of periodic table), the doped Si is designated as N-type with extra negative electrons (Fig. 2c) and the other kind is P-type with extra positive holes (Fig. 2d) if Si is doped with elements like boron in Column III [12]. The conductivities and band gaps of doped Si can be tuned by changing the type and concentration of heteroatoms. The doped Si was used to fabricate porous Si by chemical etching and the correlation between lithiation kinetics and conductivity of Si nanowires (NWs) was studied by adjusting the dopant concentrations, to be discussed later. With these intriguing chemicophysical properties, Si has been extensively studied and widely applied in many fields, like transistors, integrated circuits, diodes, solar cells and energy storage systems [10]. In this review, we mainly focus on the application of Si in rechargeable batteries.

Si anodes. By heat treatment, the mixture of Li and Si can form a range of crystalline intermediates: namely, LiSi, Li₁₂Si₇, Li₁₃Si₄ and Li₂₂Si₅. They are shown in the phase diagram of Li-Si in Fig. 3a, which is the foundation of Si anodes [13,14]. These crystalline intermediates were formed step by step upon lithiation of Si at 450 °C (Fig. 3b) [15]. The crystalline Li₂₂Si₅ (c-Li₂₂Si₅) was supposed to be the final product whose theoretical specific capacity was calculated to be ~ 4200 mAh g⁻¹. Table 2 shows that upon lithiation, Si suffers continuous volume expansion at different stages to reach a very high value of ~ 300 % [16]. The huge volume expansion would cause many deficiencies in the Si electrodes, to be discussed later. When the c-Si electrodes are electrochemically reacted with Li at room temperature, it undergoes a smooth crystalline-amorphous phase transition (Fig. 3b), different

from the formation of crystalline intermediates through a step-by-step process at a high temperature. To understand above interesting difference, the Gibbs free energy changes required to form the crystalline and amorphous (Li, Si) compounds were calculated by the density functional theory (DFT) [17]. It is revealed that the formation of amorphous Li_xSi was preferred by electrochemically-driven solid-state amorphization, while the formation of equilibrium crystalline phases was kinetically inhibited at room temperature [18]. The final lithiation product obtained at room temperature was $\text{Li}_{15}\text{Si}_4$ with a specific capacity of 3579 mAh g^{-1} , not $\text{Li}_{22}\text{Si}_5$, as confirmed by many reports [18–21].

The electrochemically-driven solid-state amorphization and the phase evolution of Si electrodes during lithiation/delithiation processes have been investigated by *in-situ* and *ex-situ* X-ray diffraction (XRD) techniques [19,21]. It is noted that during the first lithiation, the c-Si converted gradually into the amorphous Li_xSi although it coexisted as discharge potential reducing. When the potential was maintained at ~ 60 mV, the amorphous $\text{Li}_{15}\text{Si}_4$ (a- $\text{Li}_{15}\text{Si}_4$) was formed, which was then transformed to the crystalline $\text{Li}_{15}\text{Si}_4$ (c- $\text{Li}_{15}\text{Si}_4$) immediately after the potential was lower than 60 mV. Upon delithiation, the c- $\text{Li}_{15}\text{Si}_4$ transformed into an a-Si, not the original c-Si. In the following cycles, only reversible transition occurred between a-Si and $\text{Li}_{15}\text{Si}_4$ (Figs. 1c and 3c) [19]. From the fundamental activation energy viewpoint, the solid-state amorphization process of the original c-Si was driven by the large activation energy required to destroy the Si-Si bonds, which was described as an ‘edge peeling-off mechanism’, according to an atomic scale *in-situ* transmission electron microscope (TEM) examination [22]. In addition, the a- $\text{Li}_{15}\text{Si}_4$ to c- $\text{Li}_{15}\text{Si}_4$ transition below 60 mV was a spontaneous, congruent process without a long-range atomic diffusion or phase separation, unlike the classical nucleation and growth mechanisms [17].

On an atomic scale, the lithiation process of c-Si can be seen as the breakage of Si-Si networks by Li. The whole lithiation process can be divided into three stages (Fig. 3d) [11]:

namely, (i) accumulation of Li, (ii) breaking of Si-Si bonds and (iii) dissolving of Si segments. It is reported that Li preferentially diffused along the [111] direction to accumulate at the tetrahedral sites which are the most stable positions for Li insertion [23]. When the relative concentration of Li: Si reached around 0.5, the Si-Si bonds became weakened and eventually eroded by Li [24]. In an *ab initio* molecular dynamics study, the c-Si was depicted as containing 6-node rings and the breaking of Si-Si bonds in the 6 node rings created ephemeral structures or Si segments, such as stars and boomerangs. They were gradually dissociated into smaller segments, like Si-Si dumbbells and isolated Si atoms, in the amorphous Li_xSi phase [25]. These disconnected Si atoms were embedded in a dense, amorphous structure of Li atoms in a- $\text{Li}_{15}\text{Si}_4$. Because the local order of Si in a- $\text{Li}_{15}\text{Si}_4$ resembled the environment for Si atoms in c- $\text{Li}_{15}\text{Si}_4$, the transition between amorphous to crystalline $\text{Li}_{15}\text{Si}_4$ became kinetically easy [25,26], in agreement with the above statement. The lithiation mechanism of Si involves destroying the crystalline structure of Si host and the insertion of 3.75 Li ions per Si atom, which is different from the intercalation of only one Li ion into one carbon ring (C_6) with 6 carbon atoms for graphite. Such a fundamental difference provides evidence for the extremely high specific capacity and huge volume expansion of Si anodes over the commercial graphite anodes.

To measure the electrochemical properties of Si anodes, a typical LIB cell is usually assembled in an Ar-filled glove box using Li foil or lithium metal oxide as the counter cathode, polyethylene as the separator and 1M LiPF_6 dissolved in ethyl carbonate: dimethyl carbonate (EC: DMC 1/1= v/v) solvent as the electrolyte. During discharge, Li ions are released from the cathode and transported through the separator to react with the Si anode. When the potential is below 1.0 V vs Li/Li^+ , the organic electrolyte can easily decompose to form a passive layer on the electrode surface, the so-called SEI layer [27]. The SEI layer consists mainly of Li_2CO_3 , LiF, Li_2O and various lithium alkyl carbonates, as analyzed by

high resolution TEM (HRTEM), Fourier transform infrared spectroscopy (FTIR) and X-ray photoelectron spectroscopy (XPS) techniques [28–30]. The passive layer is electronically insulating and ionically conductive, preventing the occurrence of further side reactions of liquid electrolyte. Therefore, it is important to maintain stable SEI layers during cycles to ensure high Coulombic efficiencies and long cycle life of electrodes. The specific capacity, life span, gravimetric/volumetric energy density and Coulombic efficiency are among the most important parameters that evaluate the performance of a battery comprising Si-based anodes [31].

1.3 Opportunities and challenges of Si anodes

Si anode has long been identified as one of the most promising candidates for next-generation LIBs due to their many attractive features [32–34], as follows. (i) Si is the 2nd most abundant element (~28 wt.%) after oxygen in the earth crust and is environmentally friendly. (ii) The large-scale production of Si is not an issue in view of the matured semiconductor industries. (iii) Si presents the highest ever known theoretical specific capacity of 3579 mAh g⁻¹ and a volumetric capacity of 8322 mAh cm⁻³ at room temperature, which are ten times higher than those of commercial graphite anodes, 372 mAh g⁻¹ and 818 mAh cm⁻³, respectively. (iv) The operation potential of Si anodes is ~370 mV vs Li/Li⁺, leading to a high energy density and safe operation of the batteries.

Despite these exciting advantages, however, the large-scale implementation of Si anodes has been significantly retarded by their poor cyclic stability and low rate capacities. The fundamental challenges of Si-based anodes are summarized in Fig. 4 in terms of three major failure mechanisms [14,30,31]. (i) The huge volume expansion of ~300 % of Si upon full lithiation can cause cracking and eventual pulverization after repeated charge/discharge cycles (Fig. 4a). During delithiation, the volume contraction results in electrical isolation of active particles from the conductive network (Fig. 4b) and separation of the electrode from

the current collector, causing drastic capacity degradation and failure of the electrodes. (ii) The electrical conductivity and ion diffusion coefficient of Si particles are $\sim 10^{-3} \text{ S cm}^{-1}$ and $10^{-12} \text{ cm}^2 \text{ s}^{-1}$, respectively [35]. The sluggish charge transfer kinetics arising from the poor electronic conduction and ion diffusion prevent full utilization of the active material Si, especially at high current densities. (iii) The SEI layer would continuously accumulate on the surface of Si electrode after many cycles. In particular, the large volume expansion/contraction of Si causes fracture and re-formation of SEI layers on the Si surface (Fig. 4c), leading to the consumption of electrolyte, long Li diffusion path, degraded electronic conduction of active materials, poor Coulombic efficiencies and eventual battery failure.

Tremendous efforts have been made in the past two decades to mitigate the aforementioned major challenges aiming for the commercialization of Si electrodes. As a consequence, significant scientific advances and technological breakthroughs in terms of both fundamental understanding and nanostructural fabrication have been reported. This is partly proven by the exponential growth in the number of publications and citations directly relevant to Si anodes: for example, the publication/citation number has increased from 50/217 in 1996 to 777/26381 in 2016, respectively, according to Web of Science. This paper is aimed to summarize and critically review the recent state-of-the-art advances of silicon-based anodes, especially those on the nanoscale, for high-capacity rechargeable batteries. Particular emphasis has been placed to highlight and thoroughly discuss the representative approaches employed to synthesize nanosilicon, such as ball milling (BM), chemical vapor deposition (CVD), metal-assisted chemical etching (MACE) and magnesiothermic reduction (MR). Although there are many papers dedicated to reviewing the Si-based anode materials [37–47], very few of them specifically explained the synthesis processes and their influences on electrochemical performance of the Si anodes. The implications and effects of modifications made by

assembling nanosilicon with other functional materials, such as carbonaceous materials, conducting polymers and metal (oxides), on electrochemical performance are also discussed. A discernible progress has been achieved to enrich fundamental understanding of the reaction mechanisms and kinetics taking place during the charge/discharge cycles using *in-situ* techniques, such as *in-situ* TEM [48,49]. The recent progress has not been duly reviewed [50,51], which will be one of important subjects of this paper. Finally, the potential applications of nanosilicon electrodes in other rechargeable batteries with high energy densities, like lithium sulfur, lithium oxygen and sodium ion batteries (LSBs, LOBs and SIBs), are outlined along with the discussion on other issues we are facing for large-scale and practical applications of Si electrodes.

2. Methodologies to improve the electrochemical performance of Si anodes

2.1 Advantages of nanostructured electrode materials

The electrochemical performance of electrode materials depends not only on their intrinsic electrochemical properties, such as Li storage mechanisms and theoretical capacity, but also on their materials characteristics, such as particle size and electrical conductivity. It has been proven that downsizing active materials has significant positive influences on improving electrochemical properties of the electrodes by ameliorating (i) the Li ion diffusion kinetics, (ii) the fracture tolerance of electrodes and (iii) the stability of SEI layer [52]. The Li ion diffusion in electrode materials can be described as [53]:

$$\tau = L_{ion}^2 / D_{ion} \quad (1)$$

where τ is the diffusion time of Li ion in the host material, L_{ion} is Li ion diffusion length and D_{ion} is the Li ion diffusion coefficient. D_{ion} depends on the nature of the material while L_{ion} is determined by the size of electrode materials. Thereby, nanostructured materials can greatly reduce both the diffusion length and time for Li ion to react with the active materials, rendering high utilization of active materials at high current densities. In addition, nanomaterials also allow a large surface area in contact with the electrolyte, facilitating fast

charge transfer for a high rate capacity. During lithiation/delithiation, electrode materials in the alloy and conversion groups often suffer large volume changes, potentially causing cracking, fracture and pulverization of active particles. Whether an electrode material suffers fracture due to lithiation-induced stresses is closely related to the feature size of the electrode material [54]. During lithiation, the reduction in elastic energy associated with the crack advancing a unit area defines the energy release rate, G , which is given by [55]:

$$G = \frac{Z\sigma^2 h}{E} \quad (2)$$

where h is the feature size, E is the Young's modulus, σ is the representative stress and Z is a dimensional number of order unity. If G is below the fracture energy, Γ , of a material, preexisting cracks will not advance and fracture will not occur. By taking Γ into Eq. 2, we can obtain a critical particle size, h_c :

$$h_c = \frac{\Gamma E}{Z\sigma^2} \quad (3)$$

when the particle size of an electrode material is smaller than h_c , no fracture will happen, offering a fundamental evidence towards the high fracture resistance of nanostructured electrode materials. The critical sizes of c-Si and a-Si particle were determined to be 150 and 870 nm, respectively. Along with the volume expansion of active particles, the SEI layer formed on their surface may break and reform during cycles, leading to the consumption of electrolyte and thus extension of Li ion diffusion distance. Nanomaterials can offer a near static surface for more stable SEI formation than in large-size active materials. For example, Si particles encapsulated in hollow carbon spheres [56] or Fe₃O₄ nanocrystals embedded in mechanically robust carbon nanofibers (CNFs) [57] presented ultrastable SEI films and excellent cyclic stability.

In this way, nanoscale Si particles are expected to possess several distinct advantages over bulk counterparts arising from a few ameliorating characteristics. (i) Nanosilicon has a high fracture resistance to prevent materials from pulverization during cycles; (ii) nanosilicon possesses improved ion diffusion kinetics for high rate capability by providing large contact areas for electrolyte/electrode interface and short ion diffusion distance; and (iii) the

mechanical strains for SEI layers on the surface of nanosilicon can be effectively alleviated, ensuring high Coulombic efficiencies and excellent reversibility. A number of different Si nanostructures with excellent electrochemical properties have been prepared using various approaches. In the following, discussion is made of two sequential strategies devised to enhance the Li storage performance of Si-based anodes, namely the fabrication of nanostructured Si materials and the hybridization of nanosilicon with other functional materials.

2.2 Fabrication of nanostructured Si materials: methods to prepare nanosilicon

In order to exploit the advantages of nanostructured Si and realize widespread application of high performance Si anodes, many different forms of Si nanostructures have been prepared using various methods. Here, we will discuss the most representative approaches, including ball milling, chemical vapor deposition, metal-assisted chemical etching and magnesiothermic reduction. The principles of these four major methods and the electrochemical performance of the corresponding Si nanostructures made therefrom are summarized in [Tables 3](#) and [4](#), respectively.

2.2.1 Ball milling

Ball milling is a simple method to prepare Si nanoparticles (NPs) from bulk Si by taking advantage of the mechanical force of rolling balls, as schematically illustrated in [Table 3](#) [[58,59](#)]. The low-cost operation and the capability for large-scale production are the two main advantages of ball milling. For example, Si powders can be milled from low grade, microscale Si of 1-5 μm in diameter at a rate of ~ 100 kg per day [[60](#)]. The commercially available metallurgical Si (M-Si, with ~ 99 wt.% Si, priced at $\$1$ kg^{-1}) and ferrosilicon (F-Si, ~ 83 wt.% Si and ~ 13 wt.% Fe, priced at $\$0.6$ kg^{-1}) are normally used as feedstock [[61](#)]. Therefore, the total cost of Si NPs ball-milled from the raw Si sources is less than $\$2$ kg^{-1} [[60](#)], which is much cheaper than Si produced by CVD, as discussed below. As for the

electrochemical performance, the milled Si has useful microstructures and chemical compositions. It is reported that the abundant dislocations and grain boundaries generated during ball milling provided more ion diffusion channels and smoother phase transition than bulk Si particles, promoting structural stability and high rate capacities [60]. Unlike the Si NPs made from M-Si, the impurities of FeSi₂ in F-Si NPs served as the buffer to effectively accommodate the volume expansion of Si during lithiation, leading to a higher capacity of 1354 mAh g⁻¹ for F-Si than 980 mAh g⁻¹ for M-Si after 50 cycles at 0.4 A g⁻¹. The similarity in cyclic voltammetry (CV) curves between the M-Si and F-Si electrodes signifies that the FeSi₂ particles did not react with Li ions, thus maintaining their structural and chemical stability during charge/discharge cycles [61]. A major disadvantage of ball milling is that the resultant product has agglomerated, large rigid Si particles, which are deleterious to the stability of long-term cycles [62]. Creating pores by chemical etching and/or encapsulating milled Si particles with functional materials can be useful strategies to address the shortcoming.

2.2.2 Chemical vapor deposition

CVD is a popular bottom-up method to prepare various Si nanostructures [35]. The growth mechanism of Si NWs by CVD was explained by the vapor-liquid-solid (VLS) mechanism [35,39,47]. Briefly, the VLS mechanism involves three stages: (i) the formation of metal-Si liquid droplets on catalyst, (ii) the dissolution and diffusion of gaseous Si into the droplets and (iii) the growth of Si crystals (Table 3) [38]. Gaseous precursors, such as silane (SiH₄), disilane (Si₂H₆) and chlorosilane (SiH₂Cl₂ and SiCl₄), are usually used as the Si source, and a wide range of metals, including Au, Cu, Pt and Ni, serve as the metal catalyst [35]. It is noted that a-Si layers were also deposited on the surface of non-metal substrates, like graphite [63] and silica particles [64]. The reaction temperatures used in CVD were varied between 300 and 1000 °C, depending on the gaseous precursors, metal catalysts or substrates [65]. One of

the most useful merits of CVD is the ability to control the Si structure and properties, including morphology, porosity, density and crystallinity, which are critical to effectively suppressing the volume expansion of Si and extending the cycle life of Si electrodes. The electrochemical performance of Si nanostructures with different dimensions prepared by CVD is summarized in [Table 4](#) and discussed below.

Si NPs. Si NPs are one of the most promising candidates for LIBs due to their high capacities, moderate fracture resistance and good compatibility with the current electrode manufacturing processes. However, direct utilization of commercial Si particles faces many challenges such as poor electrical conductivities of individual Si NPs and the growth of SEI layers resulting from volume expansion/contraction of solid Si particles. To circumvent the poor electrical conductivity, Si NPs were deposited on conductive substrates, like carbon black granules [\[63\]](#) and graphene (G) sheets [\[66\]](#), using SiH₄ as the gaseous precursor. In particular, ultrafine a-Si NPs of 5-10 nm in diameter were uniformly deposited on both sides of graphene sheets ([Fig. 5a](#)). Owing to the enhanced electrical conductivity and chemical, mechanical stability of graphene sheets, the a-Si/G composite electrodes exhibited an average capacity of 1103 mAh g⁻¹ over 1000 cycles ([Fig. 5b](#)) and a high capacity of 1148 mAh g⁻¹ at an ultra-high current density of 28 A g⁻¹ ([Fig. 5c](#)) [\[67\]](#). To address the issue of unstable SEI layers, hollow or porous Si spheres [\[64,68\]](#) have been prepared by CVD to provide empty space for free expansion of Si, which in turn diminished the detrimental effect of volume changes of Si core on SEI surface. It should be noted, however, that the fine or hollow Si particle electrodes also created new challenging issues that need to be taken into account in future research. The large surface area of the fine a-Si/G electrode exposed to electrolyte may induce a low initial Coulombic efficiency (ICE), while the hollow Si with a large empty space of 67 % porosity, may result in a low tap density with a low volumetric capacity [\[64\]](#).

Si NWs/nanotubes (NTs). Different from the spherical, zero dimensional (0D) Si particles,

one dimensional (1D) Si NWs possess characteristic advantages, as follows. (i) The small diameter NWs can accommodate large volume changes without cracking; (ii) the charge transport is enhanced by the large aspect ratio of Si NWs; (iii) Si NWs grown on conductive substrates can be directly used as electrodes without adding conductive additives or binders, potentially helpful for reducing the manufacturing cost. The first attempt to employ Si NWs as electrode can be traced back to 2008 when Si NWs were grown on a stainless steel substrate using Au particles as the catalyst and SiH₄ gas as the Si precursor (Fig. 5d) [69]. The freestanding Si NW electrodes delivered an ultra-high initial capacity of 3124 mAh g⁻¹, but a fast capacity degradation was observed within 10 cycles due to the unstable SEI layers. To improve the structural stability and rate capability, core/shell structures were developed to form CNF core/a-Si shell (CNF/a-Si) (Fig. 5e) [70] and c-Si core/a-Si shell (c-Si/a-Si) composites (Fig. 5f) [71]. These core/shell structures were produced by CVD of SiH₄, combining the advantages of good electrical, mechanical properties of c-Si or CNF core and the high capacity of a-Si shell. The capacities of the CNF/a-Si and a-Si/c-Si NWs were 1600 and 1000 mAh g⁻¹ after 55 and 100 cycles (Table 4), respectively. These values, however, are far from sufficient to satisfy the requirements for practical applications because the issue of unstable SEI layers was only partially resolved. Another type of 1D nanosilicon prepared by CVD is Si NTs, which is probably more effective in improving the electrochemical performance than the solid Si NWs by providing two sides for ion/electron diffusion and large interior empty space to allow inward expansion of Si [72,73]. One outstanding example of Si NTs is the double-walled Si-SiO_x NTs (DWSiNTs) synthesized by depositing Si on a CNF template followed by simultaneous burning of the CNF template and the formation of a SiO_x layer on the Si surface [36]. During lithiation, the inner Si wall enclosed by the rigid SiO_x shell expanded only inwards to the hollow space so that the SEI layer remained intact and stable on the surface of DWSiNTs (Fig. 5g). Compared with the solid Si NWs and

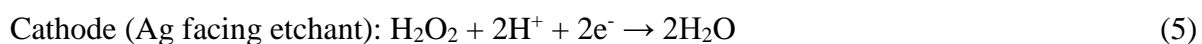
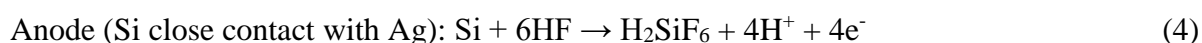
hollow Si NTs, the DWSiNTs were able to control the growth of SEI layers as confirmed by *ex-situ* scanning electron microscopy (SEM). As a result, the DWSiNT electrodes survived over 6000 cycles at 24 A g^{-1} with a remarkable capacity retention of 85 %, which is considered among the longest cycle life ever reported (Fig. 5h). Other types of Si NTs have also been prepared using templates made from ZnO [74] and MgO NWs [75] to reduce the cost and prolong the cycle life of Si NT electrodes. Similar to the case of Si hollow spheres, major concerns of Si NTs include the low tap densities, e.g. $0.02\text{-}0.1 \text{ mg cm}^{-2}$ for DWSiNT electrodes [36], and low volumetric energy densities caused by the large empty space. This means that future development should strike a balance between the ultra-long cycle life and the practical volumetric energy densities.

Si thin film. When Si is deposited on a flat substrate like glass, a two dimensional (2D) Si thin film is formed. Besides the advantage of a low dimension permitting fast ion diffusion and accommodating the mechanical strains generated during charge/discharge cycles [76,77], the Si film with well-defined geometries and chemical compositions is one of the best choices for fundamental research. Topics like the reaction kinetics [78], mechanical properties of lithiated Si [79] and the structure and composition of SEI layers [80] have been extensively investigated by monitoring the chemical and morphological changes of Si thin film electrodes. For example, Si films of 100 nm in thickness obtained by plasma enhanced CVD were used to study the Li ion diffusion coefficient during cycles by time-of-flight secondary ion mass spectrometry [78]. It is noted that the diffusion coefficient was $\sim 5.9 \times 10^{-15} \text{ cm}^2 \text{ s}^{-1}$, which decreased with increasing SEI layer and SiO_2 thickness. The Si volume expansion was also calculated from the difference between the initial and final Si volumes at different points of lithiation/delithiation while the thickness of SEI layer was indirectly inferred from sputtering times of Si and SEI regions. The contributions of Si and SEI layer to the total volume expansion were 1/3 and 2/3, respectively, revealing the significance of SEI volume swelling.

The interesting information signifies the importance of proper design of stable SEI layers on Si electrodes.

2.2.3 Metal assisted chemical etching

Unlike the bottom-up CVD technique, metal assisted chemical etching (MACE) is an appealing top-down method for preparing various Si nanostructures. The history of MACE of Si is traced back to the early 1990s when the effect of ultrafine metal particles on the electrical conductivity of Si wafer was studied, proposing the new concept of chemical etching [38]. This technique was further developed to produce wafer-scale aligned Si NWs by localized catalytic etching of Si wafer using oxidized acid solution of HF-AgNO₃ [81–83]. In the MACE process, the reaction can be divided into two steps: namely, (i) deposition of Ag particles on Si surface and (ii) metal-assisted etching in etchant solution containing HF and H₂O₂ (Table 3). The chemical reaction can be described as [83]:



The MACE method has been employed mainly to prepare porous Si nanostructures with different morphologies, including porous Si particles, NWs and 3D structures.

Porous Si particles. To accommodate the volume expansion of Si without adding extra fabrication costs, commercial or ball milled Si NPs were treated by MACE to introduce abundant pores in a scalable manner [84,85]. Figs. 6a-b present how the porous Si NPs were prepared by B-doping and MACE in sequence [85]. The porosity of Si NPs was fine-tuned by adjusting the dopant concentration: the higher the degree of doping, the rougher the surface and the higher the porosity after etching, which is a reliable guideline for synthesizing porous Si particles with a desired structure. The Si electrodes with an optimal porosity delivered very stable capacities of 1400 and 1000 mAh g⁻¹ after 200 cycles at 1 and 2 A g⁻¹ with capacity

retention of 87 % and 81%, respectively. The remarkable electrochemical performance is attributed to the synergetic effects of abundant pores that accommodated the large volume changes during cycles and the large surface area that improved the infiltration of electrolyte with enhanced ion diffusion kinetics.

Porous Si NWs. Si NWs prepared by CVD delivered impressive electrochemical performance with high capacity retention after long cycles [36]. However, these positive results do not come without any negative challenges. Most notable among the problems with the CVD process are their expensive precursor materials, delicate equipment, low yields and low active material loading, making it unattractive in large-scale applications. Porous Si NWs with controlled diameters, lengths, orientations and porosities can be mass-produced by MACE using doped Si wafers, low-grade Si or bulk M-Si [83,86]. At the early stage, commercial doped Si wafers of 50.8 mm (or 2 inches) in diameter and 0.5 mm in thickness were directly used as feedstock to prepare Si NW electrodes using a wet chemical method (Table 3). The mechanisms behind the formation of pores on Si NWs is schematically illustrated in Fig. 6c. Part of Ag ions diffuses upwards during etching and re-nucleates on the sidewalls of etched Si NWs while the new Ag nanoclusters act as new etching sites to form pores on the NW sidewalls. It is established that the porosity of Si NWs had a positive relationship with the dopant concentration in Si source: the higher the dopant concentration, the higher the porosity of Si NWs [86]. The concentrations of AgNO₃ and H₂O₂ solutions also influenced the morphology of porous Si NWs [87]. Low grade M-Si was used as feedstock to prepare low-cost Si NWs with mesopores of 20-30 nm in size, a high specific surface area of 219.4 m² g⁻¹ and a large pore volume of 0.97 cm³ g⁻¹ [88]. The electrodes prepared from the porous Si NWs maintained a high capacity of 2111 mAh g⁻¹ after 50 cycles at 0.2 C. To further enhance the reversibility of porous Si NWs electrodes, SiO_x surface coating was applied [89] and graphene sheets were encapsulated [85] so that the SEI layers were

stabilized and the expansion of Si was confined. It is also revealed that the thickness of SiO_x layer on the surface of Si NWs should be less than 3 nm, otherwise the conductivity and capacity of Si NWs would be significantly compromised [89].

3D porous Si. It is noted above that the porous or hollow Si nanostructures with a large surface area may impose critical weaknesses with a low tap density and a low volumetric capacity. These discouraging properties may limit practical applications of the LIBs made from such electrodes, especially for EVs requiring high energy densities. To tackle this problem, 3D porous Si microstructures with large particle sizes and high tap densities have been prepared by MACE using bulk Si particles. For example, a multi-dimensional Si composed of porous NWs of 5-8 μm in length and with a pore size of ~10 nm has been synthesized using commercially available Si powders with a high yield of 40-50 % [90]. The 3D porous microstructure presented a high tap density of ~4.5 mg cm⁻² and an exceptionally high volumetric capacity of ~3600 mAh cm⁻³, which is about six times of 620 mAh cm⁻³ for commercial graphite. The tap density was at least an order of magnitude higher than those of other Si nanostructures mentioned above, e.g., 0.02-0.1 mg cm⁻² for DWSiNTs [36], 0.25-0.3 mg cm⁻² for a-Si/G [66] and ~0.2 mg cm⁻² for porous Si particles [84]. Nevertheless, the bulk 3D porous Si structure also had major weaknesses, such as unstable SEI layers and the degradation of materials characteristics arising from the accumulated volume expansion of Si building blocks. To restrict the volume expansion, SiO₂ layers were coated on their surface and the best capacity retention was demonstrated for the electrodes with a 7 nm-thick SiO₂ layer [89]. Another strategy is to prepare 3D Si structures containing macropores of tens to hundreds nanometer in size [91,92], which can provide sufficient empty spaces for free expansion of Si during lithiation without damaging the structure.

2.2.4 Magnesiothermic reduction

Magnesiothermic reduction was firstly proposed to convert silica frustules to microporous Si

replicas as gas sensors based on the following reaction at 650 °C [93]:



The conversion mechanisms were investigated later by *ex-situ* XRD and TEM techniques and were depicted as [94]:



Compared with the above BM, CVD and MACE methods, the MR approach possesses several unique advantages [65]: namely, (i) the original structure of silica can be preserved after the reduction process due to the moderate conversion temperature; (ii) after etching the MgO byproduct, a highly interconnected porous structure is generated; (iii) the process seldom involves a high temperature, expensive precursors, nor delicate equipment, making it an ideal low-cost method; and (iv) natural resources, like rice husks, beach sand and bamboo leaves, can also be converted into energy storage materials by this process, paving a highly sustainable means for preparing nanosilicon electrodes. MR has been extensively applied to fabricate multi-dimensional Si nanostructures with excellent electrochemical performance, and the details are given as follows.

Si particles. At the early stage of development, solid silica particles prepared from tetraethyl orthosilicate (TEOS) were used as the precursor for MR reaction [95–97]. The Si prepared from solid silica however were easily sintered into macroscale Si particles during reduction because of the sluggish Mg vapor diffusion in solid silica and the accumulated exotherm of the reaction on the silica surface. To mitigate these issues, hollow silica spheres were prepared as the precursor for hollow Si using polystyrene (PS) [98] or cetyltrimethylammonium bromide (CTAB) [99] as the sacrificial templates. The hollow Si obtained from the MR process was more flexible to withstand the structural deformation arising from the volume expansion of Si than the solid Si particles. In addition, various

functional coatings, such as Ag [98], polypyrrole (PPy) [99], TiO₂ [100], N-doped carbon [101] and graphene [102], were applied to improve the electrical conductivity and SEI stability of the hollow, porous Si structures. Very recently, a hierarchical porous Si nanospheres (hp-Si NSs) were prepared using solid/mesoporous silica core/shell spheres by taking advantage of different transportation rates of Mg vapor in porous silica shell and solid silica core (Fig. 7a) [103]. In contrast to the outward volume expansion of solid Si particles, the hp-Si NSs expanded inwardly towards the hollow core during lithiation because of the much stiffer lithiated outer layer than the unlithiated core (Fig. 7b). The ‘inward breath mechanism’ effectively prevented the hp-Si NSs electrode from fracture, maintaining the stability of SEI layers and giving rise to a high capacity of 1800 mAh g⁻¹ at 0.18 A g⁻¹ after 200 cycles (Fig. 7c). The hollow porous Si spheres, however, had a low packing density and a low volumetric capacity, which were partly resolved by forming secondary mesoporous Si/C microspheres that consisted of ultrafine primary Si nanocrystals of ~10 nm in diameter with a compliant carbon coating on them (Fig. 7d) [104]. The space-efficient packing structure with abundant internal pores led to a higher tap density of about 0.8 g cm⁻³ than those of other Si/C nanostructures [98–101]. The high tap density was particularly beneficial to enhancing the battery capacities, giving rise to a high capacity of ~1100 mAh g⁻¹ and a volumetric capacity of 960 mAh cm⁻³ after 500 cycles (Fig. 7e).

Si nanofiber (NF)/NT. 1D Si NFs/NTs can be prepared using silica fibers because their original morphologies are preserved during the MR reduction. The 1D Si consisted of interconnected fine Si primary nanocrystals surrounded by numerous pores after etching the MgO byproducts [105–107]. The facile and scalable electrospinning method is an ideal means to synthesize the 1D silica precursor. For instance, silica NF papers have been produced by an *in-situ* acid-catalyzed polymerization of TEOS, as schematically shown in Fig. 7f [108]. The silica NF paper was reduced by MR to a freestanding, flexible Si NF film

containing a myriad of Si NPs of 8-25 nm in size. After coating with a thin layer of carbon to enhance the electrical conductivity, the electrodes made from the Si NF films delivered an excellent capacity of 802 mAh g⁻¹ after 659 cycles at 0.4 A g⁻¹ thanks to the high porosity arising from selective etching of MgO and the protection of Si NFs with carbon coating. Si NTs with an internal hollow space were also prepared by a surface sol-gel reaction between the electrospun polyacrylonitrile (PAN) fibers and TEOS followed by calcination in air [109]. After the reaction, the silica NTs were converted to Si NTs with a rough surface and a hollow tube structure, where the large surface area and pore volume allowed easy access by the electrolyte and free volume expansion of Si.

3D Si. Similar to the 3D porous Si derived from the MACE process, 3D porous Si can also be mass-produced by MR with low cost, novel structures and excellent electrochemical properties. More importantly, the 3D Si electrodes can be fabricated by MR using very cheap, sustainable and abundant natural resources, such as beach sand [94,110,111], rice husk [111–113], bamboo leaves [114] and reed plants [115]. The 3D Si-based anodes derived from natural materials deliver long cycle life, high capacities and good rate capabilities (Table 4) by forming stable SEI layers while preventing particle fracture. Several material and processing parameters are found critical to determining the morphology, scalability and electrochemical performance of 3D Si produced by the MR method. They include (i) the porosity of silica precursor, (ii) the temperature ramp rate, (iii) the diffusion rate of Mg vapor, (iv) the local heat accumulation and (v) the conversion efficiency. First, the silica precursors with an intrinsic 3D interconnected porous structure, like rice husks and bamboo leaves, were easily converted to highly porous 3D Si with a high yield and small-size primary particles [111–114]. In contrast, the Si particles prepared from solid beach sand were usually large in size and contained low porosities. Second, it is discovered that there existed a critical heating rate of 5 °C min⁻¹ for the reduction of rice husks, above which the Si nanocrystals tended to

become heavily sintered and below which the crystallinity and the particle size were not affected [111]. Third, to evaluate the influence of diffusion rate of Mg vapor on reduction kinetics of silica particles, the mixture of beach sand and Mg powder was placed in the containers under two different pressures, including low-pressure vacuum and an atmospheric pressure. It is demonstrated that the use of vacuum markedly improved the homogeneous transport of Mg into the sand powders in which the conversion was completed in 30 min [94]. Fourth, a high temperature was generated during the highly exothermic MR reaction, leading to sintering and formation of large grains in Si nanocrystals. To mitigate the side effect by sintering, NaCl powders were employed as the effective heat-scavenger to remove the MR heat and promote the formation of 3D porous network with ultrafine Si nanocrystals [110]. Last, the conversion efficiency of the most reported MR Si nanostructures obtained at the atmospheric pressure was lower than 50 % due to the formation of a significant amount of Mg₂Si. A deep reduction and partial oxidation strategy was developed to convert the low-cost silica into mesoporous Si with an extremely high yield above 90 % [116]. The process of this strategy is schematically illustrated in Fig. 7g and the relevant chemical formulas are given in Eqs. (10-13). The SiO₂ particles were fully reduced to Mg₂Si/MgO/Mg with excess Mg (Eq. 10), and the as-prepared intermediate product was oxidized in air to form MgO and Si (Eqs. 11 and 12). Finally, the mesoporous Si was obtained by etching off the MgO byproduct (Eq. 13).



The 3D Si structures prepared by MR have many beneficial features, including a high porosity, fine Si nanocrystals, a high conversion yield, low cost and sustainable resources,

making the MR derived 3D Si more attractive than those prepared by the MACE method for large-scale applications.

2.2.5 Other approaches

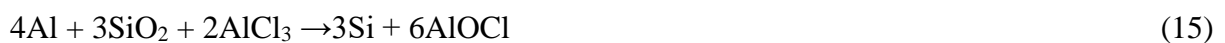
In addition to the major four fabrication methods discussed above, a few other synthesis routes have also been developed to prepare nanosilicon for LIBs. They include SiO thermal disproportion, acid etching of Si-metal alloys, molten salt reduction, Rochow reaction of bulk Si [117], NaK alloy [118] or organic surfactant reduction [119] of SiCl₄ and thermal annealing of hydrogen silsesquioxane precursors [120]. The first three techniques have been more popularly used than the rest and thus are discussed in the following.

Thanks to its high capacity of ~1200 mAh g⁻¹ and unique structural features, SiO is considered one of the most attractive materials among different Si-based electrodes. The Si suboxide concept suggests that SiO comprising amorphous Si and SiO₂ clusters can be transformed into Si and SiO₂ particles by heat treatment, through the so-called ‘disproportion reaction’ [121,122]. Micro-sized Si particles composed of nanoscale primary Si crystals were fabricated by thermal disproportion reaction of microscale SiO particles, which showed both good cyclic stability and a high volumetric capacity [123]. Among different primary Si particle sizes of 10, 15, 30 and 80 nm obtained at different reduction temperatures, 15 nm was found to be the optimal showing the best cyclic stability without compromising the reversible capacities and volumetric energy densities [124]. Non-filling carbon-coated porous Si microparticles were also designed by coating SiO particles with resorcinol-formaldehyde resin before thermal treatment and acid etching of SiO₂ [125]. It is revealed that the voids created in the place of SiO₂ provided sufficient space for expansion of Si particles without damaging the outer SEI layers and the carbon coating, giving rise to high capacity retention of 1490 mAh g⁻¹ after 1000 cycles at 1 A g⁻¹.

Etching of Si-metal alloys is another scalable method to synthesize micro-sized Si electrodes

[126,127]. For example, the Si-Al alloy powders with uniformly dispersed Si and Al atoms have been used as the raw material to produce porous Si by simple etching of Al using an acid [128–132]. The pores created thereby played an important role to accommodate the volume expansion and facilitate fast Li ion transfer during cycles. To enhance the cycle life, Coulombic efficiencies and volumetric capacities of porous Si anodes, several modifications have also been introduced to the electrode materials. They include adding few Fe and Al impurities to enhance the electrical conductivities [130], the introduction of defects such as dislocations, twin boundaries and stacking faults to allow plastic flow of Si during lithation [128], and the incorporation of conductive and/or compliant coating layers, like graphene sheets [132] and Al₂O₃ [131]. Although porous Si particles prepared from etching Si-metal alloys are promising anodes for industrial applications, the progress is still in the infant stage of development, in need of more efforts to control the porosity, so that the conversion yields are augmented for optimized electrochemical performance.

To mitigate the concerns about the relatively high reaction temperatures of CVD (300–1000 °C), MR (650 °C) and Si-metal alloying (~760 °C) processes [128], a low temperature molten salt process has been developed to prepare Si NPs where SiCl₄ [133] or silicon zeolite [134] is reduced in the molten AlCl₃ salt at below 200 °C. The chemical reactions taking place with SiCl₄ and SiO₂ precursors can be expressed as [134]:



In both reactions, AlCl₃ not only acts as molten salt but also participates in the reaction by forming MgAl₂Cl₈ and AlOCl byproducts. These byproducts are removed by etching to create pores in their place. The Si electrodes with nanoscale pores and ultrafine Si NPs delivered high reversible capacities of 2663 and 870 mAh g⁻¹ at 0.5 and 3 A g⁻¹ after 1000 cycles, respectively. One major drawback of this approach is that AlCl₃ is very sensitive to

water, making the process expensive and difficult to handle in large scale applications.

2.2.6 Summary of fabrication methods and design principles of nanosilicon

Many different techniques have been developed to fabricate nanostructured silicon with various sizes, morphologies and porosities. While the majority of these methods can contribute to promoting the real-world implementation of Si anodes by substantially improving the electrochemical performance, some may offset certain properties of the electrodes, like high volumetric capacities. Therefore, critical comparison is made of the electrochemical performance of electrode materials prepared by different fabrication methods. It is hoped that the comparison can offer clear insight into the essential principles for designing Si nanostructures, while providing a general guideline and selection criteria of fabrication methods that can satisfy the requirements for different end applications.

Fabrication methods. Table 3 summarizes the principles, morphologies of the synthesized Si structures, estimated production costs and advantages/disadvantages of the four main fabrication methods discussed above. From the viewpoint of large-scale applications in industry, several essential parameters need to be taken into account in the selection of fabrication methods, such as the cost and yield, environmental friendliness and morphological controllability. For example, the ball milling process is the cheapest at price less than \$2 kg⁻¹ with the highest yield of ~4 kg h⁻¹. It employs low-grade Si resources, making it suitable for large-scale applications. In contrast, Si prepared by CVD involves expensive and flammable SiH₄ gas (>\$100 kg⁻¹), delicate equipment with an extremely low yield of ~0.75 mg h⁻¹. Although the nanosilicon electrodes produced by CVD always present impressive electrochemical performance, the cost and yield issues discourage their applications in real world. The costs and yields of Si prepared by MACE [88,89] and MR (Table 3) are currently acceptable on a laboratory scale, which should be extended for industrial production. It is worth noting that the low-cost and abundant natural resources for

MR make this method more attractive and sustainable for developing practical energy storage devices than MACE. Environmental friendliness is another critical factor from the long-term viewpoint. The starting materials for the BM, CVD and MR processes, such as bulk Si particles, silica and Mg, are non-toxic and environmentally friendly to some extent. In contrast, the MACE process employs highly toxic and dangerous H_2O_2 , HF and AgNO_3 solutions, which significantly offset the advantages of the MACE method in large-scale production. It is demonstrated in the above sections that the nanosilicon materials with different dimensionalities, including Si particles/spheres (0D), Si NTs/NWs/NFs (1D), Si thin films (2D) and 3D porous Si, are all attractive candidates for both practical applications and fundamental investigation of LIBs. Therefore, the ability to control the morphology of nanosilicon is an important criterion determining the selection of fabrication methods. The CVD, MACE and MR approaches are capable of preparing nanosilicon materials with different dimensions, whereas the BM process is less attractive as it can produce only solid particles, as shown in [Table 3](#).

Design principles of nanosilicon. [Table 4](#) summarizes the electrochemical performance of different Si nanostructures prepared by different approaches. It is obvious that significant progress has been achieved in terms of reversible specific capacities, Coulombic efficiencies, cyclic life and capacity retention. Several general conclusions and important suggestions can be drawn from the results, which can contribute to designing better nanosilicon electrodes in the future, as follows. (i) The Si electrodes with smaller particle sizes tend to exhibit better cyclic stability and high-rate capability than those with larger sizes. This is verified by a number of exemplary results: e.g. high reversible capacities of 1103, 990 and 1024 mAh g^{-1} after 1000 cycles for a-Si/graphene [\[67\]](#), mesoporous Si/C microspheres [\[104\]](#) and sand-based Si particles [\[110\]](#), respectively, all of which were made of ultrafine Si particles. As discussed in Section 2.1, the smaller Si particles provide a shorter ionic transport distance, a

larger electrolyte contact area and a higher strain required for mechanical fracture, giving rise to enhanced high-rate performance and cyclic stability. (ii) The incorporation of pores or voids enhances the high-rate capacities and cycle life, as evidenced by the hollow Si NSs [64,103,135], porous Si NPs [84,85], porous Si NWs [87,88] and 3D porous structure [92,115], all of which contained numerous pores and/or large voids. These pores functioned as both the buffer to absorb the volume expansion, maintaining the structural integrity, and the channels to facilitate fast electrolyte permeation. (iii) The stability of the SEI layer at the interface between the liquid electrolyte and Si electrode is another important factor for long cyclic life. Long-term stability has been reported for double walled Si-SiO_x NT electrodes after 6000 cycles [36] and for mesoporous Si/SiO_x exhibiting an almost negligible capacity degradation of about 0.035% per cycle for over 1400 cycles [116]. Both of these two nanostructures had a mechanically rigid SiO_x coating that stabilized the SEI layer during the lithiation/delithiation cycles. (iv) Conductive coatings or substrates in the nanostructured Si electrodes can promote not only the high rate capacities and structural integrity, but also the stability of SEI layers. This is supported by the excellent performance of hollow Si spheres coated with different conductive materials [98–102]. The importance of coatings is further illustrated in Section 2.3.

2.3 Hybridization of nanosilicon with functional materials

Among the many issues of Si electrodes, volume expansion is known to be the most serious challenge causing mechanical fracture of Si and total failure of the electrode. Pulverization has been addressed by designing various nanostructures with different dimensions using different fabrication methods, as discussed above. However, the problems of unstable SEI films, low Coulombic efficiencies and poor electrical conductivities cannot be resolved by optimizing the Si nanostructures alone. Thus, functional materials, like carbon, conducting polymers and metal (oxides), have been incorporated into nanosilicon to form high

performance Si-based composite electrodes. The detailed discussion is made as follows.

2.3.1 Silicon/carbon composites

The incorporation of carbon materials with nanosilicon has been widely exploited and considered an effective approach to improve the electrochemical performance. The flexible, lightweight, highly conductive and thermally stable carbon materials can not only enhance the electrical conductivity, but also constrain the volume expansion of Si and fracture of SEI layers [45,46,136]. The Si/C composites can be classified into several groups based on the dimensions of carbon, including 0D carbon coating, 1D CNFs/CNTs and 2D graphene. The morphologies, Si contents and electrochemical performance of various Si/C composites are summarized in Table 5.

Si/carbon coating composites. A carbon coating on Si has many ameliorating effects on benefitting the energy storage capabilities of electrodes, as follows. (i) The carbon sheath can improve the ion/electron transport and reaction kinetics of Si NPs; (ii) the soft carbon coating functions as the buffer to accommodate the volume expansion of Si during lithiation; (iii) the carbon shell prevents the Si particles from direct contact with the electrolyte, effectively discouraging the formation of thick SEI layers; and (iv) the carbon coating serves as the physical barrier to prevent aggregation of active particles during cycles. A uniform carbon coating on Si surface is normally obtained by thermal decomposition of polymer precursors, such as poly vinyl alcohol (PVA) [137], dopamine [138], PAN [139] and polyvinylidene fluoride (PVDF) [140], or by CVD deposition of carbon using gaseous precursors of CH₄, C₂H₄ and C₂H₂ [134,135]. For example, carbon-coated Si (Si/C) composites were prepared by one-pot carbonization of the mixture containing commercial Si particles and PVDF (Fig. 8a) [143]. The Si/C electrodes delivered a high capacity of 2057 mAh g⁻¹ after 40 cycles, which is much higher than the negligible capacity of 81 mAh g⁻¹ only after 5 cycles for a bare Si electrode (Fig. 8b). The improved performance is attributed to the enhanced interfacial

contact, a conductive network and the compliant carbon coating for stress relaxation. However, the thin carbon coating was unable to withstand the whole volume expansion to prevent fracture of Si/C particles, to be discussed in Section 3.1. To mitigate the danger of mechanical failure, several strategies have been devised, such as Si/C composites with fine Si crystals below 15 nm in diameter [124], porous Si/C particles [144–146] and a Si/C yolk/shell structure with an empty space around the Si particles [56,147,148]. An excellent reversible capacity of $\sim 1110 \text{ mAh g}^{-1}$ after 1000 cycles at 1 C has been reported for the Si/C yolk/shell electrode [147]. However, the same structure exhibited a low initial Coulombic efficiency of 60 % and a moderate capacity of $\sim 500 \text{ mAh g}^{-1}$ at a high current density of 4 C, due probably to the formation of a thick SEI layer stemming from the large contact area with the electrolyte and poor electronic conduction due to the point-to-point contact between Si and carbon shell. Thus, it is necessary for the porous Si/C composite electrodes to strike a balance among different performance criteria such as long cycle life, high irreversible capacities, moderate high-rate capability and possibly low volumetric capacities.

Si/CNT composites. 1D CNTs with high electrical conductivities, large surface areas, excellent mechanical and chemical stability have been widely used as the substrate to support nanosilicon. The addition of CNTs improved the electronic/ionic conductivities of the electrode, protected the SEI layers and prevented the Si particles from agglomeration during cycles [43]. Due to the hollow structure of CNTs, Si NPs can be deposited on both the external and the internal surfaces of CNTs. For example, nanoscale a-Si/c-Si droplets were deposited on vertically aligned CNT supports using a two-step CVD process (Fig. 8c) [149]. The CNTs in the composite electrode functioned both as the charge transfer channel and the flexible mechanical support to accommodate the volume expansion of Si particles, giving rise to a high cyclic capacity of $\sim 2000 \text{ mAh g}^{-1}$ after 20 cycles. However, the 20-time cycle life was insufficient to satisfy the requirements for commercial applications, which was explained

by the direct exposure of Si to electrolyte and separation of Si particles from the CNT surface after repetitive expansion/contraction. In an effort to further enhance the cycle life, Si were deposited on the inner surface of CNTs where they could deform inside the tube with no danger of pulverization nor inadvertently affecting the SEI layers on the outer surface of CNTs (Fig. 8d) [150]. The CNT/Si shell/core structure outperformed the earlier CNT/Si core/shell structure by presenting a high capacity of $\sim 800 \text{ mAh g}^{-1}$ after 250 cycles maintaining a remarkable Coulombic efficiency of 99.9 % [149]. The *in-situ* TEM study carried out of the CNT/Si shell/core composite electrode revealed that the CNT walls restricted the volume expansion of Si particles to only $\sim 180 \%$ [151], much lower than the theoretical value of over 300 %. Further, significant progress has been made to synthesize freestanding Si/CNT composite electrodes for flexible LIB applications utilizing the excellent flexibility of CNT matrix. They include twisted, aligned CNT/Si fibers [152], Si/cone-shaped CNT films [153] and multilayer Si/CNT fibers [154], which can make a promising future in powering flexible electronic devices [155].

Si/CNF composites. Besides CNTs, CNFs with unique merits of large aspect ratios, short Li ion diffusion paths and efficient electron transport along the fiber direction are another useful substrate for nanosilicon [156]. Electrospinning is a facile and versatile method to produce CNF films or webs by applying a high voltage to the polymer solution to eject into continuous nanoscale fibers [157]. This technique is considered one of the most promising approaches to continuously produce freestanding and conductive battery electrodes, eliminating the use of heavy metal current collectors, conductive additives or binders. Active materials can be *in situ* grown and/or incorporated into the PAN or PVA precursors before electrospinning, and the dimensions and structure of CNFs can be tuned or modified to optimize the pore size/volume and surface area [158–160]. At the early stage, Si/CNF films were prepared by electrospinning the mixture of commercial Si NPs and PAN, followed by

carbonization of the polymer matrix [161–163]. The electrodes made from the Si/CNF composites presented enhanced electrochemical performance, in terms of both specific capacity and cyclic life, compared to the neat Si anodes. However, the cycle life was usually below 100 cycles even at low current densities (Table 5), which can be explained by severe agglomeration of Si NPs, weak interfacial bond between Si and polymer, and poor conductivities of amorphous CNFs. To address these issues, several strategies have been successfully devised, as follows. (i) Si NPs were monodispersed by amino-silane termination followed by F ion mediation in aqueous solution, satisfying the prerequisite for good dispersion of Si particles in CNFs [164]. (ii) Conductive additives, such as graphene sheets [164], CNTs [165] and carbon black [166], and/or sacrificial catalyst particles, like Fe [167] and Ni [168], were incorporated into the polymer precursor to form graphitic carbon layers/spheres in the CNF matrix. (iii) Large voids were systematically created between the Si particles and carbon sheath by partially etching the Si particles to form highly porous Si/CNF composites [167,169]. Co-axial Si/CNF core/shell architectures were also synthesized by completely encapsulating the Si particles in the CNF matrix for extended cycle life (Fig. 8e) [170–172]. The electrochemical performance of various Si/carbon electrodes given in Table 5 indicates that the porous Si/CNF (872 mAh g⁻¹ after 200 cycles) and the co-axial core/shell Si/CNF electrodes (750 mAh g⁻¹ after 300 cycles) outperformed the solid Si/CNF electrode (644 mAh g⁻¹ after 50 cycles), a testament to the benefits arising from the ameliorating composite structures.

Si/graphene composites. Graphene, a single layer of carbon atoms arranged in a hexagonal manner, has been recognized as a promising platform to support diverse nanomaterials including nanosilicon. In general, the incorporation of graphene sheets can improve the electronic/ionic conductivities of the electrode, reduce the aggregation and volume expansion of Si particles, benefiting from its excellent electrical conductivity, good thermal and

chemical stability, a large theoretical specific surface area and flexibility [173]. In the early days, Si/G composites were prepared in the form of hybrid papers or films mainly by vacuum filtration or freeze drying of graphene oxide (GO)/Si suspension [174–176]. Although these cost-efficient Si/G electrodes exhibited improved electrochemical performance, their poor structural design brought about a few issues, including heavy agglomeration of Si particles, poor contact between Si and GO and sluggish ion diffusion through the GO plane, adversely affecting the electrochemical properties of the composite electrode. These issues have been resolved by devising several strategies, such as introducing covalent bonds [177–179] or electrostatic attraction between the surface-modified Si particles and GO sheets [180], and engineering in-plane vacancies on GO sheets as ion diffusion channels [181], substantially enhancing the reversibility and high-rate capability of Si/G composites. Nevertheless, the Si/G hybrid films/papers suffer a new challenge of limited penetration of electrolyte for high energy/power density applications due to tight stacking of graphene sheets while the areal mass loading and the electrode thickness are increased. 3D porous graphene structures, like graphene foam (GF) [182,183], graphene aerogel [184,185] and graphene tree [186], were employed to form 3D Si/G composites which offered rapid and robust ion transport paths and electrolyte infiltration channels throughout the whole electrode, giving rise to high energy/power densities. It may be worthwhile to highlight the recent work on Si NP-impregnated assemblies of templated carbon-bridged oriented graphene (TCG-Si) structure prepared by simple filtration and annealing (Fig. 8f) [187]. The TCG-Si bulk assemblies created a network for rapid ion/electron transport throughout the electrode even at a high mass loading along with a high tap density of 1.3 g cm^{-3} . The anodes made from TCG-Si presented a remarkable rate capability of 900 mAh g^{-1} at 8 A g^{-1} and a high volumetric capacity of 1807 mAh cm^{-3} after 200 cycles (Fig. 8g), paving an attractive and viable way to design energy storage devices with both high energy and power densities.

2.3.2 Silicon/conducting polymer composites

Apart from carbonaceous materials, conducting polymers have also been introduced to accommodate the volume expansion of Si and to form conductive networks for enhanced reaction kinetics of the electrode. Four different conducting polymers have been mainly used in Si-based composites [188–191], including PPy, polyaniline (PANi), poly(3,4-ethylenedioxythiophene) (PEDOT) and poly(3,4-ethylenedioxythiophene) doped with poly(4-styrenesulfonate) (PEDOT:PSS), all of which have useful features, such as simple fabrication, high electrical conductivities, structural flexibility and wide applications (Table 6). The representative Si/conducting polymer composite electrodes with their preparation procedures, Si contents and electrochemical properties are summarized in Table 7.

Uniform dispersion of Si particles within polymer, a strong interface bond between Si and polymer and a high electrical conductivity of polymer are among the most critical parameters determining the electrochemical performance of Si/conducting polymer composite electrodes. First, to obtain good dispersion of Si particles and uniform polymer coating, conducting polymers are usually *in-situ* formed using monomers on the surface of Si particles. For instance, a 3D hierarchically porous PPy/Si/single-walled CNT (SWCNT) composite was prepared by *in-situ* polymerization of pyrrole monomer with phytic acid followed by the formation of hydrogel of Si particle/SWCNT dispersion [192]. The *in-situ* formed polymeric layer on Si particles was ~15 nm thick and the energy dispersive spectrometer (EDS) mapping revealed a uniform coating thickness (Fig. 9a). As a consequence, the PPy/Si/CNT composite electrode delivered a stable capacity of 1600 mAh g⁻¹ after long-term 1000 cycles at 3.3 A g⁻¹, outperforming the PVDF/Si and PPy/Si electrodes (Fig. 9b). Second, a strong interfacial bond between PANi and Si NPs was achieved by *in-situ* polymerization [193]. During the polymerization of aniline monomers, the phosphoric acid groups in phytic acid bind with the native oxide layer on Si particles (Fig. 9c). In contrast to the fast capacity

degradation of the electrodes made from a Si/PANi mixture, the *in-situ* polymerized Si/PANi electrodes exhibited a stable capacity of 1600 mAh g⁻¹ for 1000 cycles based on the weight of Si alone (Fig. 9d). Moreover, the interfacial bond between PANi and Si particles was further enhanced by doping with 5-sulfoiophthalic acid containing carboxyl and sulfo acid (-SO₃H) functional groups so that the cyclic stability and energy densities of the Si/PANi electrodes were much improved [194]. Third, PPy and PANi with moderate electrical conductivities (Table 6) may not fulfill the capacity demands at high current densities, thus highly conductive SWCNTs [192] or graphene sheets [195] were incorporated to further improve the electrical conductivity and thus to promote the electron/ion transport. In addition, water-soluble PEDOT:PSS has a conjugated backbone that allows efficient de-localized electron transport, leading to an extremely high electrical conductivity of 10-10³ S cm⁻¹, making it an ideal material for electrode applications [196–198]. However, it is still necessary to understand why most of Si/conducting polymer electrodes deliver poor initial Coulombic efficiencies of less than 80 % (Table 7). The irreversible reaction taking place between the liquid electrolyte and conducting polymer may partially be responsible. Nevertheless, the roles of different conducting polymers on electrochemical performance of Si electrodes remain poorly understood, which needs further efforts for in-depth investigation.

2.3.3 Silicon/metal (oxides) composites

When the electrical conductivities of carbon materials and conducting polymer coatings are difficult to satisfy the required fast charge transport at extremely high rates, the integration of Si with highly conductive metal coatings, like Cu or Ag (with electrical conductivities of 5.96 × 10⁵ and 6.30 × 10⁵ S cm⁻¹, respectively), are the only remaining options [43,44]. The metal coatings not only ameliorate the surface conductivity of Si particles ensuring adequate utilization of high capacity active materials at high current densities, but also protect the Si core from pulverization and direct contact with electrolyte, allowing the formation of stable

SEI layers with a resulting high power density and long cycle life of the Si/metal electrodes [98,199–201]. However, metal coatings are not free from issues. Their main drawbacks include the high gravimetric densities, electrochemical inertness and high costs which should compromise the high energy densities of nanosilicon materials.

Another critical concern about carbon and conducting polymer coating materials is their low or negligible lithium storage capacities, leading to a significant energy density penalty for the composite electrodes. In view of this, combining Si with electrochemically active metals or metal oxides, such as Fe₂O₃ [202], SnO₂ [203], Co₃O₄ [204], Li₄Ti₅O₁₂ [205], Sn [206] and Ge [207], is considered a sensible option to improve the electrochemical performance without comprising capacities. Ge has a high electrical conductivity (i.e. 10⁴ times higher than Si) and a substantial Li ion diffusivity (400 times higher than Si), but with a moderate specific capacity of 1600 mAh g⁻¹ [208]. It is envisaged that the combination of Si active material and Ge with excellent reaction kinetics can produce ideal Si/Ge hybrid electrodes possessing both high energy and power densities. This was realized by constructing a Si/Ge branched NW heterostructure using a pyrolysis synthetic protocol and a sequential secondary seeding method (Fig. 10a) [207]. The hybrid electrodes exhibited high capacities of 1612, 1459 and 1256 mAh g⁻¹ after 100 cycles at Ge:Si mass ratios of 2:1, 3:1 and 4:1, respectively (Fig. 10b). Their rate capacities were also tunable by adjusting the Si to Ge mass ratios that the higher the Ge content in the electrode, the higher the capacity retention at high rates. This finding is important for designing electrode materials with either a high capacity or a high rate capability depending on end applications.

In addition to the large collection of aforementioned coating materials aiming to enhance the rate capacities and extend the cycle life of Si electrodes, there is another group of coating layers that are designed to endow the Si electrodes with special features, like enhanced thermal conductivities [209], fast Li-ion mobility [210] and low electrode expansion [211–

213]. For example, the large amount of heat generated in Si-based electrodes is a critical concern threatening the safe operation of LIBs, especially under severe conditions, like an elevated temperature environment. Si/TiO_{2-x}@C core/shell NFs were prepared by dual-nozzle electrospinning where the Si particles were fully encapsulated by the TiO_{2-x}@C fiber shell (Figs. 10c-d). The heat accumulated in the co-axial fiber electrode in the temperature range 100-400 °C was 4.2 kJ g⁻¹, which is much lower than those of Si NPs, Si NP/C and commercial graphite electrodes (Fig. 10e) [209]. The high thermal stability with significantly reduced exotherm in the co-axial fiber electrode was due to the TiO_{2-x} shell which possibly retarded the thermal reactions between the lithiated Si and the electrolyte solution. Another intriguing report is the enhancement of Li ion mobility induced by the local piezoelectric potential of BaTiO₃ particles [210]. BaTiO₃ particles can absorb the mechanical stresses arising from Si volume expansion and in turn induce piezoelectric potentials (Fig. 10f). The piezoelectric potentials improved the electrochemical performance of the BaTiO₃/Si/CNT composite electrode during rapid charge/discharge cycles by enhancing the Li ion diffusion (Fig. 10g).

2.3.4 Discussion on Si-based composite electrodes

Tremendous efforts have been made in developing a myriad of different Si-based composites over the past decades, including Si/carbon, Si/conducting polymers and Si/metal (oxides), and the key properties and improved electrochemical performance of these electrodes are summarized in Tables 5, 6 and 8. Although drawing a firm conclusion is difficult in view of different materials, morphologies and measured parameters, several general implications can be identified to provide future directions in developing Si-based and other metal oxide composite electrodes. The following discussions include three major parameters of electrode materials, namely, electrical conductivity, structural stability and active material loading.

Electrical conductivity. One strong motivation to hybridize Si with functional materials is to

remedy the intrinsically poor electrical conductivity of Si, thus the host materials should have high conductivities to enhance the electrochemical performance of the electrodes, especially at high current densities. Generally speaking, the electrical conductivities of CNTs (10^2 - 10^6 S cm^{-1}), graphene (4×10^3 S cm^{-1}) [157], PEDOT: PSS (10 - 10^3 S cm^{-1}) and metal coating ($\sim 10^5$ S cm^{-1}) are already high enough to boost the rate capacities of Si electrodes. For example, the Ag-coated Si electrode delivered a high capacity of 640 mAh g^{-1} at 5 C [200], corresponding to one charge in 12 min. However, the other host materials, like amorphous carbon coating (10^{-3} - 10^2 S cm^{-1}), amorphous CNFs (10^{-7} - 10^2 S cm^{-1}) [157] and metal oxides, display relatively low electrical conductivities, which may cause a high internal resistance, large polarization and low utilization of active materials. In order to obtain high electrical conductivities of these composites, several strategies have been adopted, including, (i) the use of catalysts for graphitization of amorphous carbon, like nanocavity-engineered Si/functional CNFs [167] and Ni/Si/CNF [168] composites; (ii) the incorporation of CNTs or graphene sheets as conductive additives, like in SWCNT/PPy/Si [192] and BaTiO₃/CNT/Si [210] ternary composites; and (iii) the selection of active metals with higher conductivities, like Sn [206] and Ge [207]. For the latter two strategies, it is necessary to strike a balance between the electrical conductivity and the mass ratio of conductive additives to avoid excessive reduction in capacity.

Structural stability. The structural stability of nanosilicon electrodes has been discussed in Section 2.2.6, and here we place special attention on the stability of SEI layers and active materials because it is directly related to the Coulombic efficiency and capacity retention of the electrodes. A few strategies have been explored to maintain the integrity of electrodes, including (i) the design of core/shell and/or porous structures; (ii) the use of mechanically stable/flexible host materials; and (iii) the incorporation of materials that can absorb [210] or suppress [211] the volume expansion of Si. Table 5 shows that the cycle lives of internal

Si/CNT [150,151], core/shell Si/CNF [166,170,172] and porous CNF/Si [169] electrodes are much better than those of solid Si/CNF [161,162] and external Si/CNT [149] electrodes. It should be noted that the hollow and porous structures are detrimental to initial Coulombic efficiencies and volumetric capacities of the electrodes, which has to be kept in mind when designing these structures. The highly stable graphene sheets [180], CNTs [151] and Ag coating [199] and flexible polymers (Tables 6 and 7) can be used to directly encapsulate Si particles to constrain the volume expansion of Si and ensure structural integrity of Si-based composite electrodes. An optimal coating thickness is important as it determines the electrochemical performance of the electrodes, thus their correlation should be explored in future studies.

Active material loading. In general, there is a trade-off between the mass ratios of Si particles: host materials and the conductivity, cyclic stability of Si/C composite electrodes. An insufficient carbon host may neither provide efficient electron transport paths nor accommodate the volume expansion of Si particles, whereas too much carbon can compromise the high specific capacities of Si active material. Table 5 shows that the majority of Si/C composites with good electrochemical performance presents Si contents below 60 wt.%, which is much lower than ~70 wt.% of Si/conducting polymer composites (Table 7) and over 90 wt.% of Si/Ag composites [199,200]. Freestanding Si/C electrodes can partly compensate the low Si loading by eliminating the binders, current collectors and conductive additives. Techniques to fabricate freestanding electrodes include electrospinning of Si/CNF films, vacuum filtration to form Si/G papers, freeze-drying of Si/G aerogels and CVD to synthesize Si/graphene foams. Unlike the conventional slurry casting techniques, these freestanding composites can be directly employed as the electrodes without further treatments, potentially reducing the manufacturing cost. Moreover, the porous 3D structure like Si/G aerogels and Si/graphene foams with a large surface area can also promote electrolyte

penetration and ion diffusion for high power outputs. Another important merit is that the processes to synthesize freestanding electrodes are highly scalable, making them amenable to mass production.

2.4 Disadvantages of nanosilicon anodes and potential solutions

Apart from the aforementioned benefits and useful features of nanosilicon-based electrodes, they also possess several important disadvantages [214–217], including (i) low thermodynamic stability, (ii) formation of thick SEI layers, (iii) poor packing densities and (iv) high manufacturing costs. One should note that Si NPs tend to aggregate together to reduce their surface energy, causing poor dispersion of active particles among polymer binder and conductive additives. The Si particles within the large clusters are easily isolated from the conductive additives and electrolyte during the charge/discharge cycles, becoming the so-called ‘dead’ particles. Compounding the problem, these agglomerated Si NPs can be electrochemically sintered to form larger ones during lithiation, lessening the advantages arising from nanostructures. As discussed in Section 2.1, the large surface area offered by nanosilicon is a useful feature for high-rate performance by enhancing the ionic conductivity. In fact, the large electrolyte/electrode interfacial area is a double-edged sword. It favors the formation of more SEI on the electrode surface by consuming more electrolyte during discharge than in the Si electrodes with microscale particles, causing low Coulombic efficiencies. In addition, the tap densities of nanosilicon electrodes are very low, often below 0.5 g cm^{-3} , because of the large empty space between NPs and the voids created to accommodate the expansion of Si [36,66,84].

Effective strategies have been developed to mitigate the above disadvantages while maintaining the attractive features of nanosilicon. For example, Si NPs were monodispersed by amino-silane termination and F ion mediation in aqueous solution [164], ameliorating the dispersion of Si particles on carbon hosts. Forming microscale secondary particles is a

successful approach that can improve both the initial Coulombic efficiency and the tap density of Si anodes. For example, microscale Si secondary particles consisting of tightly assembled Si/C yolk/shell primary NPs were fabricated, which were also coated with an amorphous carbon layer as the electrolyte blocker [218]. The volume expansion of Si NPs was accommodated by the void space in the yolk/shell structure; the tap density was significantly enhanced to 0.53 g cm^{-3} by space-efficient packing of primary Si/C NPs while the formation of SEI was limited to the outer surface of secondary particles. A significantly higher tap density of 0.91 g cm^{-3} with an outstanding areal capacity of $\sim 3.5 \text{ mAh cm}^{-2}$ was further achieved by fabricating Si/C secondary clusters by means of mechanical press [219]. To mitigate the high material and fabrication cost of nanosilicon, magnesiothermic reduction of abundant natural SiO_2 sources, like sand, rice husks and bamboo leaves, has been demonstrated as a potentially cost-effective approach preparing nanosilicon with large scale and high performance, see Section 2.2.4.

Besides the aforementioned strategies to fabricating nanostructured Si and Si-based composites, there are many other material parameters, such as the electrolyte additives, binders and current collectors, which also significantly affect the reversible capacities and cycle life of Si anodes. Several useful reviews have recently appeared to shed insights into the design principles and optimal properties of binders [220–222], the working mechanisms of electrolyte additives [35] and promising current collectors beyond Cu foils [43]. As such, similar discussions will not be repeated here while more focus is placed on understanding the fundamentals, mechanisms and designs along with applications of nanosilicon electrodes in this review.

3. Fundamental understanding of Si anodes (based on *in-situ* experiments)

In parallel with the research efforts made to promote the electrochemical performance of Si

electrodes, extensive research has been directed towards understanding the underlying mechanisms behind the volumetric expansion, structural changes and fracture of Si during the lithiation/delithiation cycles. The information on these mechanisms can not only provide important guidance for designing optimized Si structures, but also shed light on factors influencing the reaction processes and the resulting electrochemical performance. Among various techniques devised for this purpose, the *in situ* examination appears to be most suited for real-time investigation of charge/discharge behaviors of electrode materials. Fundamental understanding revealed by *in-situ* TEM and other *in-situ* characterization techniques are discussed in the following, and the major findings are summarized in [Table 9](#).

3.1 *In-situ* transmission electron microscopy examination

In-situ TEM is a powerful tool recently developed to probe in real-time the electrochemical reactions taking place in the electrode at high spatial resolution [\[223\]](#). A typical nano-battery setup for *in-situ* TEM examination is illustrated in [Table 9](#). For probing Si anodes, the nano-battery apparatus consists of three components, including an electron transparent Si anode, a vacuum-compatible electrolyte (i.e. Li_2O) and a Li metal cathode. In an *in-situ* TEM experiment, lithiation commences as soon as the Si anode is in physical contact with the cathode while a negative bias potential is applied to the anode. Delithiation would happen when an opposite potential is applied to the anode. Based on many years of extensive research, substantial understanding has been established on lithiation mechanisms, reaction kinetics, the effects of coating layers on electrochemical behaviors of Si electrodes [and the properties of lithiated Si](#), as discussed in the following.

3.1.1 Lithiation mechanisms

It is discovered that c-Si NPs underwent a phase transition from c-Si to amorphous Li_xSi (a- Li_xSi) upon lithiation, as partially discussed in Introduction. The bump-shaped a- Li_xSi shell grown along the $\langle 110 \rangle$ direction ([Fig. 11b](#)) and the faceted c-Si core ([Fig. 11c](#)) indicate that

the lithiation of Si NPs was anisotropic with preferential lithiation along the $\langle 110 \rangle$ direction. This unique phenomenon was also observed in the lithiation of c-Si NWs [224], which was interpreted by differing interfacial mobilities of different crystallographic planes during lithiation [22]. The anisotropic expansion is not attributed to different diffusivities of Li in c-Si because the symmetric elements of cubic Si crystals can only lead to isotropic diffusion. Rather, it can be explained by the anisotropic reaction kinetics associated with different electrochemical potentials for different crystallographic planes of Si, according to the first principles simulations [11]. It is also proposed that the very first anisotropic volume expansion of a Si particle in liquid electrolyte was related to the smaller Li diffusion energy barrier at the Si-electrolyte interface along the $\langle 110 \rangle$ direction. Upon completion of this stage, the Li diffusion became isotropic [225]. It is also interesting to note that there existed a critical particle diameter of ~ 150 nm (Fig. 11d) above which the particles tended to fracture due to the formation of surface cracks, according to the statistics of fracture behavior of many c-Si NPs during lithiation. This finding provides invaluable information for the design and synthesis of nanosilicon electrodes [226]. To enrich the understanding of Li-Si reactions, the lithiation process of a-Si NPs was also examined [227,228]. Although the a-Si particles underwent a two-phase transition similar to c-Si during the first lithiation (Figs. 11e-h), there were noticeable differences. The a-Si particle was isotropically lithiated, in contrast to the anisotropic lithiation with a faceted core in the c-Si particle (Fig. 11i), and the concentration of Li in the lithiated a-Si phase was lower than that in the crystalline case. More importantly, the a-Si particles of up to 870 nm in diameter did not fracture, which is a few times larger than the threshold diameter of ~ 150 nm for the c-Si particles [228]. Their different stress states created during lithiation were responsible for the largely enhanced fracture resistance of a-Si particles, according to the chemomechanical models [229,230]. c-Si particles undergo two-phase lithiation with a sharp reaction front where the c-Si core experiences a

compressive hoop stress while the lithiated surface layer experiences a large tensile hoop stress, leading to the initiation and growth of surface cracks. In contrast, a-Si particles are subject to single-phase lithiation after the first cycle, thus the compressive hoop stress prevails over the whole structure. The uniform distribution of stresses in the isotropically expanded a-Si particles also benefits the structural stability of the electrodes.

3.1.2 Lithiation kinetics

The lithiation kinetics of c-Si particles have also been extensively studied. It is found that the movement of reaction front was controlled by the reaction rate at the a-Li_xSi/c-Si interface, instead of Li diffusion speed through the lithiated region. As lithiation continued to propagate towards the Si particle inside, the reaction rate slowed down because the mechanical stresses generated from the volume expansion reduced the thermodynamic driven force, as confirmed by analytical models [231,232]. The lithiation rates of a-Si particles significantly differed from those of c-Si particles, where the lithiation thickness of a-Si particles increased almost linearly with lithiation time. The positive linear relationship was explained by its lower hydrostatic stress that impeded the interface velocity in the reaction front than that in c-Si particles [228]. However, the above explanation of the intriguing phenomenon has not been fully verified by solid evidence, requiring further investigations.

Similar to c-Si particles, the lithiation process in c-Si NWs also became significantly sluggish after the initiation and even stalled due to the large compressive stresses generated at the reaction interface, resulting in a c-Si/a-Li_xSi core/shell NW structure after the reaction [233]. Several important parameters, such as the diameter and electrical conductivity of NWs, controlled the freezing of lithiation in the electrodes. It was demonstrated that the freezing could be avoided by selecting Si NWs of diameters below 38 nm [234]. To establish the relationship between the electrical conductivity and lithiation kinetics or freezing of lithiation, a few Si NWs with different conductivities were prepared and their lithiation behaviors were

examined under *in-situ* TEM [235]. They include pristine Si, phosphorus doped (P-doped) Si, carbon-coated Si and carbon-coated, P-doped Si NWs with different electrical conductivities of 5.95×10^{-3} , 1.05×10^3 , 3.76 and 1.77×10^3 S m⁻¹ (Fig. 11j), respectively. The results revealed that the corresponding lithiation rates of the four Si NWs were 2.3, 20.5, 27.5 and 117.4 nm s⁻¹ (Fig. 11k), respectively, suggesting that enhancing the conductivity of Si NWs was an effective way to improve the reaction kinetics and eliminate the self-limiting lithiation of Si NWs.

3.1.3 Effects of coating layers

It is discussed in Section 2.3 that surface coatings can significantly improve the electrochemical performance of Si-based electrodes, and thus understanding the underlying mechanisms of how these coatings function is vital. For examples, the electrochemical lithiation behaviors of bare Si and carbon-coated Si (Si/C) particles were studied using *in-situ* TEM [143]. The bare Si particles underwent an anisotropic expansion during lithiation, consistent with other reports [226,231]. In contrast, the Si/C particles displayed an isotropic lithiation with spherical shaped a-Li_xSi shell and c-Si core at the initial stage (Fig. 12a), which later transferred to anisotropic lithiation after 30 s. The characteristic isotropic expansion of Si/C particles is attributed to the fact that the thermodynamic driving forces brought by the uniform external voltage [236] and the mechanical stresses through the mechanically robust carbon coating are larger than the neat free energy change in forming Li_xSi, whose process is intrinsically anisotropic [237]. The isotropic expansion is beneficial to structural stability of Si/C particles due to the uniform distribution of mechanical stresses. In addition, the *in-situ* TEM investigations also revealed that the lithiation rate of Si/C particles was 3.5-4 times faster than that of bare Si particles due to the highly conductive and uniform carbon coating. The largely improved reaction kinetics of Si particles by hybridization with conducting materials were also evidenced by *in-situ* TEM studies of many

other Si-based composite electrodes, such as CNT/Si [151], CNF/Si [238], GO/Si [236], SiC-free G/Si [237], Si/C particles [143,239], Si/conducting polymer [240] and Cu/Si NWs [241]. For example, a lithiation rate of $\sim 20 \text{ nm s}^{-1}$ was detected for the Si/CNT composites [151], much faster than $0.07\text{-}3 \text{ nm s}^{-1}$ for the bare Si particles.

In addition to reaction kinetics, there were also changes in degradation mechanism of Si depending on whether Si particles were coated with carbon or not. The damage mode of Si particles was modified from multiple-crack pulverization to single-crack fracture after carbon coating [143], which is beneficial to maintaining the electrically conductive networks between the individual Si particles. The Si particles encapsulated in the CNF matrix presented different damage behaviors. The aggregated Si NPs within the electrospun Si/CNFs underwent significant electrochemical sintering following the large volume expansion of Si particles, causing fracture of the CNF shell (Fig. 12b) [238]. This observation signifies that moderately-filled individual Si NPs, instead of densely-packed agglomerated Si particles, can better achieve enhanced electrochemical performance of Si/CNF composites.

In contrast to the major beneficial effects of most coating layers on Si particles, the *in-situ* TEM examination unexpectedly revealed detrimental roles of coatings on Si [241,242]. For example, the native SiO_x layer on Si NPs reacted with Li to form electrically insulating Li_2O islands, which in turn prevented full lithiation of Si anode by retarding the electron transport. This observation explained the reason behind the low Coulombic efficiencies of LIBs made from partially oxidized Si electrodes [243]. In addition, the PPy coated Si particles (PPy/Si) presented a ‘self-discharging’ or self-delithiation phenomenon during lithiation [244]. As shown in Figs. 12c-f, the PPy/Si particles were lithiated with the $\text{a-Li}_x\text{Si/c-Si}$ reaction front moving inward the Si particle in the first 30 s. However, the reaction front stopped moving inward, but rather it began to move backward, leading to the shrink of lithiated Si particles to its original size after 40 s (Fig. 12f). To elucidate the underlying mechanism of ‘self-

discharge', an analytic model was applied [231,232]:

$$\Delta G_r = \Delta G_r^0 - e\varphi + \frac{1}{x}[\sigma_m^{\text{Si}} \Omega^{\text{Si}} - \sigma_m^{\text{Li}_x\text{Si}} \Omega^{\text{Li}_x\text{Si}}] \quad (16)$$

where ΔG_r is the Gibbs free energy change for the formation of $1/x$ units of Li_xSi at the reaction front, ΔG_r^0 is the neat free energy change of Li-Si alloying, φ is the external voltage applied to Si anode. σ_m^{Si} and $\sigma_m^{\text{Li}_x\text{Si}}$ refer to the mean stresses induced by the Si core and Li_xSi phase, respectively. Ω^{Si} and $\Omega^{\text{Li}_x\text{Si}}$ are the volumes of one Si atom and a Li_xSi unit, respectively. Thus, the last term in the bracket refers to the resistance force arising from the mechanical stresses generated at the reaction front. If the resistance force arising from the compressive stress is larger than the neat free energy change and the external voltage driving force for lithiation, i.e., $\Delta G_r \geq 0$, the motion of the reaction front may be retroacted (Fig. 12g), thus the 'self-discharge' happens. It is also found that the constraint from the PPy coating decreased the tensile stresses in the Si particles, increasing the critical size of Si particles from 150 nm to 380 nm. These observations suggest that it is necessary to identify both the potentially detrimental and beneficial effects of coatings on Si particles when selecting coating materials.

3.1.4 Properties of lithiated silicon

To mitigate the mechanical degradation of Si anodes caused by large volume expansion during lithiation, it is essential to understand their mechanical behaviors. Much progress has been made in identifying the mechanical electrochemical phenomena of Si anodes by *in-situ* TEM and other techniques. For example, a dual probe consisting of atomic force microscopy and scanning tunneling microscopy was used to lithiate a Si NW which was then subjected to an *in-situ* tension in TEM (Fig. 13a) [245]. The Yong's modulus, tensile strength and fracture strain were determined to be 180 GPa, 3.6 GPa and 8 % for the pristine Si NWs and 7.9 GPa, 0.72 GPa and 16 % for the lithiated Si NWs, respectively, suggesting a certain degree of tensile plasticity and softening after lithiation. The lithiation-induced softening behavior was

also detected using other techniques [246,247], as follows. (i) An *ex-situ* nanoindentation was used to measure the hardness and elastic modulus of a Si thin film as a function of lithium concentration. The hardness and Young's modulus decreased from 5 to 1.5 GPa and 92 to 12 GPa after full lithiation[248]. (ii) The hardness of c-Si, a-Li_{3.5}Si and c-Li_{3.75}Si measured by *in-situ* indentation were 14.8, 1.0 and 0.8 GPa, respectively [249]. (iii) A charge-coupled device optical measurement system was developed to *in-situ* monitor the deformation and elastic modulus evolution, presenting a 90 % decrease in elastic modulus of Si composite after lithiation [250]. To understand why lithiation softened Si anodes, the first principles and molecular dynamics simulations were carried out [251–253]. It was revealed that lithium insertion caused the breaking of strong Si-Si bonds and the formation of weak Si-Li bonds, leading to a brittle-to-ductile transition with increasing Li concentration and a concomitant reduction of the Young's modulus. The continuous Li-assisted breaking and reforming of Si-Si bonds and the creation of nanopores during deformation contributed to the large plasticity of lithiated Si.

The fracture resistance of lithiated Si, a critical parameter dictating the structural durability of Si electrode during cycles, has also been studied by *in-situ* TEM. After partial lithiation by Li/Li₂O in TEM, the Si NW was subjected to *in-situ* compression using the Li probe (Fig. 13b) [254]. Interestingly, the c-Si core presented brittle fracture with a flat fracture surface while the a-Li_{3.75}Si shell underwent a large tensile deformation of ~47 % without fracture (Fig. 13c). The nanoindentation of a-Si films revealed that the fracture toughness and fracture energy drastically increased from 0.51 MPa \sqrt{m} and 2.85 J m⁻² for a-Si to 0.77 MPa \sqrt{m} and 8.54 J m⁻² for Li_{1.09}Si. The largely enhanced fracture resistance was explained by molecular dynamics simulations that the local tensile deformation near the crack tip of Li-rich Si (i.e. a-Li_{2.5}Si) was accommodated by the stretching, rotation, breakage and reformation of atomic bonds resulting in blunted crack tip (Fig. 13d). In contrast, the Li-lean Si (i.e. a-Li_{0.5}Si) with

many covalent Si bonds lacked bond reformation and the crack tip remained sharp (Fig. 13e). The high fracture resistance of Li-rich Si provides important implications for designing durable Si anodes under cyclic loading. Also reported, however, was an apparently inconsistent finding in which the fracture energy of lithiated Si was independent of the concentration of lithium and was similar to that of pristine Si [255], requiring further studies for clarification.

3.2 Other *in-situ* techniques

3.2.1 *In-situ* atomic force microscopy

The SEI layers are formed by electrolyte decomposition during discharge, which play an important role in determining the cycle life of Si-based electrodes. Thus, it is necessary to study the formation mechanisms and structural evolution of SEI layers during cycles. Because the properties of SEI layers are very sensitive to sample preparation steps after electrochemical tests, such as washing and cleaning, *in-situ* characterization is an ideal choice to avoid unwanted damage to them. Although *in-situ* TEM provides unique opportunities of probing the reaction mechanisms of individual nanosilicon, the electrode/electrolyte interface in the nano-battery prepared with a solid electrolyte is much different from the situation in real batteries with liquid electrolyte [143]. Instead, the *in-situ* atomic force microscopy (AFM) has emerged as an invaluable tool to probe the SEI layers by scanning the interphase between the electrode and the liquid electrolyte during cycles [256–258]. By probing the heights of an individual Si NW electrode under the AFM tip [256], the formation of initial SEI layer was divided into three stages at different potentials (Fig. 14a): (i) at above 0.4 V, a thin (ca. 5 nm) primary SEI layer grew slowly; (ii) at 0.4-0.1 V, the SEI grew rapidly with a thicker and grainy feature; (iii) at below 0.1 V, the SEI layer kept growing at a much slower speed than the second stage and the Si NW electrode was completely covered by a 22-29 nm thick SEI film (Fig. 14b). The SEI formation behavior on Si surface could differ significantly if a

different electrolyte was used. For example, the SEI film thickness at the steady state after the initial growth was 17-20 nm when the ethylene carbonate (EC) electrolyte was used, whereas the SEI film thickness was 10-12 nm when the propylene carbonate (PC) electrolyte was used [258]. According to the AFM results, the SEI layer was formed during the initial lithiation cycle and remained stable within less than 5 nm variation during the subsequent cycles for both the EC and PC electrolytes, suggesting the stability of SEI layers on the Si thin film electrode. It is worth noting that the *in-situ* AFM has also been applied to study the volume expansion of Si electrodes by scanning the changes in Si film height during reactions (Table 9) [259–261].

3.2.2 *In-situ* scanning electron microscopy

Another limitation of the *in-situ* TEM technique is that it is difficult to show the whole cyclic electrochemical reactions due to its nanoscale working platform and rigorous vacuum environment. An *in-situ* SEM with a good spatial resolution has been developed to study the structural evolution of Si electrodes by placing a LIB cell inside the chamber (Table 9) [262,263]. It is revealed that the height of Si nodules gradually increased from 36 μm of the original state to 80 μm at the 10th cycle, partially confirming the results reported by *in-situ* AFM [256]. This phenomenon, which was responsible for the gradual capacity degradation of Si particle anodes, is attributed to two reasons: (i) the conductive binders and polymer matrix failed to revert to their original morphologies due to the large volume variation of Si particles and (ii) the densities of a-Si and Li_xSi formed during charge/discharge were lower than the pristine c-Si particles. It is also revealed that the bare Si particles underwent electrochemical sintering to form large clusters during cycles, resulting in structural degradation after long cycles [262]. The studies of Si electrodes using *in-situ* SEM are still rare, and in particular the formation of SEI layers and the structural evolution of Si particles upon many cycles would be interesting topics to be probed by *in-situ* SEM.

3.2.3 Other *in situ* techniques

There are other *in-situ* techniques focusing on studying different aspects of Si-based electrodes, as listed in Table 9. For instance, the *in-situ* XRD technique has been applied to study the phase evolution of c-Si electrodes during lithiation/delithiation cycles [264], see Introduction. Apart from the information mentioned in Introduction, it is revealed by *in-situ* XRD analysis that the formation of unwanted c-Li₁₅Si₄ phase in Si NW electrodes could be avoided by devising several modifications to materials and processing parameters, e.g., increasing the lithiation potential to above 70 mV [19], decreasing the thickness of Si film to below 2 μm [265] and modifying the Si NW growth temperature from 450 to 500 °C [266]. These methods offer a useful design guideline for stable cyclic performance of Si electrodes by avoiding c-Li₁₅Si₄ reaction products. *In-situ* ⁷Li nuclear magnetic resonance (NMR) based on the magnetic resonance properties of nuclear isotope ⁷Li has also been used to evaluate the kinetics and reaction processes of Si electrodes on an atomistic level under realistic conditions over multiple cycles [267–270]. The NMR study of the initial discharge process revealed that the crystalline-to-amorphous phase transition occurred via the formation of small Si-Si clusters and isolated Si atoms embedded in the Li matrix where the former was dissolved at the end of discharge, forming isolated Si atoms [268]. These findings are in good agreement with the modeling results mentioned in Introduction. It is also found that the transition from amorphous to crystalline Li₁₅Si₄ process was inhomogeneous at ~50 mV. c-Li₁₅Si₄ was easy to nucleate and grow from the domains of a-Li₁₅Si₄ surrounded by richer isolated Si⁴⁺ anions, resulting in the formation of over-lithiated c-Li_{15+δ}Si₄ and Li-deficient c-Li_{15-δ}Si₄ phases (Fig. 14c). During charge, the Li-deficient c-Li_{15-δ}Si₄ acted as nuclei for the growth of small Si clusters by removing Li ions, which then grew into extended Si networks at above 0.3 V for a-Si formation [269].

In summary, motivated by the synthesis of new electrode materials for rechargeable batteries,

there have been rapid developments of new and accurate tools to characterize their electrochemical performance in the last few years. In particular, *in situ* characterization tools, such as *in situ* TEM, SEM, AFM, XRD and NMR, are now becoming increasingly popular for the evaluation of real-time energy storage behaviors of batteries. It is envisaged that a lot more comprehensive and insightful understanding can be established of the energy storage behaviors of Si electrodes if one of these *in-situ* techniques is combined with another so that a more complete picture can be drawn than one technique acting alone. Another potential improvement can be made by integrating the results obtained from various *ex-situ* techniques, like XPS, electrochemical impedance spectroscopy (EIS) and FTIR, with the aforementioned *in situ* techniques.

4. Application of Si anodes in rechargeable batteries beyond LIBs

The foregoing discussions are mainly focused on Si anodes for LIBs. Apart from LIBs, Si-based anodes have also shown a great potential as electrodes for other types of rechargeable batteries, like Li-sulfur (LSB), Li-O₂ (LOB) and Na-ion batteries (SIB). Significant progress has been made along with numerous studies in employing lithiated Si to replace the dendrite-forming Li metal anodes in LSBs and LOBs. The studies of Si anodes for application in SIBs with potentially high energy densities have appeared recently. The examples of Si anodes applied in these rechargeable batteries beyond LIBs are discussed in the following.

4.1 Li-sulfur batteries

LSBs undergo a redox reaction according to the below equation:



to deliver a high specific capacity of 1672 mAh g⁻¹, a moderate working potential of 2.1 V and an exceptionally high energy density of 2567 Wh kg⁻¹. These intriguing features make LSBs promising candidates to power the next-generation EVs with a capability to drive a

long distance [271,272]. The current LSBs use Li metal as anodes, but the Li metal causes serious safety concerns due to the formation of Li dendrites during cycles. The incorporation of high capacity Si anodes has been proven to be one of the most effective approaches to mitigate the above challenges. Pre-lithiated Si nanostructures with a high Li storage capacity were prepared mainly using a self-discharge process [273,274] and electrochemical lithiation with [275] or without Li-metal [276]. The pre-lithiated Si not only prevented the formation of Li dendrites, but also enhanced the energy density because of the desirable amount of Li. For example, highly reversible LSBs were designed using a dual-type sulfur cathode and a lithiated Si/SiO_x NS anode [277]. The Si/SiO_x anode was pre-lithiated by direct contact with Li metal in an electrolyte, which later served as the Li source in full cells. The cathode consisted of an activated carbon/sulfur composite on a gas diffusion layer as the electrode and an electrolyte containing Li₂S₈, as schematically shown in Fig. 15a. Thanks to the synergy arising from the newly-designed anode and the optimized cathode, the full cell delivered a remarkable specific capacity of ~750 mAh g⁻¹ at 1.675 A g⁻¹ after 500 cycles with 85 % capacity retention (Fig. 15b). This value corresponds to an energy density of 497 Wh kg⁻¹, which is more than three times that of commercial LIBs, ~150 Wh kg⁻¹. It is worth noting that the dissolved polysulfides can react with the lithiated Si anode, which can be alleviated by a Nafion coating on lithiated Si anodes [275]. To further inhibit the dissolution of polysulfides and improve the energy density, a Li_xSi-S battery was prepared using a honeycomb-like sulfur copolymer structure built on the 3D graphene networks as the cathode and a 3D lithiated Si/graphene as the anode. The sulfur copolymer prepared through the copolymerization of elemental sulfur with 1,3-diisopropenylbenzene possessed a high sulfur content of over 90 % and inhibited the dissolution of polysulfides [278]. The full Li_xSi-S cells made from freestanding electrodes without metal current collector delivered an ultrahigh energy density of 1147 Wh kg⁻¹ (based on the total mass of anode and cathode) and excellent

cyclic stability over 500 cycles [279].

Lithium sulfides (Li_2S) with a high theoretical specific capacity of 1166 mAh g^{-1} were also used as the cathode to supply Li and couple with the high capacity Si anodes [280,281]. For instance, a novel $\text{Li}_2\text{S}/\text{Si}$ LSB consisting of a $\text{Li}_2\text{S}/\text{mesoporous carbon}$ composite cathode and a Si NW anode has been reported, as shown in Fig. 15c [281]. It delivered a remarkable theoretical energy density of 1550 Wh kg^{-1} , several times that of $\text{LiCoO}_2/\text{graphite}$ batteries (Fig. 15d). It should be noted that there are important drawbacks arising from the use of Si-based anodes and Li_2S cathodes for full Si-S batteries [282]. They include the high initial irreversible capacity due to the side reactions occurring between Si and electrolyte, the extremely poor electrical conductivity of Li_2S and the decomposition of Li_2S in the presence of oxygen and moisture. All of these issues should be addressed in the future before realizing practical applications of $\text{Li}_2\text{S}/\text{Si}$ full batteries.

4.2 Li- O_2 batteries

LOB is another popular rechargeable energy storage system with an ultrahigh theoretical specific energy density of $\sim 3600 \text{ Wh Kg}^{-1}$ [283]. The redox reaction occurs according to the equation:



Similar to LSBs, the safety issues arising from the Li metal anode have substantially retarded the implementation of LOBs in practical applications. In spite of the tremendous efforts made to address the issues of electrolyte and cathodes, there have been only a few papers involving alternative anodes [284–287], implying great challenges as well as many opportunities for developing Si-based anodes for LOBs. Lithiated Si/C composites first appeared as the anode for LOBs in 2012, and Fig. 16 presents the schematic of $\text{Li}_x\text{Si}-\text{O}_2$ cell structure and its electrochemical behaviors [284]. The reversible reaction of the $\text{Li}_x\text{Si}/\text{O}_2\text{-C}$ cell was verified by the *ex-situ* XRD analysis where the Li_2O_2 peaks appeared after discharging but were

totally absent after charging (Figs. 16b-c). This work also pointed out a limited cycle life of 15 cycles and the gradual voltage decay during cycles at a cut-off capacity of 1000 mAh $\text{g}_{\text{carbon}}^{-1}$, as shown in Fig. 16d. The failure mechanisms of full $\text{Li}_x\text{Si-O}_2$ batteries are still under investigation, and the formation of LiOH on Si anode by a side reaction of moisture in the electrolyte and the Li ions returning from the cathode during charging could be a possible reason [286]. To protect the lithiated Si anode and extend the cycle life of full $\text{Li}_x\text{Si-O}_2$ batteries, a novel fluoroethylene carbonate (FEC) modified electrolyte containing bis(trifluoromethane) sulfonimide salt and tetraglyme solvent has been developed [287]. A strong and deformable SEI film composed of LiF, Li_2CO_3 and polyfluorocarbon was formed on the surface of Si particles during pre-lithiation. The polyfluorocarbon possessed good mechanical flexibility and chemical stability so that the durable SEI film functioned as buffer to accommodate the volume fluctuation of Si as well as passivation layer to prevent the O_2 crossover on the Si anode. As a result, the modified full $\text{Li}_x\text{Si-O}_2$ batteries were sustained up to 100 cycles at a cut-off capacity of 1000 mAh g^{-1} .

4.3 Na-ion batteries

SIBs have attracted tremendous research interest due to many beneficial features of Na, including the abundance of raw materials, low toxicity and low cost. With the particular advantage of low-cost raw materials, SIBs have been considered likely alternative to LIBs for large-scale smart grid applications. Si with a high specific lithium storage capacity naturally has drawn much attention as the anode for SIBs. Unfortunately, the computational analyses of the sodiation of c-Si involved a positive formation energy [288,289] with the reaction process energetically unlikely. This finding is consistent with the negligible capacity observed for the c-Si electrodes in SIBs [290]. In contrast, a-Si was able to absorb 0.76 Na atoms per Si with a negative formation energy of -0.15 eV for $\text{Na}_{0.76}\text{Si}$ (Figs. 17a-b), which value is much higher than -1.1 eV for Li_xSi and corresponds to a theoretical specific capacity

of 725 mAh g⁻¹ with moderate volume expansion of 114 % [291]. There have hitherto been only a few experimental reports on Na ion insertion/extraction in Si anodes with a significant capacity [292–294]. Si NPs of ~20 nm in diameter were prepared by expanding thermal plasma CVD, which consisted of both c-Si and a-Si with a weight ratio of c-Si: a-Si = 0.39:0.61. The Si electrodes displayed initial sodiation/desodiation capacities of 1027/270 mAh g⁻¹ with a very low Coulombic efficiency of 26.3 %. The low Coulombic efficiency was attributed to the formation of excessive SEI layers due to the reaction with native oxide layers. Si/C composites with tunable degrees of crystallinity were synthesized by ball milling of pristine Si and graphite granules for different durations [294]. The Si/graphite composite prepared by 1 h ball milling exhibited a stable cyclic performance with a high capacity of 280 mAh g⁻¹ after 100 cycles at 0.1 A g⁻¹. Although the Coulombic efficiency of the first cycle was only 54.4 % due to the SEI film formation, the efficiencies measured afterwards were almost 100 % (Figs. 17c-d). It seems that the co-existence of a-Si and c-Si phases promoted the Na ion storage in the Si anode, which needs further confirmation.

4.4 Remaining issues of Si anodes beyond LIBs

In addition to the discernable achievements in electrochemical performance of Si anodes beyond LIBs, several fundamental issues involving the synthesis of Li_xSi, the stability of Li_xSi and the reaction of Si with Na warrant further discussion, as follows.

(i) Li_xSi with a large Li storage capacity has been identified as a promising Li-metal free anode for LSBs and LOBs and an excellent prelithiation reagent that can improve the initial Coulombic efficiency of LIBs. Therefore, scalable synthesis of reliable Li_xSi compounds becomes an important issue. Based on a thermodynamic estimate, i.e. $\Delta G = -42 \text{ kJ mol}^{-1}$ for Li_{4.4}Si formation, Li spontaneously reacted with Si to form a Li_xSi alloy so that Li_xSi compounds were prepared by pressing Si and Li metal along with electrolyte in-between [273,274]. Another method is to take advantage of Si-Li phase diagram (Fig. 3a). Li_xSi alloys

were prepared by heating and stirring a stoichiometric mixture of Si particles and Li metal in an Ar-filled glove box [295].

(ii) The as-prepared Li_xSi alloys present extremely high chemical reactivity such that they can easily react with proton-containing solvents, like water and alcohol, and highly polar organic solvents, like N-methyl-2-pyrrolidinone and carbonate. It is reported that the Li_xSi alloys survived only in low polar solvents, such as ether and toluene, while they reacted aggressively with polytetrafluoroethylene polymer binder, leading to poor compatibility with battery synthesis steps [296,297]. In addition, the Li_xSi electrodes in LSBs and LOBs are easily attacked by lithium polysulfides and oxygen molecules as mentioned above. Because ensuring the chemical and structural stability of Li_xSi in full batteries is essential, significant efforts have been made to enhance the stability of Li_xSi in air and humid environment by surface modifications. For example, the $\text{Li}_x\text{Si}/\text{Li}_2\text{O}$ core/shell structure was prepared by exposing Li_xSi particles to dry air [296,297] and an artificial SEI film consisting of LiF and Li alkyl carbonate with long hydrophobic carbon chains was deposited on Li_xSi by reducing 1-fluorodecane on the Li_xSi surface [298]. The dense Li_2O and artificial SEI films effectively prevented further reaction of the underlying Li_xSi with O_2 or moisture.

(iii) The simulation results in Section 4.3 show that the sodiation of c-Si is unfavorable because of the poor binding strength (-0.79 eV) and the high energy barrier for Na diffusion (1.04 eV) [288,289]. Even so, many publications have focused on perfect Si crystals. When defects, such as dislocation, twin boundary and heteroatom doping, are considered, however, the thermodynamic properties and reaction kinetics of SIB using a Si anode are largely different [299,300]. For example, a multi-scale simulation [300] showed that the Si anodes containing 90° partial dislocations enhanced the binding energy of Na to 0.423 eV by providing large space for Na atom insertion while reducing the Na migration barrier to 0.75 eV through fast motion pipe. Although the Si anode can make a promising candidate for SIBs,

there are many unresolved questions, such as the lack of understanding of sodiation mechanisms, reaction kinetics and structural evolution of Si anodes during cycles.

5. Perspectives of Si anodes for practical applications

Although a remarkable progress has been made to enhance the electrochemical performance and to enrich our fundamental understanding of reaction mechanisms of Si-based anodes for high performance rechargeable batteries, there are still many critical issues that have to be fully addressed for large scale use of Si electrodes. They are summarized in the following.

Manufacturing processes. From the view point of massive production and practical applications, Si electrodes with good electrochemical performance should be prepared in a scalable, low-cost and environment-friendly manner. Among all aforementioned manufacturing methods in Section 2.2, MR seems to be the most promising because Si nanostructures with controlled morphologies can be prepared on a large scale and in an environment benign way. Among many different Si precursors, the use of natural materials is considered appealing because of their abundant supply and negligible material costs [110–115]. Natural resources with an intrinsically porous structure are particularly attractive for heat radiation and the preservation of 3D porous structures during reactions. However, several important issues still remain unresolved, including how the purification process of silica can be simplified from the natural resources, how a high conversion yield can be easily achieved and how the porous structure can be stably maintained during reduction. In addition to the abovementioned approaches associated with the preparation of nanosilicon and Si-based composites, the optimization of the properties of binders, electrolytes and current collectors is also important to achieve enhanced performance of Si anodes. Optimal combination of these individual constituents using low-cost, reliable materials and large-scalable fabrication methods have yet to be realized.

Initial Coulombic efficiency. For real-world applications, the ICEs of Si electrodes should be over 90 % similar to that of commercial graphite anodes, but most ICE values listed in [Tables 4, 5, 7 and 8](#) are in the range of 50-85 %. The low ICEs are attributed mainly to (i) the formation of a thick SEI layer due to the large contact area accessed by the liquid electrolyte and (ii) the entrapment of Li ions in carbon, conducting polymer and Si particles. To compensate the significant initial Li loss, several strategies have been proposed: namely, (i) to add commercial microscale Li metal powders as prelithiation reagent [\[301\]](#); (ii) to add Li_xSi NPs as Li donors to the pristine anodes [\[298\]](#); and (iii) to prelithiate the electrode to form an artificial SEI layer before cyclic tests [\[302\]](#). The ICEs of modified Si anodes improved to above 90 % by effective Li ion compensation. However, the microscale Li metals and Li_xSi prelithiation reagents have low potentials and an extremely high chemical reactivity, causing serious compatibility issues with ambient environment, solvents, binders and thermal treatment during the manufacturing of batteries [\[303\]](#). The prelithiation of anodes requires many extra materials/tasks, e.g. a temporary battery consisting of an anode and lithium metal, a long time for Li ions to diffuse across the entire electrode and precise monitoring to check the degree of prelithiation, making this method unsuitable for large-scale production. This means that it still remains a big challenge to achieve high ICEs for nanosilicon electrodes in a feasible, reliable and scalable manner.

Energy density. The Si-based electrodes should deliver high gravimetric/volumetric energy densities sufficient for EV applications. Currently, the Si electrodes are prepared mainly by casting the mixture of active materials, binder and carbon black onto Cu foil current collectors. The gravimetric capacities of above 1000 mAh g^{-1} are usually obtained by calculation based on the active materials, like Si and Si/C. If the weights of other components were taken into account, the real specific capacity of the whole electrode would be lower than 100 mAh g^{-1} , assuming a Si content of 70 wt.%, a Si loading of 1.0 mg cm^{-2} and a Cu areal

density of 7.0 mg cm^{-2} . This estimate is much lower than 200 mAh g^{-1} for the commercial graphite anodes [304]. In addition, the volumetric capacities of Si nanostructures with high porosities and large specific areas are usually not as attractive as their gravimetric capacities: e.g. the porous Si sphere electrodes had a specific capacity of 1800 mAh g^{-1} but their gravimetric capacity was $\sim 760 \text{ mAh cm}^{-3}$ [103]. This value is very similar to $\sim 620 \text{ mAh cm}^{-3}$ of graphite electrodes and far below the theoretical volumetric capacity of Si material, 8322 mAh cm^{-3} . Moreover, in practical LIB configurations, the swelling of external dimension of a battery should also be limited to below 5 % to ensure the structural stability and safety of battery packs. A theoretical analysis [305] reveals that the improvements in volumetric and gravimetric energy densities using Si/C as anode and lithium nickel cobalt aluminum oxide as cathode with a constrained volume change were $\sim 14 \%$ and $\sim 21 \%$, respectively, higher than those of graphite-based LIBs. The amount of Si content is limited to $\sim 11.7 \text{ wt.}\%$ accordingly. Therefore, it can be concluded that although most of Si-based electrodes have high specific capacities, the real volumetric/gravimetric energy densities of full batteries are considerably low and cannot meet the needs for EV applications. Possible solutions to improve the energy density without sacrificing the cycle life of Si electrodes are (i) to prepare free-standing Si-based electrodes with lightweight current collectors like CNF ($\sim 1.5 \text{ mg cm}^{-3}$) and graphene foam ($\sim 1.3 \text{ mg cm}^{-3}$) as discussed in Section 2.3.4; (ii) to synthesize microscale secondary particles/clusters (with a high tap density up to 0.91 g cm^{-3}) using yolk/shell Si/C nanoparticles as building blocks (with a tap density of 0.15 g cm^{-3}) [218,219], see Section 2.4; (iii) to utilize large microscale Si particles coated with highly flexible conducting polymer (i.e. self-healing polymer) [306] or graphene cages [307]; (iv) to couple Si/C anodes with high capacity cathodes to develop new energy storage systems like LSBs and LOBs. Although progress has been made to obtain high energy density Si electrodes, the commercial

applications of these nanosilicon electrodes are still limited by their high costs arising from expensive raw materials and complex synthesis procedures.

Reaction mechanisms and phase evolution. Understanding the phase/morphological evolution of materials on an atomic/molecular level and the failure mechanisms of electrode structure is essential to establishing a design methodology for the synthesis of high-performance Si-based electrodes. Despite the large collections of live data accumulated from the *in-situ* investigation of Si nanostructures, our current understandings of how the SEI layers are formed during cycles, how the interfacial reactions take place between Si and electrolyte and how the Li-Si electrochemical reaction proceeds are still far from complete. In addition, it is demonstrated in Section 2.3 that various coatings made of carbon, conductive polymer and metal (oxides) much improved the electrochemical performance of Si-based electrodes. However, *in-situ* TEM investigations revealed that amorphous carbon coatings were not able to withstand the volume expansion of solid Si particles to maintain the structural integrity [143]. Moreover, the conductive polymer, PPy, induced self-discharge of Si particles due to the strong internal compressive stresses generated during lithiation, which is detrimental to cyclic stability of the electrode [244]. Although the above findings obtained from *in-situ* characterization of nanoscale cells are useful for fundamental understanding, they are insufficient to correctly and clearly explain how the electrochemical performance of real batteries can be improved. It is obvious that further studies, including quantitative analyses, are needed to understand the roles of different coating materials under realistic conditions.

Potential applications. The discussions in Section 4 clearly indicate that Si-based anodes are promising alternatives to Li metal anodes in LSBs and LOBs both of which may provide energy contents far beyond that of the current LIBs. The total specific capacity of commercial LIBs is $\sim 130 \text{ mAh g}^{-1}$ based on the combination of a capacity of $\sim 200 \text{ mAh g}^{-1}$ for lithium

metal oxide cathodes and 372 mAh g⁻¹ for graphite anodes. If these anode and cathode materials are replaced by Li_xSi/C and S/C composites with capacities of ~1500 mAh g⁻¹ and ~1000 mAh g⁻¹, respectively, the Li_xSi/C||S/C batteries are capable of delivering a total specific capacity of ~600 mAh g⁻¹, which is more than four times that of the current LIBs [308]. When considering the working potentials of commercial LIB (~3.6V) and Li_xSi/C||S/C battery (~1.8 V), the specific energy densities are calculated to be ~468 and ~1080 Wh kg⁻¹, respectively, leading to a whopping ~130 % improvement in energy density by the Li_xSi/C||S/C battery [309]. As highlighted in Section 4.2, a substantial progress has been achieved for Li_xSi/S or Si/Li₂S full batteries with long cycle life and high reversible capacities [280,281], but several critical issues need to be addressed in the future. They include (i) the large-scale production of reliable Li_xSi composite electrodes; (ii) the initial irreversible Li consumption caused by the formation of SEI layers; (iii) the elimination of deleterious reactions between the lithium polysulfides and lithiated Si anodes during cycles; and (iv) the moderate energy density obtained by a low output voltage of ~1.8 V for Li_xSi/S full cells. As for LOB and SIB applications, Si anodes have been limitedly explored thus far. Apparently, the use of Si anodes for battery systems beyond LIBs is in their infant stage and there is a large room for exploitation to enrich the knowledge of reaction mechanisms so as to extend their applications in other rechargeable battery systems.

6. Conclusions

Si is a promising, advanced anode material for next generation high capacity rechargeable batteries given its ultrahigh capacity, moderate low working potential, abundant supply and low cost. However, the inherently large volume expansion of Si and the associated structural deficiencies have hindered its practical implementation. Several strategies have been successfully established to address the issue of capacity degradation, including the synthesis

of nanoscale Si architectures and the combination of various functional materials with nanosilicon. In addition, the fundamental understanding of underlying reaction mechanisms ascertained by *in-situ* experiments can offer invaluable insights into and guidelines on how the Si electrodes can be better designed. To extend the application of Si anodes beyond LIBs, there have already been many efforts dedicated to exploring them in other rechargeable battery systems with high energy densities, such as LSBs, LOBs and SIBs.

In this review, an emphasis is laid on the synthesis methods of Si nanostructures and their relative advantages and disadvantages in terms of manufacturing cost, scalability, morphological controllability, environmental impact and electrochemical properties of Si products. After a comprehensive and systematic comparison, it can be said that MR is one of the best choices for preparing high-performance Si nanostructures in mass production. The incorporation of functional coatings, like carbon, conducting polymer and metal (oxides), on nanosilicon enables the Si-based composite electrodes to deliver much enhanced electrochemical properties with long lives, high capacities and excellent reversibility. Several key factors are found to be of significance in enhancing the performance: namely, (i) effective relaxation of mechanical stresses by reducing Si particle size and creating internal/external pores; (ii) stabilization of SEI layers by applying a coating layer(s) or compressing the outward volume expansion; and (iii) enhancing charge transfer by conductive coatings. To disclose the underlying reaction mechanisms, the reaction kinetics, the role of surface coatings, the mechanical properties of lithiated Si and the formation of SEI layers in Si electrodes in real time, *in-situ* TEM and other *in situ* techniques have been successfully developed and utilized.

Over the past two decades, considerable success has been achieved in the design and synthesis of high-performance nanosilicon electrodes and the understanding of their electrochemical reaction behaviors. These achievements not only advanced significantly the

electrochemical properties of Si anodes in LIBs, but also promoted the penetration of Si-based anodes into other promising rechargeable battery systems. Nevertheless, there are several important questions hindering the common application of Si-based anodes in high energy density devices. These challenging issues that need to be continuously explored in the years to come are associated with high manufacturing costs, low initial Coulombic efficiencies, low energy densities of the whole electrodes, and partial or incomplete understanding of the underlying reaction mechanisms.

Acknowledgments

This project was financially supported by the Research Grants Council (GRF projects 613612 and 16212814) and the Innovation and Technology Commission (ITF projects ITS/318/14 and ITS/001/17) of Hong Kong SAR. ZL Xu was partly supported by the SENG PhD Fellowship from the School of Engineering at HKUST.

References

- [1] Tarascon JM, Armand M. Issues and challenges facing rechargeable lithium batteries. *Nature* 2001;414:359–67.
- [2] Armand M, Tarascon JM. Building better batteries. *Nature* 2008;451:652–7.
- [3] Yoo HD, Markevich E, Salitra G, Sharon D, Aurbach D. On the challenge of developing advanced technologies for electrochemical energy storage and conversion. *Mater Today* 2014;17:110–21.
- [4] Nitta N, Wu F, Lee JT, Yushin G. Li-ion battery materials: present and future. *Mater Today* 2015;18:252–64.
- [5] Abouali S, Akbari Garakani M, Zhang B, Luo H, Xu Z, Huang JQ, et al. Co_3O_4 /porous electrospun carbon nanofibers as anodes for high performance Li-ion batteries.

- J Mater Chem A 2014;2:16939–44.
- [6] Abouali S, Akbari Garakani M, Zhang B, Xu ZL, Kamali Heidari E, Huang J, et al. Electrospun carbon nanofibers with in situ encapsulated Co_3O_4 nanoparticles as electrodes for high-performance supercapacitors. ACS Appl Mater Interfaces 2015;7:13503–11.
- [7] Goriparti S, Miele E, De Angelis F, Di Fabrizio E, Proietti Zaccaria R, Capiglia C. Review on recent progress of nanostructured anode materials for Li-ion batteries. J Power Sources 2014;257:421–43.
- [8] Zhang WJ. A review of the electrochemical performance of alloy anodes for lithium-ion batteries. J Power Sources 2011;196:13–24.
- [9] Obrovac MN, Chevrier VL. Alloy negative electrodes for Li-ion batteries. Chem Rev 2014;114:11444–502.
- [10] Siffert P, Krimmel E. Silicon: evolution and future of a technology. Springer 2004.
- [11] Chan MKY, Wolverton C, Greeley JP. First principles simulations of the electrochemical lithiation and delithiation of faceted crystalline silicon. J Am Chem Soc 2012;134:14362–74.
- [12] Schultz ML. Silicon: semiconductor properties. Infrared Phys 1964;4:93–112.
- [13] Okamoto H. Li-Si (Lithium-Silicon). J Phase Equilibria Diffus 2009;30:118–9.
- [14] Sharma RA, Seefurth RN. Thermodynamic properties of the lithium-silicon system. J Electrochem Soc 1976;123:1763–8.
- [15] Wu H, Cui Y. Designing nanostructured Si anodes for high energy lithium ion batteries. Nano Today 2012;7:414–29.
- [16] Boukamp BA, Lesh GC, Huggins RA. All-solid lithium electrodes with mixed-conductor matrix. J Electrochem Soc 1981;128:725.
- [17] Gu M, Wang Z, Connell JG, Perea DE, Lauhon LJ, Gao F, et al. Electronic origin for

- the phase transition from amorphous Li_xSi to crystalline $\text{Li}_{15}\text{Si}_4$. *ACS Nano* 2013;7:6303–9.
- [18] Limthongkul P, Jang Y II, Dudney NJ, Chiang YM. Electrochemically-driven solid-state amorphization in lithium-metal anodes. *J Power Sources* 2003;119:604–9.
- [19] Li J, Dahn JR. An in situ X-ray diffraction study of the reaction of Li with crystalline Si. *J Electrochem Soc* 2007;154:A156.
- [20] Limthongkul P, Jang Y-I, Dudney NJ, Chiang Y-M. Electrochemically-driven solid-state amorphization in lithium-silicon alloys and implications for lithium storage. *Acta Mater* 2003;51:1103–13.
- [21] Li H, Huang X, Chen L, Zhou G, Zhang Z, Yu D, et al. Crystal structural evolution of nano-Si anode caused by lithium insertion and extraction at room temperature. *Solid State Ionics* 2000;135:181–91.
- [22] Liu XH, Wang JW, Huang S, Fan F, Huang X, Liu Y, et al. In situ atomic-scale imaging of electrochemical lithiation in silicon. *Nat Nanotechnol* 2012;7:749–56.
- [23] Lee SW, McDowell MT, Choi JW, Cui Y. Anomalous shape changes of silicon nanopillars by electrochemical lithiation. *Nano Lett* 2011;11:3034–9.
- [24] Kim SP, Datta D, Shenoy VB. Atomistic mechanisms of phase boundary evolution during initial lithiation of crystalline silicon. *J Phys Chem C* 2014;118:17247–53.
- [25] Johari P, Qi Y, Shenoy VB. The mixing mechanism during lithiation of Si negative electrode in Li-ion batteries: An ab-initio molecular-dynamics study. *Nano Lett* 2011;11:5494–500.
- [26] Cubuk ED, Kaxiras E. Theory of structural transformation in lithiated amorphous silicon. *Nano Lett* 2014;14:4065–70.
- [27] Verma P, Maire P, Novák P. A review of the features and analyses of the solid electrolyte interphase in Li-ion batteries. *Electrochim Acta* 2010;55:6332–41.

- [28] Chan CK, Ruffo R, Hong SS, Cui Y. Surface chemistry and morphology of the solid electrolyte interphase on silicon nanowire lithium-ion battery anodes. *J Power Sources* 2009;189:1132–40.
- [29] Ruffo R, Hong SS, Chan CK, Huggins RA, Cui Y. Impedance analysis of silicon nanowire lithium ion battery anodes. *J Phys Chem C* 2009;113:11390–8.
- [30] Soto FA, Ma Y, Martinez de la Hoz JM, Seminario JM, Balbuena PB. Formation and growth mechanisms of solid-electrolyte interphase layers in rechargeable batteries. *Chem Mater* 2015;23:7990–8000.
- [31] Goodenough JB, Kim Y. Challenges for rechargeable batteries. *J Power Sources* 2011;196:6688–94.
- [32] Kasavajjula U, Wang C, Appleby AJ. Nano- and bulk-silicon-based insertion anodes for lithium-ion secondary cells. *J Power Sources* 2007;163:1003–39.
- [33] Szczech JR, Jin S. Nanostructured silicon for high capacity lithium battery anodes. *Energy Environ Sci* 2011;4:56.
- [34] Yin Y, Wan L, Guo Y. Silicon-based nanomaterials for lithium-ion batteries. *Chinese Sci Bull* 2012;57:4104–10. doi:2.
- [35] Su X, Wu Q, Li J, Xiao X, Lott A, Lu W, et al. Silicon-based nanomaterials for lithium-ion Batteries: a review. *Adv Energy Mater* 2014;4:1300882.
- [36] Wu H, Chan G, Choi JW, Ryu I, Yao Y, McDowell MT, et al. Stable cycling of double-walled silicon nanotube battery anodes through solid–electrolyte interphase control. *Nat Nanotechnol* 2012;7:310–5.
- [37] Li X, Zhi L. Managing voids of Si anodes in lithium ion batteries. *Nanoscale* 2013;5:8864–73.
- [38] Peng KQ, Wang X, Li L, Hu Y, Lee ST. Silicon nanowires for advanced energy conversion and storage. *Nano Today* 2013;8:75–97.

- [39] Song T, Hu L, Paik U. One-dimensional silicon nanostructures for Li ion batteries. *J Phys Chem Lett* 2014;5:720–31.
- [40] Ko M, Chae S, Cho J. Challenges in accommodating volume change of Si anodes for Li-ion batteries. *ChemElectroChem* 2015;2:1645–51.
- [41] Rahman MA, Song G, Bhatt AI, Wong YC, Wen C. Nanostructured silicon anodes for high-performance lithium-ion batteries. *Adv Funct Mater* 2016;26:647–78.
- [42] Ashuri M, He Q, Shaw LL. Silicon as a potential anode material for Li-ion batteries: where size, geometry and structure matter. *Nanoscale* 2015;8:74–103.
- [43] Du F, Wang KX, Chen JS. Strategies to succeed in improving the lithium-ion storage properties of silicon nanomaterials. *J Mater Chem A* 2016;4:32–50.
- [44] Liu L, Lyu J, Li T, Zhao T. Well-constructed silicon-based materials as high-performance lithium-ion battery anodes. *Nanoscale* 2016;8:701–22.
- [45] Terranova ML, Orlanducci S, Tamburri E, Guglielmotti V, Rossi M. Si/C hybrid nanostructures for Li-ion anodes: an overview. *J Power Sources* 2014;246:167–77.
- [46] Luo F, Liu B, Zheng J, Chu G, Zhong K, Li H, et al. Nano-silicon/carbon composite anode materials towards practical application for next generation Li-ion batteries. *J Electrochem Soc* 2015;162:A2509–28.
- [47] Zamfir MR, Nguyen HT, Moyon E, Lee YH, Pribat D. Silicon nanowires for Li-based battery anodes: a review. *J Mater Chem A* 2013;1:9566–86.
- [48] Liu XH, Huang JY. In situ TEM electrochemistry of anode materials in lithium ion batteries. *Energy Environ Sci* 2011;4:3844.
- [49] Liu XH, Liu Y, Kushima A, Zhang S, Zhu T, Li J, et al. In situ TEM experiments of electrochemical lithiation and delithiation of individual nanostructures. *Adv Energy Mater* 2012;2:722–41.
- [50] McDowell MT, Lee SW, Nix WD, Cui Y. 25th anniversary article: Understanding the

- lithiation of silicon and other alloying anodes for lithium-ion batteries. *Adv Mater* 2013;25:4966–85.
- [51] Gu M, He Y, Zheng J, Wang C. Nanoscale silicon as anode for Li-ion batteries: The fundamentals, promises, and challenges. *Nano Energy* 2015;17:366–83.
- [52] Roy P, Srivastava SK. Nanostructured anode materials for lithium ion batteries. *J Mater Chem A* 2015;3:2454–84.
- [53] Chen G, Yan L, Luo H, Guo S. Nanoscale engineering of heterostructured anode materials for boosting lithium-ion storage. *Adv Mater* 2016;28:7580–602.
- [54] Woodford WH, Chiang YM, Carter WC. “Electrochemical Shock” of intercalation electrodes: a fracture mechanics analysis. *J Electrochem Soc* 2010;157:A1052–9.
- [55] Zhao K, Pharr M, Vlassak JJ, Suo Z. Inelastic hosts as electrodes for high-capacity lithium-ion batteries. *J Appl Phys* 2011;109:16110.
- [56] Li X, Meduri P, Chen X, Qi W, Engelhard MH, Xu W, et al. Hollow core–shell structured porous Si–C nanocomposites for Li-ion battery anodes. *J Mater Chem* 2012;22:11014.
- [57] Xu ZL, Zhang B, Gang Y, Cao K, Garakani MA, Abouali S, et al. In-situ TEM examination and exceptional long-term cyclic stability of ultrafine Fe₃O₄ nanocrystal/carbon nanofiber composite electrodes. *Energy Storage Mater* 2015;1:25–34.
- [58] Gauthier M, Reyter D, Mazouzi D, Moreau P, Guyomard D, Lestriez B, et al. From Si wafers to cheap and efficient Si electrodes for Li-ion batteries. *J Power Sources* 2014;256:32–6.
- [59] Wang D, Gao M, Pan H, Wang J, Liu Y. High performance amorphous-Si@SiO_x/C composite anode materials for Li-ion batteries derived from ball-milling and in situ carbonization. *J Power Sources* 2014;256:190–9.

- [60] Gauthier M, Mazouzi D, Reyter D, Lestriez B, Moreau P, Guyomard D, et al. A low-cost and high performance ball-milled Si-based negative electrode for high-energy Li-ion batteries. *Energy Environ Sci* 2013;6:2145–55.
- [61] Zhu B, Jin Y, Tan Y, Zong L, Hu Y, Chen L, et al. Scalable production of Si nanoparticles directly from low grade sources for lithium-ion battery anode. *Nano Lett* 2015;15:5750–4.
- [62] Ge M, Lu Y, Ercius P, Rong J, Fang X, Mecklenburg M, et al. Large-scale fabrication, 3D tomography, and lithium-ion battery application of porous silicon. *Nano Lett* 2014;14:261–8.
- [63] Nijhawan S, McMurry PH, Swihart MT, Suh S-M, Girshick SL, Campbell SA, et al. An experimental and numerical study of particle nucleation and growth during low-pressure thermal decomposition of silane. *J Aerosol Sci* 2003;34:691–711.
- [64] Yao Y, McDowell MT, Ryu I, Wu H, Liu N, Hu L, et al. Interconnected silicon hollow nanospheres for lithium-ion battery anodes with long cycle life. *Nano Lett* 2011;11:2949–54.
- [65] Zhang L, Liu X, Zhao Q, Dou S, Liu H, Huang Y, et al. Si-containing precursors for Si-based anode materials of Li-ion batteries: A review. *Energy Storage Mater* 2016;4:92–102.
- [66] Magasinski A, Dixon P, Hertzberg B, Kvit A, Ayala J, Yushin G. High-performance lithium-ion anodes using a hierarchical bottom-up approach. *Nat Mater* 2010;9:353–8.
- [67] Ko M, Chae S, Jeong S, Oh P, Cho J. Elastic a-silicon nanoparticle backboned graphene hybrid as a self-compacting anode for high-rate lithium ion batteries. *ACS Nano* 2014;8:8591–9.
- [68] Lv Q, Liu Y, Ma T, Zhu W, Qiu X. Hollow structured silicon anodes with stabilized solid electrolyte interphase film for lithium-ion batteries. *ACS Appl Mater Interfaces*

- 2015;7:23501–6.
- [69] Chan CK, Peng H, Liu G, McIlwrath K, Zhang XF, Huggins RA, et al. High-performance lithium battery anodes using silicon nanowires. *Nat Nanotechnol* 2008;3:31–5.
- [70] Cui LF, Yang Y, Hsu CM, Cui Y. Carbon-silicon core-shell nanowires as high capacity electrode for lithium ion batteries. *Nano Lett* 2009;9:3370–4.
- [71] Cui LF, Ruffo R, Chan CK, Peng H, Cui Y. Crystalline-amorphous core-shell silicon nanowires for high capacity and high current battery electrodes. *Nano Lett* 2009;9:491–5.
- [72] Park M, Kim MG, Joo J, Kim K, Kim J, Ahn S, et al. Silicon nanotube battery anodes. *Nano Lett* 2009;9:3844–7.
- [73] Song T, Xia J, Lee JH, Lee DH, Kwon MS, Choi JM, et al. Arrays of sealed silicon nanotubes as anodes for lithium ion batteries. *Nano Lett* 2010;10:1710–6.
- [74] Liu J, Li N, Goodman MD, Zhang HG, Epstein ES, Huang B, et al. Mechanically and chemically robust sandwich-structured C@Si@C nanotube array Li-ion battery anodes. *ACS Nano* 2015;9:1985–94.
- [75] Epur R, Hanumantha PJ, Datta MK, Hong D, Gattu B, Kumta PN. A simple and scalable approach to hollow silicon nanotube (h-SiNT) anode architectures of superior electrochemical stability and reversible capacity. *J Mater Chem A* 2015;3:11117–29.
- [76] Jung H, Park M, Han SH, Lim H, Joo SK. Amorphous silicon thin-film negative electrode prepared by low pressure chemical vapor deposition for lithium-ion batteries. *Solid State Commun* 2003;125:387–90.
- [77] Miyazaki R, Ohta N, Ohnishi T, Sakaguchi I, Takada K. An amorphous Si film anode for all-solid-state lithium batteries. *J Power Sources* 2014;272:541–5.
- [78] Pereira-Nabais C, Światowska J, Rosso M, Ozanam F, Seyeux A, Gohier A, et al.

- Effect of lithiation potential and cycling on chemical and morphological evolution of Si thin film electrode studied by ToF-SIMS. *ACS Appl Mater Interfaces* 2014;6:13023–33.
- [79] Li J, Dozier AK, Li Y, Yang F, Cheng YT. Crack pattern formation in thin film lithium-ion battery electrodes. *J Electrochem Soc* 2011;158:A689–94.
- [80] Xiao X, Lu P, Ahn D. Ultrathin multifunctional oxide coatings for lithium ion batteries. *Adv Mater* 2011;23:3911–5.
- [81] McSweeney W, Geaney H, O'Dwyer C. Metal-assisted chemical etching of silicon and the behavior of nanoscale silicon materials as Li-ion battery anodes. *Nano Res* 2015;8:1395–442.
- [82] Morinaga H. Behavior of ultrafine metallic particles on silicon wafer surface. *J Electrochem Soc* 1995;142:966.
- [83] Peng K, Lu A, Zhang R, Lee ST. Motility of metal nanoparticles in silicon and induced anisotropic silicon etching. *Adv Funct Mater* 2008;18:3026–35.
- [84] Jin Y, Zhang S, Zhu B, Tan Y, Hu X, Zong L, et al. Simultaneous purification and perforation of low-grade Si sources for lithium-ion battery anode. *Nano Lett* 2015;15:7742–7.
- [85] Ge M, Rong J, Fang X, Zhang A, Lu Y, Zhou C. Scalable preparation of porous silicon nanoparticles and their application for lithium-ion battery anodes. *Nano Res* 2013;6:174–81.
- [86] Zhong X, Qu Y, Lin YC, Liao L, Duan X. Unveiling the formation pathway of single crystalline porous silicon nanowires. *ACS Appl Mater Interfaces* 2011;3:261–70.
- [87] Ge M, Rong J, Fang X, Zhou C. Porous doped silicon nanowires for lithium ion battery anode with long cycle life. *Nano Lett* 2012;12:2318–23.
- [88] Li X, Yan C, Wang J, Graff A, Schweizer SL, Sprafke A, et al. Stable silicon anodes

- for lithium-ion batteries using mesoporous metallurgical silicon. *Adv Energy Mater* 2015;5.
- [89] Chen Y, Liu L, Xiong J, Yang T, Qin Y, Yan C. Porous Si nanowires from cheap metallurgical silicon stabilized by a surface oxide layer for lithium ion batteries. *Adv Funct Mater* 2015;25:6701–9.
- [90] Bang BM, Kim H, Song H-K, Cho J, Park S. Scalable approach to multi-dimensional bulk Si anodes via metal-assisted chemical etching. *Energy Environ Sci* 2011;4:5013.
- [91] Bang BM, Lee JI, Kim H, Cho J, Park S. High-performance macroporous bulk silicon anodes synthesized by template-free chemical etching. *Adv Energy Mater* 2012;2:878–83.
- [92] Li X, Gu M, Hu S, Kennard R, Yan P, Chen X, et al. Mesoporous silicon sponge as an anti-pulverization structure for high-performance lithium-ion battery anodes. *Nat Commun* 2014;5:4105.
- [93] Bao Z, Weatherspoon MR, Shian S, Cai Y, Graham PD, Allan SM, et al. Chemical reduction of three-dimensional silica micro-assemblies into microporous silicon replicas. *Nature* 2007;446:172–5.
- [94] Yoo JK, Kim J, Choi M-J, Park YU, Hong J, Baek KM, et al. Extremely high yield conversion from low-cost sand to high-capacity Si electrodes for Li-ion batteries. *Adv Energy Mater* 2014;4:1400622.
- [95] Xie J, Wang G, Huo Y, Zhang S, Cao G, Zhao X. Nanostructured silicon spheres prepared by a controllable magnesiothermic reduction as anode for lithium ion batteries. *Electrochim Acta* 2014;135:94–100.
- [96] Chen W, Fan ZL, Dhanabalan A, Chen CH, Wang CL. Mesoporous silicon anodes prepared by magnesiothermic reduction for lithium ion batteries. *J Electrochem Soc* 2011;158:A1055–9.

- [97] Zhong H, Zhan H, Zhou Y-H. Synthesis of nanosized mesoporous silicon by magnesium-thermal method used as anode material for lithium ion battery. *J Power Sources* 2014;262:10–4.
- [98] Chen D, Mei X, Ji G, Lu M, Xie J, Lu J, et al. Reversible lithium-ion storage in silver-treated nanoscale hollow porous silicon particles. *Angew Chemie - Int Ed* 2012;51:2409–13.
- [99] Du FH, Li B, Fu W, Xiong YJ, Wang KX, Chen JS. Surface binding of polypyrrole on porous silicon hollow nanospheres for li-ion battery anodes with high structure stability. *Adv Mater* 2014:6145–50.
- [100] Fang S, Shen L, Xu G, Nie P, Wang J, Dou H, et al. Rational design of void-involved Si@TiO₂ nanospheres as high-performance anode material for lithium-ion batteries. *ACS Appl Mater Interfaces* 2014;6:6497–503.
- [101] Ma Y, Ji G, Ding B, Lee JY. N-doped carbon encapsulation of ultrafine silicon nanocrystallites for high performance lithium ion storage. *J Mater Chem A* 2013;1:13625.
- [102] Li W, Tang Y, Kang W, Zhang Z, Yang X, Zhu Y, et al. Core-shell Si/C nanospheres embedded in bubble sheet-like carbon film with enhanced performance as lithium ion battery anodes. *Small* 2015;11:1345–51.
- [103] Xiao Q, Gu M, Yang H, Li B, Zhang C, Liu Y, et al. Inward lithium-ion breathing of hierarchically porous silicon anodes. *Nat Commun* 2015;6:8844.
- [104] Xu ZL, Gang Y, Garakani MA, Abouali S, Huang JQ, Kim JK. Carbon-coated mesoporous silicon microsphere anodes with greatly reduced volume expansion. *J Mater Chem A* 2016;4:6098–106.
- [105] Yoo JK, Kim J, Lee H, Choi J, Choi M-J, Sim DM, et al. Porous silicon nanowires for lithium rechargeable batteries. *Nanotechnology* 2013;24:424008.

- [106] Fang S, Shen L, Tong Z, Zheng H, Zhang F, Zhang X. Si nanoparticles encapsulated in elastic hollow carbon fibres for Li-ion battery anodes with high structural stability. *Nanoscale* 2015;7:7409–14.
- [107] Lee DJ, Lee H, Ryou MH, Han GB, Lee JN, Song J, et al. Electrospun three-dimensional mesoporous silicon nanofibers as an anode material for high-performance lithium secondary batteries. *ACS Appl Mater Interfaces* 2013;5:12005–10.
- [108] Favors Z, Bay HH, Mutlu Z, Ahmed K, Ionescu R, Ye R, et al. Towards scalable binderless electrodes: carbon coated silicon nanofiber paper via Mg reduction of electrospun SiO₂ nanofibers. *Sci Rep* 2015;5:8246.
- [109] Yoo JK, Kim J, Jung YS, Kang K. Scalable fabrication of silicon nanotubes and their application to energy storage. *Adv Mater* 2012;24:5452–6.
- [110] Favors Z, Wang W, Bay HH, Mutlu Z, Ahmed K, Liu C, et al. Scalable synthesis of nano-silicon from beach sand for long cycle life Li-ion batteries. *Sci Rep* 2014;4:5623.
- [111] Liu N, Huo K, McDowell MT, Zhao J, Cui Y. Rice husks as a sustainable source of nanostructured silicon for high performance Li-ion battery anodes. *Sci Rep* 2013;3:1919.
- [112] Wong DP, Suriyaprabha R, Yuvakumar R, Rajendran V, Chen Y-T, Hwang B-J, et al. Binder-free rice husk-based silicon–graphene composite as energy efficient Li-ion battery anodes. *J Mater Chem A* 2014;2:13437.
- [113] Jung DS, Ryou M-H, Sung YJ, Park S Bin, Choi JW. Recycling rice husks for high-capacity lithium battery anodes. *Proc Natl Acad Sci U S A* 2013;110:12229–34.
- [114] Wang L, Gao B, Peng C, Peng X, Fu J, Chu PK, et al. Bamboo leaf derived ultrafine Si nanoparticles and Si/C nanocomposites for high-performance Li-ion battery anodes. *Nanoscale* 2015;7:13840–7.
- [115] Liu J, Kopold P, van Aken PA, Maier J, Yu Y. Energy storage materials from nature

- through nanotechnology: a sustainable route from reed plants to a silicon anode for lithium-ion batteries. *Angew Chemie* 2015;127:9768–9772.
- [116] Liang J, Li X, Hou Z, Zhang W, Zhu Y, Qian Y. A deep reduction and partial oxidation strategy for fabrication of mesoporous Si anode for lithium ion batteries. *ACS Nano* 2016;10:2295–304.
- [117] Zhang Z, Wang Y, Ren W, Tan Q, Chen Y, Li H, et al. Scalable synthesis of interconnected porous silicon/carbon composites by the Rochow reaction as high-performance anodes of lithium ion batteries. *Angew Chemie Int Ed* 2014;53:5165–9.
- [118] Dai F, Zai J, Yi R, Gordin ML, Sohn H, Chen S, et al. Bottom-up synthesis of high surface area mesoporous crystalline silicon and evaluation of its hydrogen evolution performance. *Nat Commun* 2014;5:3605.
- [119] Kim H, Seo M, Park MH, Cho J. A critical size of silicon nano-anodes for lithium rechargeable batteries. *Angew Chemie - Int Ed* 2010;49:2146–9.
- [120] Song J, Chen S, Zhou M, Xu T, Lv D, Gordin ML, et al. Micro-sized silicon–carbon composites composed of carbon-coated sub-10 nm Si primary particles as high-performance anode materials for lithium-ion batteries. *J Mater Chem A* 2014;2:1257.
- [121] Hwa Y, Park CM, Sohn HJ. Modified SiO as a high performance anode for Li-ion batteries. *J Power Sources* 2013;222:129–34.
- [122] Lee JI, Park S. High-performance porous silicon monoxide anodes synthesized via metal-assisted chemical etching. *Nano Energy* 2013;2:146–52.
- [123] Lee J-I, Choi N-S, Park S. Highly stable Si-based multicomponent anodes for practical use in lithium-ion batteries. *Energy Environ Sci* 2012;5:7878–82.
- [124] Yi R, Dai F, Gordin ML, Sohn H, Wang D. Influence of silicon nanoscale building blocks size and carbon coating on the performance of micro-sized Si-C composite Li-ion anodes. *Adv Energy Mater* 2013;3:1507–15.

- [125] Lu Z, Liu N, Lee HW, Zhao J, Li W, Li Y, et al. Nonfilling carbon coating of porous silicon micrometer-sized particles for high-performance lithium battery anodes. *ACS Nano* 2015;9:2540–7.
- [126] He W, Tian H, Xin F, Han W. Scalable fabrication of micro-sized bulk porous Si from Fe-Si alloy as a high performance anode for lithium-ion batteries. *J Mater Chem A* 2015;3:17956–62.
- [127] Wada T, Yamada J, Kato H. Preparation of three-dimensional nanoporous Si using dealloying by metallic melt and application as a lithium-ion rechargeable battery negative electrode. *J Power Sources* 2016;306:8–16.
- [128] Wang J, Meng X, Fan X, Zhang W, Zhang H, Wang C. Scalable synthesis of defect abundant Si nanorods for high-performance Li-ion battery anodes. *ACS Nano* 2015;9:6576–86.
- [129] Jiang Z, Li C, Hao S, Zhu K, Zhang P. An easy way for preparing high performance porous silicon powder by acid etching Al-Si alloy powder for lithium ion battery. *Electrochim Acta* 2014;115:393–8.
- [130] Tian H, Tan X, Xin F, Wang C, Han W. Micro-sized nano-porous Si/C anodes for lithium ion batteries. *Nano Energy* 2015;11:490–9.
- [131] Hwang G, Park H, Bok T, Choi S, Lee S, Hwang I, et al. A high-performance nanoporous Si/Al₂O₃ foam lithium-ion battery anode fabricated by selective chemical etching of the Al-Si alloy and subsequent thermal oxidation. *Chem Commun* 2015;51:4429–32.
- [132] Jiang H, Zhou X, Liu G, Zhou Y, Ye H, Liu Y, et al. Free-standing Si/graphene paper using Si nanoparticles synthesized by acid-etching Al-Si alloy powder for high-stability Li-ion battery anodes. *Electrochim Acta* 2016;188:777–84.
- [133] Lin N, Han Y, Wang L, Zhou J, Zhou J, Zhu Y, et al. Preparation of nanocrystalline

- silicon from SiCl_4 at 200 °C in molten salt for high-performance anodes for lithium ion batteries. *Angew Chemie - Int Ed* 2015;54:3822–5.
- [134] Lin N, Han Y, Zhou J, Zhang K, Xu T, Zhu Y, et al. A low temperature molten salt process for aluminothermic reduction of silicon oxides to crystalline Si for Li-ion batteries. *Energy Environ Sci* 2015;8:3187–91.
- [135] Huang X, Yang J, Mao S, Chang J, Hallac PB, Fell CR, et al. Controllable synthesis of hollow Si anode for long-cycle-life lithium-ion batteries. *Adv Mater* 2014;26:4326–32.
- [136] Zhang M, Zhang T, Ma Y, Chen Y. Latest development of nanostructured Si/C materials for lithium anode studies and applications. *Energy Storage Mater* 2016;4:1–14.
- [137] Hwa Y, Kim WS, Hong SH, Sohn HJ. High capacity and rate capability of core-shell structured nano-Si/C anode for Li-ion batteries. *Electrochim Acta* 2012;71:201–5.
- [138] Chen S, Gordin ML, Yi R, Howlett G, Sohn H, Wang D. Silicon core–hollow carbon shell nanocomposites with tunable buffer voids for high capacity anodes of lithium-ion batteries. *Phys Chem Chem Phys* 2012;14:12741.
- [139] Wang J, Zhou M, Tan G, Chen S, Wu F, Lu J, et al. Encapsulating micro-nano Si/SiO_x into conjugated nitrogen-doped carbon as binder-free monolithic anodes for advanced lithium ion batteries. *Nanoscale* 2015;7:8023–34.
- [140] Hassan FM, Chabot V, Elsayed AR, Xiao X, Chen Z. Engineered Si electrode nanoarchitecture: a scalable postfabrication treatment for the production of next-generation Li-ion batteries. *Nano Lett* 2014;14:277–83.
- [141] Liu X, Zhang J, Si W, Xi L, Eichler B, Yan C, et al. Sandwich nanoarchitecture of Si/reduced graphene oxide bilayer nanomembranes for Li-ion batteries with long cycle life. *ACS Nano* 2015;9:1198–205.
- [142] Wang B, Li X, Zhang X, Luo B, Zhang Y, Zhi L. Contact-engineered and void-

- involved silicon/carbon nanohybrids as lithium-ion-battery anodes. *Adv Mater* 2013;25:3560–5.
- [143] Xu ZL, Cao K, Abouali S, Akbari Garakani M, Huang J, Huang J-Q, et al. Study of lithiation mechanisms of high performance carbon-coated Si anodes by in-situ microscopy. *Energy Storage Mater* 2016;3:45–54.
- [144] Xu Y, Zhu Y, Wang C. Mesoporous carbon/silicon composite anodes with enhanced performance for lithium-ion batteries. *J Mater Chem A* 2014;2:9751.
- [145] Ma X, Liu M, Gan L, Tripathi PK, Zhao Y, Zhu D, et al. Novel mesoporous Si@C microspheres as anodes for lithium-ion batteries. *Phys Chem Chem Phys* 2014;16:4135–42.
- [146] Shao D, Tang D, Mai Y, Zhang L. Nanostructured silicon/porous carbon spherical composite as a high capacity anode for Li-ion batteries. *J Mater Chem A* 2013;1:15068.
- [147] Liu N, Wu H, McDowell MT, Yao Y, Wang C, Cui Y. A yolk-shell design for stabilized and scalable Li-ion battery alloy anodes. *Nano Lett* 2012;12:3315–21.
- [148] Zhang J, Zhang L, Xue P, Zhang L, Zhang X, Hao W, et al. Silicon-nanoparticles isolated by in situ grown polycrystalline graphene hollow spheres for enhanced lithium-ion storage. *J Mater Chem A* 2015;3:7810–21.
- [149] Wang W, Kumta PN. Nanostructured hybrid silicon/carbon nanotube heterostructures: reversible high-capacity lithium-ion anodes. *ACS Nano* 2010;4:2233–41.
- [150] Hertzberg B, Alexeev A, Yushin G. Deformations in Si-Li anodes upon electrochemical alloying in nano-confined space. *J Am Chem Soc* 2010;132:8548–9.
- [151] Yu W, Liu C, Hou P, Zhang L, Shan X, Li F, et al. Lithiation of silicon nanoparticles confined in carbon nanotubes. *ACS Nano* 2015:5063–71.
- [152] Lin H, Weng W, Ren J, Qiu L, Zhang Z, Chen P, et al. Twisted aligned carbon nanotube/silicon composite fiber anode for flexible wire-shaped lithium-ion battery.

- Adv Mater 2014;26:1217–22.
- [153] Wang W, Ruiz I, Ahmed K, Bay HH, George AS, Wang J, et al. Silicon decorated cone shaped carbon nanotube clusters for lithium ion battery anodes. *Small* 2014;10:3389–96.
- [154] Xiao Q, Fan Y, Wang X, Susantyoko RA, Zhang Q. A multilayer Si/CNT coaxial nanofiber LIB anode with a high areal capacity. *Energy Environ Sci* 2014;7:655.
- [155] Gwon H, Hong J, Kim H, Seo D-H, Jeon S, Kang K. Recent progress on flexible lithium rechargeable batteries. *Energy Environ Sci* 2014;7:538.
- [156] Wang H, Yuan S, Ma D, Zhang X, Yan JM. Electrospun materials for lithium and sodium rechargeable batteries: from structure evolution to electrochemical performance. *Energy Environ Sci* 2015;8:1660–81.
- [157] Zhang B, Kang F, Tarascon JM, Kim JK. Recent advances in electrospun carbon nanofibers and their application in electrochemical energy storage. *Prog Mater Sci* 2016;76:319–80.
- [158] Zhang B, Yu Y, Huang Z, He Y-B, Jang D, Yoon W-S, et al. Exceptional electrochemical performance of freestanding electrospun carbon nanofiber anodes containing ultrafine SnO_x particles. *Energy Environ Sci* 2012;5:9895.
- [159] Zhang B, Huang J, Kim JK. Ultrafine Amorphous SnO_x embedded in carbon nanofiber/carbon nanotube composites for Li-ion and Na-ion batteries. *Adv Funct Mater* 2015;25:5222–8.
- [160] Zhang B, Xu ZL, Kim JK. In situ grown graphitic carbon/Fe₂O₃/carbon nanofiber composites for high performance freestanding anodes in Li-ion batteries. *RSC Adv* 2014;4:12298–301.
- [161] Ji L, Zhang X. Evaluation of Si/carbon composite nanofiber-based insertion anodes for new-generation rechargeable lithium-ion batteries. *Energy Environ Sci* 2010;3:124–9.

- [162] Li Y, Guo B, Ji L, Lin Z, Xu G, Liang Y, et al. Structure control and performance improvement of carbon nanofibers containing a dispersion of silicon nanoparticles for energy storage. *Carbon* 2013;51:185–94.
- [163] Fu K, Xue L, Yildiz O, Li S, Lee H, Li Y, et al. Effect of CVD carbon coatings on Si@CNF composite as anode for lithium-ion batteries. *Nano Energy* 2013;2:976–86.
- [164] Xu ZL, Zhang B, Kim JK. Electrospun carbon nanofiber anodes containing monodispersed Si nanoparticles and graphene oxide with exceptional high rate capacities. *Nano Energy* 2014;6:27–35.
- [165] Lee B-S, Son S, Seo J, Park K, Lee G, Lee S, et al. Facile conductive bridges formed between silicon nanoparticles inside hollow carbon nanofibers. *Nanoscale* 2013;5:4790–6.
- [166] Zhang H, Qin X, Wu J, He Y, Du H, Li B, et al. Electrospun core-shell silicon/carbon fibers with internal honeycomb-like conductive carbon framework as anode for lithium ion batteries. *J Mater Chem A* 2015;3:7112–20.
- [167] Xu ZL, Zhang B, Abouali S, Akbari Garakani M, Huang J, Huang JQ, et al. Nanocavity-engineered Si/multi-functional carbon nanofiber composite anodes with exceptional high-rate capacities. *J Mater Chem A* 2014;2:17944–51.
- [168] Xu ZL, Zhang B, Zhou Z, Abouali S, Akbari Garakani M, Huang J, et al. Carbon nanofibers containing Si nanoparticles and graphene-covered Ni for high performance anodes in Li ion batteries. *RSC Adv* 2014;4:22359.
- [169] Wu H, Zheng G, Liu N, Carney TJ, Yang Y, Cui Y. Engineering empty space between Si nanoparticles for lithium-ion battery anodes. *Nano Lett* 2012;12:904–9.
- [170] Hwang TH, Lee YM, Kong BS, Seo JS, Choi JW. Electrospun core-shell fibers for robust silicon nanoparticle-based lithium ion battery anodes. *Nano Lett* 2012;12:802–7.
- [171] Zhou X, Wan LJ, Guo YG. Electrospun silicon nanoparticle/porous carbon hybrid

- nanofibers for lithium-ion batteries. *Small* 2013;9:2684–8.
- [172] Lee BS, Yang HS, Jung H, Jeon SY, Jung C, Kim SW, et al. Novel multi-layered 1-D nanostructure exhibiting the theoretical capacity of silicon for a super-enhanced lithium-ion battery. *Nanoscale* 2014;6:5989–98.
- [173] Xu C, Xu B, Gu Y, Xiong Z, Sun J, Zhao XS. Graphene-based electrodes for electrochemical energy storage. *Energy Environ Sci* 2013;6:1388.
- [174] Lee JK, Smith KB, Hayner CM, Kung HH. Silicon nanoparticles-graphene paper composites for Li ion battery anodes. *Chem Commun* 2010;46:2025–7.
- [175] Zhou X, Yin YX, Wan LJ, Guo YG. Facile synthesis of silicon nanoparticles inserted into graphene sheets as improved anode materials for lithium-ion batteries. *Chem Commun* 2012;48:2198.
- [176] Luo J, Zhao X, Wu J, Jang HD, Kung HH, Huang J. Crumpled graphene-encapsulated Si nanoparticles for lithium ion battery anodes. *J Phys Chem Lett* 2012;3:1824–9.
- [177] Yang S, Li G, Zhu Q, Pan Q. Covalent binding of Si nanoparticles to graphene sheets and its influence on lithium storage properties of Si negative electrode. *J Mater Chem* 2012;22:3420–5.
- [178] Zhao G, Zhang L, Meng Y, Zhang N, Sun K. Decoration of graphene with silicon nanoparticles by covalent immobilization for use as anodes in high stability lithium ion batteries. *J Power Sources* 2013;240:212–8.
- [179] Wen Y, Zhu Y, Langrock A, Manivannan A, Ehrman SH, Wang C. Graphene-bonded and -encapsulated Si nanoparticles for lithium ion battery anodes. *Small* 2013;9:2810–6.
- [180] Zhou X, Yin YX, Wan LJ, Guo YG. Self-assembled nanocomposite of silicon nanoparticles encapsulated in graphene through electrostatic attraction for lithium-ion batteries. *Adv Energy Mater* 2012;2:1086–90.

- [181] Zhao X, Hayner CM, Kung MC, Kung HH. In-plane vacancy-enabled high-power Si-graphene composite electrode for lithium-ion batteries. *Adv Energy Mater* 2011;1:1079–84.
- [182] Chang J, Huang X, Zhou G, Cui S, Hallac PB, Jiang J, et al. Multilayered Si nanoparticle/reduced graphene oxide hybrid as a high-performance lithium-ion battery anode. *Adv Mater* 2014;26:758–64.
- [183] Li B, Yang S, Li S, Wang B, Liu J. From commercial sponge toward 3D graphene-silicon networks for superior lithium storage. *Adv Energy Mater* 2015;5:1500289.
- [184] Chen S, Bao P, Huang X, Sun B, Wang G. Hierarchical 3D mesoporous silicon@graphene nanoarchitectures for lithium ion batteries with superior performance. *Nano Res* 2014;7:85–94.
- [185] Wang B, Li X, Luo B, Hao L, Zhou M, Zhang X, et al. Approaching the downsizing limit of silicon for surface-controlled lithium storage. *Adv Mater* 2015;27:1526–32.
- [186] Li N, Jin S, Liao Q, Cui H, Wang CX. Encapsulated within graphene shell silicon nanoparticles anchored on vertically aligned graphene trees as lithium ion battery anodes. *Nano Energy* 2014;5:105–15.
- [187] Zhou M, Li X, Wang B, Zhang Y, Ning J, Xiao Z, et al. High-performance silicon battery anodes enabled by engineering graphene assemblies. *Nano Lett* 2015;15:6222–8.
- [188] Liang B, Liu Y, Xu Y. Silicon-based materials as high capacity anodes for next generation lithium ion batteries. *J Power Sources* 2014;267:469–90.
- [189] Chew SY, Guo ZP, Wang JZ, Chen J, Munroe P, Ng SH, et al. Novel nano-silicon/polypyrrole composites for lithium storage. *Electrochem Commun* 2007;9:941–6.
- [190] Li J, Huang J. A nanofibrous polypyrrole/silicon composite derived from cellulose

- substance as the anode material for lithium-ion batteries. *Chem Commun* 2015;51:14590–3.
- [191] Du Z, Zhang S, Liu Y, Zhao J, Lin R, Jiang T. Facile fabrication of reticular polypyrrole-silicon core-shell nanofibers for high performance lithium storage. *J Mater Chem* 2012;22:11636–41.
- [192] Liu B, Soares P, Checkles C, Zhao Y, Yu G. Three-dimensional hierarchical ternary nanostructures for high-performance Li-ion battery anodes. *Nano Lett* 2013;13:3414–9.
- [193] Wu H, Yu G, Pan L, Liu N, McDowell MT, Bao Z, et al. Stable Li-ion battery anodes by in-situ polymerization of conducting hydrogel to conformally coat silicon nanoparticles. *Nat Commun* 2013;4:1943.
- [194] Lin H-Y, Li C-H, Wang D-Y, Chen C-C. Chemical doping of a core-shell silicon nanoparticles@polyaniline nanocomposite for the performance enhancement of a lithium ion battery anode. *Nanoscale* 2016;8:1280–7.
- [195] Mi H, Li F, He C, Chai X, Zhang Q, Li C, et al. Three-dimensional network structure of silicon-graphene-polyaniline composites as high performance anodes for Lithium-ion batteries. *Electrochim Acta* 2015;190:1032–40.
- [196] Yao Y, Liu N, McDowell MT, Pasta M, Cui Y. Improving the cycling stability of silicon nanowire anodes with conducting polymer coatings. *Energy Environ Sci* 2012;5:7927.
- [197] Yue L, Wang S, Zhao X, Zhang L. Nano-silicon composites using poly(3,4-ethylenedioxythiophene):poly(styrenesulfonate) as elastic polymer matrix and carbon source for lithium-ion battery anode. *J Mater Chem* 2011;22:1094–9.
- [198] Chen Z, To JWF, Wang C, Lu Z, Liu N, Chortos A, et al. A three-dimensionally interconnected carbon nanotube-conducting polymer hydrogel network for high-performance flexible battery electrodes. *Adv Energy Mater* 2014;4:1400207.

- [199] Yu Y, Gu L, Zhu C, Tsukimoto S, van Aken PA, Maier J. Reversible storage of lithium in silver-coated three-dimensional macroporous silicon. *Adv Mater* 2010;22:2247–50.
- [200] Yoo S, Lee JI, Ko S, Park S. Highly dispersive and electrically conductive silver-coated Si anodes synthesized via a simple chemical reduction process. *Nano Energy* 2013;2:1271–8.
- [201] Song H, Wang HX, Lin Z, Jiang X, Yu L, Xu J, et al. Highly connected silicon-copper alloy mixture nanotubes as high-rate and durable anode materials for lithium-ion batteries. *Adv Funct Mater* 2016;26:524–31.
- [202] Zhang L, Guo H, Rajagopalan R, Hu X, Huang Y, Dou SX, et al. One-step synthesis of a silicon/hematite@carbon hybrid nanosheet/silicon sandwich-like composite as an anode material for Li-ion batteries. *J Mater Chem A* 2016;4:4056–61.
- [203] Ren W, Wang C, Lu L, Li D, Cheng C, Liu J. SnO₂@Si core-shell nanowire arrays on carbon cloth as a flexible anode for Li ion batteries. *J Mater Chem A* 2013;1:13433.
- [204] Hwa Y, Kim WS, Yu BC, Hong SH, Sohn HJ. Enhancement of the cyclability of a Si anode through Co₃O₄ coating by the sol-gel method. *J Phys Chem C* 2013;117:7013–7.
- [205] Lee J, Ko Y, Shin M, Song H, Choi N-S, Kim MG, et al. High-performance silicon-based multicomponent battery anodes produced via synergistic coupling of multifunctional coating layers. *Energy Environ Sci* 2015;8:2075–84.
- [206] Kohandehghan A, Cui K, Kupsta M, Memarzadeh E, Kalisvaart P, Mitlin D. Nanometer-scale Sn coatings improve the performance of silicon nanowire LIB anodes. *J Mater Chem A* 2014;2:11261–79.
- [207] Kennedy T, Bezuidenhout M, Palaniappan K, Stokes K, Brandon M, Ryan KM. Nanowire heterostructures comprising germanium stems and silicon branches as high-capacity Li-ion anodes with tunable rate capability. *ACS Nano* 2015;9:7456–65.

- [208] Liu J, Song K, Zhu C, Chen C, van Aken PA, Maier J, et al. Ge/C nanowires as high-capacity and long-life anode materials for Li-ion batteries. *ACS Nano* 2014;8:7051–9.
- [209] Jeong G, Kim JG, Park MS, Seo M, Hwang SM, Kim YU, et al. Core-shell structured silicon nanoparticles@TiO_{2-x}/carbon mesoporous microfiber composite as a safe and high-performance lithium-ion battery anode. *ACS Nano* 2014;8:2977–85.
- [210] Lee BS, Yoon J, Jung C, Kim DY, Jeon SY, Kim K-H, et al. Silicon/carbon nanotube/BaTiO₃ nanocomposite anode: evidence for enhanced lithium-ion mobility induced by the local piezoelectric potential. *ACS Nano* 2016;10:2617–27.
- [211] Sim S, Oh P, Park S, Cho J. Critical thickness of SiO₂ coating layer on core@shell bulk@nanowire Si anode materials for Li-ion batteries. *Adv Mater* 2013;25:4498–503.
- [212] Park E, Yoo H, Lee J, Park M-S, Kim Y-J, Kim H. Dual-size silicon nanocrystal-embedded SiO_x nanocomposite as a high-capacity lithium storage material. *ACS Nano* 2015;9:7690–6.
- [213] Choi S, Jung DS, Choi JW. Scalable fracture-free SiOC glass coating for robust silicon nanoparticle anodes in lithium secondary batteries. *Nano Lett* 2014;14:7120–5.
- [214] Aricò AS, Bruce PG, Scrosati B, Tarascon J-M, Van Schalkwijk W. Nanostructured materials for advanced energy conversion and storage devices. *Nat Mater* 2005;4:366–77.
- [215] Bruce PG, Scrosati B, Tarascon J-M. Nanomaterials for rechargeable lithium batteries. *Angew Chem Int Ed* 2008;47:2930–46.
- [216] Guo YG, Hu JS, Wan LJ. Nanostructured materials for electrochemical energy conversion and storage devices. *Adv Mater* 2008;20:2878–87.
- [217] Sun Y, Liu N, Cui Y. Promises and challenges of nanomaterials for lithium-based rechargeable batteries. *Nat Energy* 2016;1:16071.
- [218] Liu N, Lu Z, Zhao J, McDowell MT, Lee H, Zhao W, et al. A pomegranate-inspired

- nanoscale design for large-volume-change lithium battery anodes. *Nat Nanotechnol* 2014;9:187–92.
- [219] Lin D, Lu Z, Hsu P, Lee HR, Liu N, Zhao J, et al. A high tap density secondary silicon particle anode fabricated by scalable mechanical pressing for lithium-ion batteries. *Energy Environ Sci* 2015;8:2371–6.
- [220] Zhao H, Yuan W, Liu G. Hierarchical electrode design of high-capacity alloy nanomaterials for lithium-ion batteries. *Nano Today* 2015;10:1–20.
- [221] Choi N, Ha S, Lee Y, Jang JY, Jeong M, Shin WC, et al. Recent progress on polymeric binders for silicon anodes in lithium-ion batteries. *J Electrochem Sci Technol* 2015;6:35–49.
- [222] Mazouzi D, Karkar Z, Reale Hernandez C, Jimenez Manero P, Guyomard D, Roué L, et al. Critical roles of binders and formulation at multiscales of silicon-based composite electrodes. *J Power Sources* 2015;280:533–49.
- [223] Yao S, Cui J, Lu Z, Xu ZL, Qin L, Huang J, et al. Unveiling the unique phase transformation behavior and sodiation kinetics of 1D van der Waals Sb_2S_3 anodes for sodium ion batteries. *Adv Energy Mater* 2017; 7:1602149.
- [224] Liu XH, Zheng H, Zhong L, Huang S, Karki K, Zhang LQ, et al. Anisotropic swelling and fracture of silicon nanowires during lithiation. *Nano Lett* 2011;11:3312–8.
- [225] Yuk JM, Seo HK, Choi JW, Lee JY. Anisotropic lithiation onset in silicon nanoparticle anode revealed by in situ graphene liquid cell electron microscopy. *ACS Nano* 2014;8:7478–85.
- [226] Liu XH, Zhong L, Huang S, Mao SX, Zhu T, Huang JY. Size-dependent fracture of silicon nanoparticles during lithiation. *ACS Nano* 2012;6:1522–31.
- [227] Wang JW, He Y, Fan F, Liu XH, Xia S, Liu Y, et al. Two-phase electrochemical lithiation in amorphous silicon. *Nano Lett* 2013;13:709–15.

- [228] McDowell MT, Lee SW, Harris JT, Korgel BA, Wang C, Nix WD, et al. In situ TEM of two-phase lithiation of amorphous silicon nanospheres. *Nano Lett* 2013;13:758–64.
- [229] McDowell MT, Xia S, Zhu T. The mechanics of large-volume-change transformations in high-capacity battery materials. *Extrem Mech Lett* 2016;9:480–94.
- [230] Zhao K, Cui Y. Understanding the role of mechanics in energy materials: A perspective. *Extrem Mech Lett* 2016;9:347–52.
- [231] McDowell MT, Ryu I, Lee SW, Wang C, Nix WD, Cui Y. Studying the kinetics of crystalline silicon nanoparticle lithiation with in situ transmission electron microscopy. *Adv Mater* 2012;24:1–8.
- [232] Zhao K, Pharr M, Wan Q, Wang WL, Kaxiras E, Vlassak JJ, et al. Concurrent reaction and plasticity during initial lithiation of crystalline silicon in lithium-ion batteries. *J Electrochem Soc* 2012;159:A238.
- [233] Liu XH, Fan F, Yang H, Zhang S, Huang JY, Zhu T. Self-limiting lithiation in silicon nanowires. *ACS Nano* 2013;7:1495–503.
- [234] Wang L, Liu D, Yang S, Tian X, Zhang G, Wang W, et al. Exotic reaction front migration and stage structure in lithiated silicon nanowires. *ACS Nano* 2014;8:8249–54.
- [235] Liu XH, Zhang LQ, Zhong L, Liu Y, Zheng H, Wang JW, et al. Ultrafast electrochemical lithiation of individual Si nanowire anodes. *Nano Lett* 2011;11:2251–8.
- [236] Luo L, Wu J, Luo J, Huang J, Dravid VP. Dynamics of electrochemical lithiation/delithiation of graphene-encapsulated silicon nanoparticles studied by in-situ TEM. *Sci Rep* 2014;4:3863.
- [237] Son IH, Hwan Park J, Kwon S, Park S, Rummeli MH, Bachmatiuk A, et al. Silicon carbide-free graphene growth on silicon for lithium-ion battery with high volumetric

- energy density. *Nat Commun* 2015;6:7393.
- [238] Gu M, Li Y, Li X, Hu S, Zhang X, Xu W, et al. In situ TEM study of lithiation behavior of silicon nanoparticles attached to and embedded in a carbon matrix. *ACS Nano* 2012;6:8439–47.
- [239] Xiao X, Zhou W, Kim Y, Ryu I, Gu M, Wang C, et al. Regulated breathing effect of silicon negative electrode for dramatically enhanced performance of Li-ion battery. *Adv Funct Mater* 2015;25:1426–33.
- [240] Gu M, Xiao X, Liu G, Thevuthasan S, Baer DR, Zhang JG, et al. Mesoscale origin of the enhanced cycling-stability of the Si-conductive polymer anode for Li-ion batteries. *Sci Rep* 2014;4:3684.
- [241] McDowell MT, Woo Lee S, Wang C, Cui Y. The effect of metallic coatings and crystallinity on the volume expansion of silicon during electrochemical lithiation/delithiation. *Nano Energy* 2012;1:401–10.
- [242] Luo L, Yang H, Yan P, Travis JJ, Lee Y, Liu N, et al. Surface-coating regulated lithiation kinetics and degradation in silicon nanowires for lithium ion battery. *ACS Nano* 2015;9:5559–66.
- [243] He Y, Piper DM, Gu M, Travis JJ, George SM, Lee S, et al. In situ transmission electron microscopy probing of native oxide and artificial layers on silicon nanoparticles for lithium ion batteries. *ACS Nano* 2014;8:11816–23.
- [244] Luo L, Zhao P, Yang H, Liu B, Zhang JG, Cui Y, et al. Surface coating constraint induced self-discharging of silicon nanoparticles as anodes for lithium ion batteries. *Nano Lett* 2015;15:7016–22.
- [245] Kushima A, Huang JY, Li J. Quantitative fracture strength and plasticity measurements of lithiated silicon nanowires by in situ TEM tensile experiments. *ACS Nano* 2012;6:9425–32.

- [246] Chon MJ, Sethuraman VA, McCormick A, Srinivasan V, Guduru PR. Real-time measurement of stress and damage evolution during initial lithiation of crystalline silicon. *Phys Rev Lett* 2011;107:45503.
- [247] Zhao K, Pharr M, Cai S, Vlassak JJ, Suo Z. Large plastic deformation in high-capacity lithium-ion batteries caused by charge and discharge. *J Am Ceram Soc* 2011;94:226–35.
- [248] Hertzberg B, Benson J, Yushin G. Ex-situ depth-sensing indentation measurements of electrochemically produced Si-Li alloy films. *Electrochem Commun* 2011;13:818–21.
- [249] Epler E, Roddatis V V., Volkert CA. Measuring mechanical properties during the electrochemical lithiation of silicon. *Energy Technol* 2016;4:1575–81.
- [250] Xie H, Qiu W, Song H, Tian J. In situ measurement of the deformation and elastic modulus evolution in Si composite electrodes during electrochemical lithiation and delithiation. *J Electrochem Soc* 2016;163:A2685–90.
- [251] Huggins RA, Nix WD. Decrepitation model for capacity loss during cycling of alloys in rechargeable electrochemical systems. *Ionics* 2000;6:57–63.
- [252] Shenoy VB, Johari P, Qi Y. Elastic softening of amorphous and crystalline Li-Si Phases with increasing Li concentration: A first-principles study. *J Power Sources* 2010;195:6825–30.
- [253] Zhao KJ, Wang WL, Gregoire J, Pharr M, Suo ZG, Vlassak JJ, et al. Lithium-assisted plastic deformation of silicon electrodes in lithium-ion batteries: a first-principles theoretical study. *Nano Lett* 2011;11:2962–7.
- [254] Wang X, Fan F, Wang J, Wang H, Tao S, Yang A, et al. High damage tolerance of electrochemically lithiated silicon. *Nat Commun* 2015;6:8417.
- [255] Pharr M, Suo Z, Vlassak JJ. Measurements of the fracture energy of lithiated silicon electrodes of Li-Ion batteries. *Nano Lett* 2013;13:5570–7.

- [256] Liu XR, Deng X, Liu RR, Yan HJ, Guo YG, Wang D, et al. Single nanowire electrode electrochemistry of silicon anode by in situ atomic force microscopy: Solid electrolyte interphase growth and mechanical properties. *ACS Appl Mater Interfaces* 2014;6:20317–23.
- [257] Tokranov A, Sheldon BW, Li C, Minne S, Xiao X. In situ atomic force microscopy study of initial solid electrolyte interphase formation on silicon electrodes for Li-ion batteries. *ACS Appl Mater Interfaces* 2014;6:6672–86.
- [258] Yoon I, Abraham DP, Lucht BL, Bower AF, Guduru PR. In situ measurement of solid electrolyte interphase evolution on silicon anodes using atomic force microscopy. *Adv Energy Mater* 2016; 6:1600099.
- [259] Beaulieu LY, Beattie SD, Hatchard TD, Dahn JR. The Electrochemical reaction of lithium with alloy thin films studied by in situ AFM. *J Electrochem Soc* 2003;150:A419.
- [260] Becker CR, Strawhecker KE, McAllister QP, Lundgren CA. In situ atomic force microscopy of lithiation and delithiation of silicon nanostructures for lithium ion batteries. *ACS Nano* 2013;7:9173–82.
- [261] Becker CR, Prokes SM, Love CT. Enhanced lithiation cycle stability of ALD-coated confined a-Si microstructures determined using in situ AFM. *ACS Appl Mater Interfaces* 2016;8:53–537.
- [262] Hovington P, Dontigny M, Guerfi A, Trottier J, Lagacé M, Mauger A, et al. In situ scanning electron microscope study and microstructural evolution of nano silicon anode for high energy Li-ion batteries. *J Power Sources* 2014;248:457–64.
- [263] Tsuda T, Kanetsuku T, Sano T, Oshima Y, Ui K, Yamagata M, et al. In situ SEM observation of the Si negative electrode reaction in an ionic-liquid-based lithium-ion secondary battery. *Microscopy* 2015;64:159–68.

- [264] Nelson Weker J, Toney MF. Emerging in situ and operando nanoscale X-ray imaging techniques for energy storage materials. *Adv Funct Mater* 2015;25:1622–37.
- [265] Hatchard TD, Dahn JR. In situ XRD and electrochemical study of the reaction of lithium with amorphous silicon. *J Electrochem Soc* 2004;151:A838–42.
- [266] Misra S, Liu N, Nelson J, Hong SS, Cui Y, Toney MF. In situ X-ray diffraction studies of (de) lithiation mechanism in silicon nanowire anodes. *ACS Nano* 2012;6:5465–73.
- [267] Harks PPRML, Mulder FM, Notten PHL. In situ methods for Li-ion battery research: A review of recent developments. *J Power Sources* 2015;288:92–105.
- [268] Key B, Bhattacharyya R, Morcrette M, Seznéc V, Tarascon J, Grey CP. Real-time NMR investigations of structural changes in silicon electrodes for lithium-ion batteries. *J Am Chem Soc* 2009;131:9239–49.
- [269] Ogata K, Salager E, Kerr CJ, Fraser A E, Ducati C, Morris a J, et al. Revealing lithium-silicide phase transformations in nano-structured silicon-based lithium ion batteries via in situ NMR spectroscopy. *Nat Commun* 2014;5:3217.
- [270] Key B, Morcrette M, Tarascon J-M, Grey CP. Pair distribution function analysis and solid state NMR studies of silicon electrodes for lithium ion batteries: understanding the (de)lithiation mechanisms. *J Am Chem Soc* 2011;133:503–12.
- [271] Bruce PG, Freunberger SA, Hardwick LJ, Tarascon J-M. Li–O₂ and Li–S batteries with high energy storage. *Nat Mater* 2011;11:172–172.
- [272] Xu ZL, Huang JQ, Chong WG, Qin X, Wang X, Zhou L, et al. In situ TEM study of volume expansion in porous carbon nanofiber/sulfur cathodes with exceptional high-rate performance. *Adv Energy Mater* 2017; 7:1602078.
- [273] Liu N, Hu L, McDowell MT, Jackson A, Cui Y. Prelithiated silicon nanowires as an anode for lithium ion batteries. *ACS Nano* 2011;5:6487–93.
- [274] Hassoun J, Kim J, Lee DJ, Jung HG, Lee SM, Sun YK, et al. A contribution to the

- progress of high energy batteries: A metal-free, lithium-ion, silicon-sulfur battery. *J Power Sources* 2012;202:308–13.
- [275] Shen C, Ge M, Zhang A, Fang X, Liu Y, Rong J, et al. Silicon(lithiated)-sulfur full cells with porous silicon anode shielded by Nafion against polysulfides to achieve high capacity and energy density. *Nano Energy* 2016;19:68–77.
- [276] Zhou H, Wang X, Chen D. Li-metal-free prelithiation of Si-based negative electrodes for full Li-ion batteries. *ChemSusChem* 2015;8:2737–44.
- [277] Lee SK, Oh SM, Park E, Scrosati B, Hassoun J, Park MS, et al. Highly cyclable lithium-sulfur batteries with a dual-type sulfur cathode and a lithiated Si/SiO_x nanosphere anode. *Nano Lett* 2015;15:2863–8.
- [278] Chung WJ, Griebel JJ, Kim ET, Yoon H, Simmonds AG, Ji HJ, et al. The use of elemental sulfur as an alternative feedstock for polymeric materials. *Nat Chem* 2013;5:518–24.
- [279] Li B, Li S, Xu J, Yang S. A new configured lithiated silicon–sulfur battery built on 3D graphene with superior electrochemical performances. *Energy Environ Sci* 2016;9:2025–30.
- [280] Agostini M, Hassoun J, Liu J, Jeong M, Nara H, Momma T, et al. A lithium-ion sulfur battery based on a carbon-coated lithium-sulfide cathode and an electrodeposited silicon-based anode. *ACS Appl Mater Interfaces* 2014;6:10924–8.
- [281] Yang Y, McDowell MT, Jackson A, Cha JJ, Hong SS, Cui Y. New nanostructured Li₂S/silicon rechargeable battery with high specific energy. *Nano Lett* 2010;10:1486–91.
- [282] Son Y, Lee JS, Son Y, Jang JH, Cho J. Recent advances in lithium sulfide cathode materials and their use in lithium sulfur batteries. *Adv Energy Mater* 2015;5:1500110.
- [283] Li F, Zhang T, Zhou H. Challenges of non-aqueous Li-O₂ batteries: electrolytes,

- catalysts, and anodes. *Energy Environ Sci* 2013;6:1125–41.
- [284] Hassoun J, Jung HG, Lee DJ, Park JB, Amine K, Sun YK, et al. A metal-free, lithium-ion oxygen battery: A step forward to safety in lithium-air batteries. *Nano Lett* 2012;12:5775–9.
- [285] Teranishi R, Si Q, Mizukoshi F, Kawakubo M, Matsui M, Takeda Y, et al. Silicon anode for rechargeable aqueous lithium–air batteries. *J Power Sources* 2015;273:538–43.
- [286] Kwak W-J, Shin H-J, Reiter J, Tsiouvaras N, Hassoun J, Passerini S, et al. Understanding problems of lithiated anodes in lithium oxygen full-cells. *J Mater Chem A* 2016;4:10467–71.
- [287] Wu S, Zhu K, Tang J, Liao K, Bai S, Yi J, et al. A long-life lithium ion oxygen battery based on commercial silicon particles as the anode. *Energy Environ Sci* 2016;9:3262–71.
- [288] Malyi O, Kulish V V., Tan TL, Manzhos S. A computational study of the insertion of Li, Na, and Mg atoms into Si(111) nanosheets. *Nano Energy* 2013;2:1149–57.
- [289] Legrain F, Malyi OI, Manzhos S. Comparative computational study of the energetics of Li, Na, and Mg storage in amorphous and crystalline silicon. *Comput Mater Sci* 2014;94:214–7.
- [290] Komaba S, Matsuura Y, Ishikawa T, Yabuuchi N, Murata W, Kuze S. Redox reaction of Sn-polyacrylate electrodes in aprotic Na cell. *Electrochem Commun* 2012;21:65–8.
- [291] Jung SC, Jung DS, Choi JW, Han YK. Atom-level understanding of the sodiation process in silicon anode material. *J Phys Chem Lett* 2014;5:1283–8.
- [292] Xu Y, Swaans E, Basak S, Zandbergen HW, Borsa DM, Mulder FM. Reversible Na-ion uptake in Si nanoparticles. *Adv Energy Mater* 2016;6:1501436.
- [293] Lim C-H, Huang T-Y, Shao P-S, Chien J-H, Weng Y-T, Huang H-F, et al.

- Experimental study on sodiation of amorphous silicon for use as sodium-ion battery anode. *Electrochim Acta* 2016;211:265–72.
- [294] Zhao Q, Huang Y, Hu X. A Si/C nanocomposite anode by ball milling for highly reversible sodium storage. *Electrochem Commun* 2016;70:8–12.
- [295] Iwamura S, Nishihara H, Ono Y, Morito H, Yamane H, Nara H, et al. Li-rich Li-Si alloy as a lithium-containing negative electrode material towards high energy lithium-ion batteries. *Sci Rep* 2015;5:25–7.
- [296] Zhao J, Lee H-W, Sun J, Yan K, Liu Y, Liu W, et al. Metallurgically lithiated SiO_x anode with high capacity and ambient air compatibility. *Proc Natl Acad Sci* 2016;113:7408–13.
- [297] Zhao J, Lu Z, Liu N, Lee H-W, McDowell MT, Cui Y. Dry-air-stable lithium silicide–lithium oxide core–shell nanoparticles as high-capacity prelithiation reagents. *Nat Commun* 2014;5:5088.
- [298] Zhao J, Lu Z, Wang H, Liu W, Lee H-W, Yan K, et al. Artificial solid electrolyte interphase-protected Li_xSi nanoparticles: an efficient and stable prelithiation reagent for lithium-ion batteries. *J Am Chem Soc* 2015;137:8372–5.
- [299] Wang C, Sun X, Li C, Wu G, Wang B, Wang Z, et al. Effects of defect on the storage and diffusion of Na and Mg interstitials in Si anode. *J Alloy Compd* 2016;654:157–62.
- [300] Legrain F, Manzhos S. Aluminum doping improves the energetics of lithium, sodium, and magnesium storage in silicon: A first-principles study. *J Power Sources* 2015;274:65–70.
- [301] Zhao H, Wang Z, Lu P, Jiang M, Shi F, Song X, et al. Toward practical application of functional conductive polymer binder for a high-energy lithium-ion battery design. *Nano Lett* 2014;14:6704–10.

- [302] Kim HJ, Choi S, Lee SJ, Seo MW, Lee JG, Deniz E, et al. Controlled prelithiation of silicon monoxide for high performance lithium-ion rechargeable full cells. *Nano Lett* 2016;16:282–8.
- [303] Sun Y, Lee H-W, Seh ZW, Liu N, Sun J, Li Y, et al. High-capacity battery cathode prelithiation to offset initial lithium loss. *Nat Energy* 2016;1:15008.
- [304] Xu Y, Zhu Y, Han F, Luo C, Wang C. 3D Si/C fiber paper electrodes fabricated using a combined electro spray/electrospinning technique for Li-ion batteries. *Adv Energy Mater* 2015;5:1400753.
- [305] Dash R, Pannala S. The potential of silicon anode based lithium ion batteries. *Mater Today* 2016;19:483–4.
- [306] Wang C, Wu H, Chen Z, McDowell MT, Cui Y, Bao Z. Self-healing chemistry enables the stable operation of silicon microparticle anodes for high-energy lithium-ion batteries. *Nat Chem* 2013;5:1042–8.
- [307] Li Y, Yan K, Lee H-W, Lu Z, Liu N, Cui Y. Growth of conformal graphene cages on micrometre-sized silicon particles as stable battery anodes. *Nat Energy* 2016;1:15029.
- [308] Lee JK, Oh C, Kim N, Hwang J-Y, Sun Y-K. Rational design of silicon-based composites for high-energy storage devices. *J Mater Chem A* 2016;4:5366–84.
- [309] Rosenman A, Markevich E, Salitra G, Aurbach D, Garsuch A, Chesneau FF. Review on Li-sulfur battery systems: an integral perspective. *Adv Energy Mater* 2015;5:1500212.

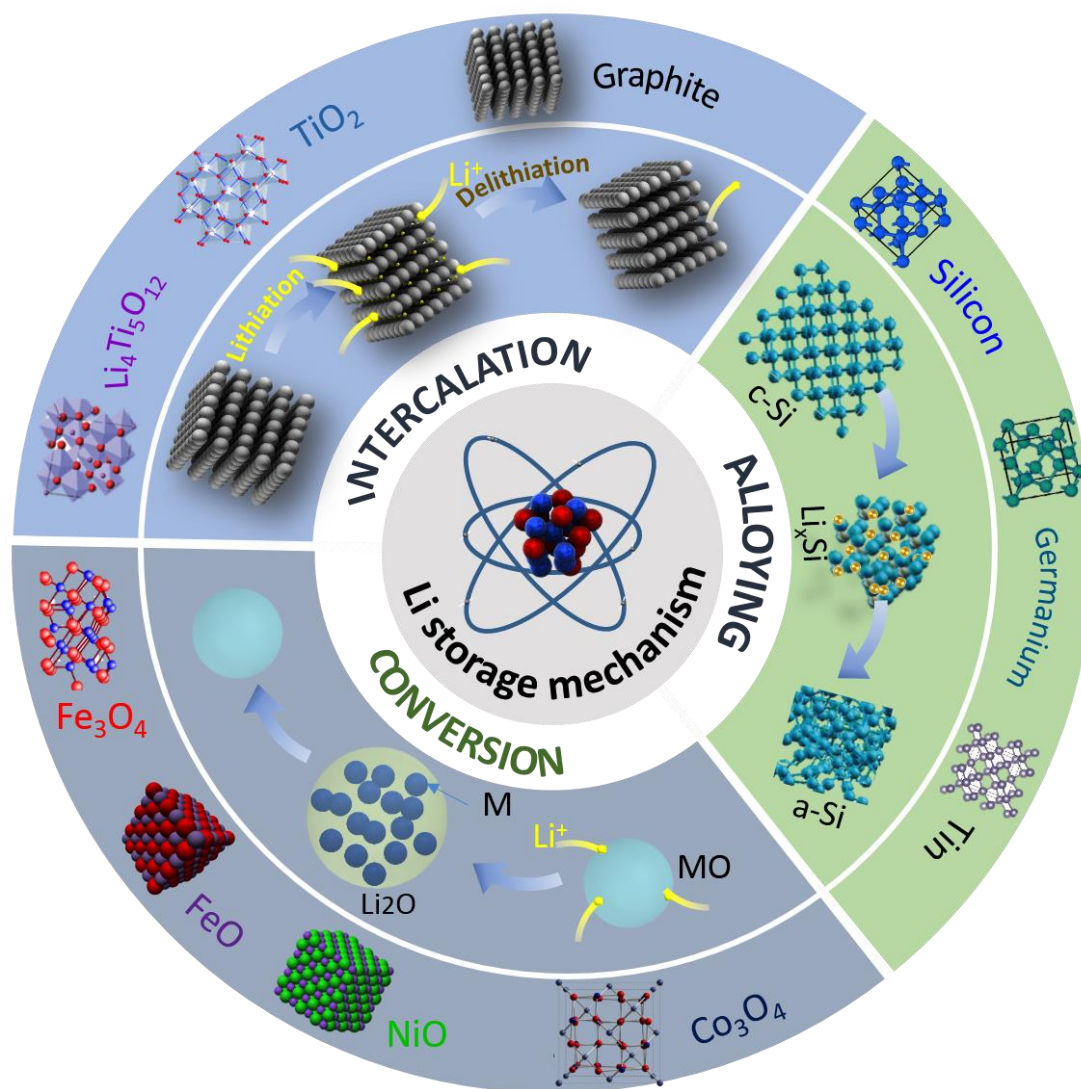


Fig. 1. Schematic illustration of different reaction mechanisms of anode materials for LIBs.

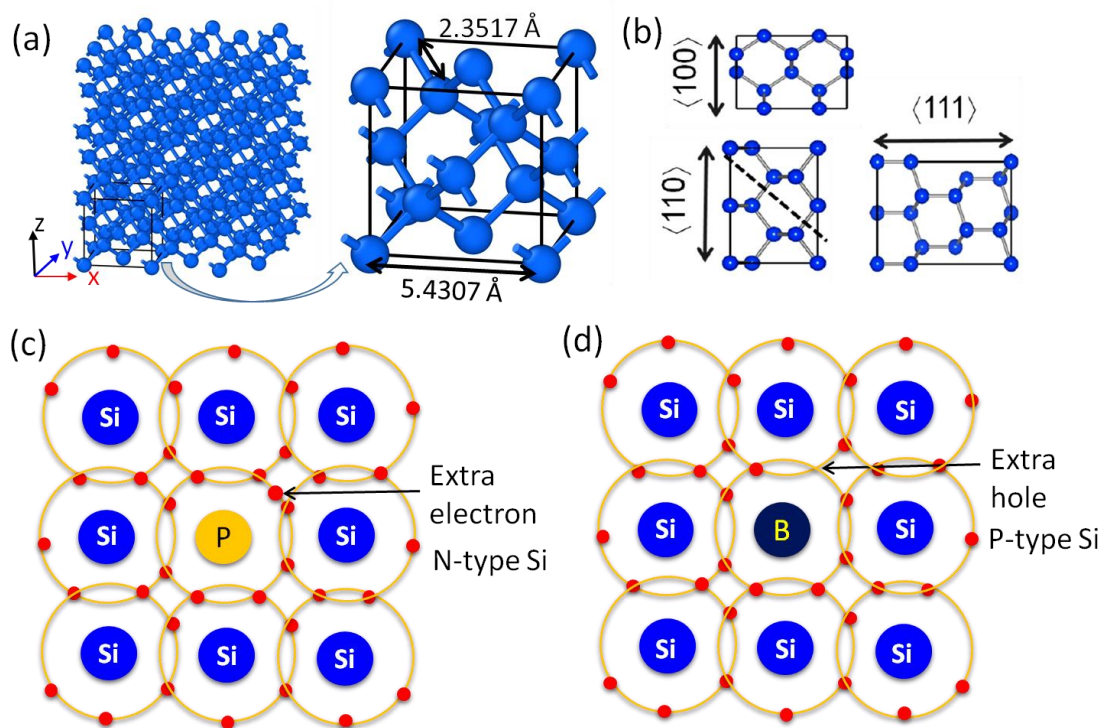


Fig. 2. (a) Crystal structure and dimensions of c-Si, (b) c-Si along the $\langle 100 \rangle$, $\langle 110 \rangle$ and $\langle 111 \rangle$ crystallographic orientations [11], atomistic configurations of (c) phosphorous-doped Si (N-type) with extra negative electrons, (d) boron-doped Si (P-type) with extra positive holes. (Reprinted with permission from [11], Copyright 2012 ACS).

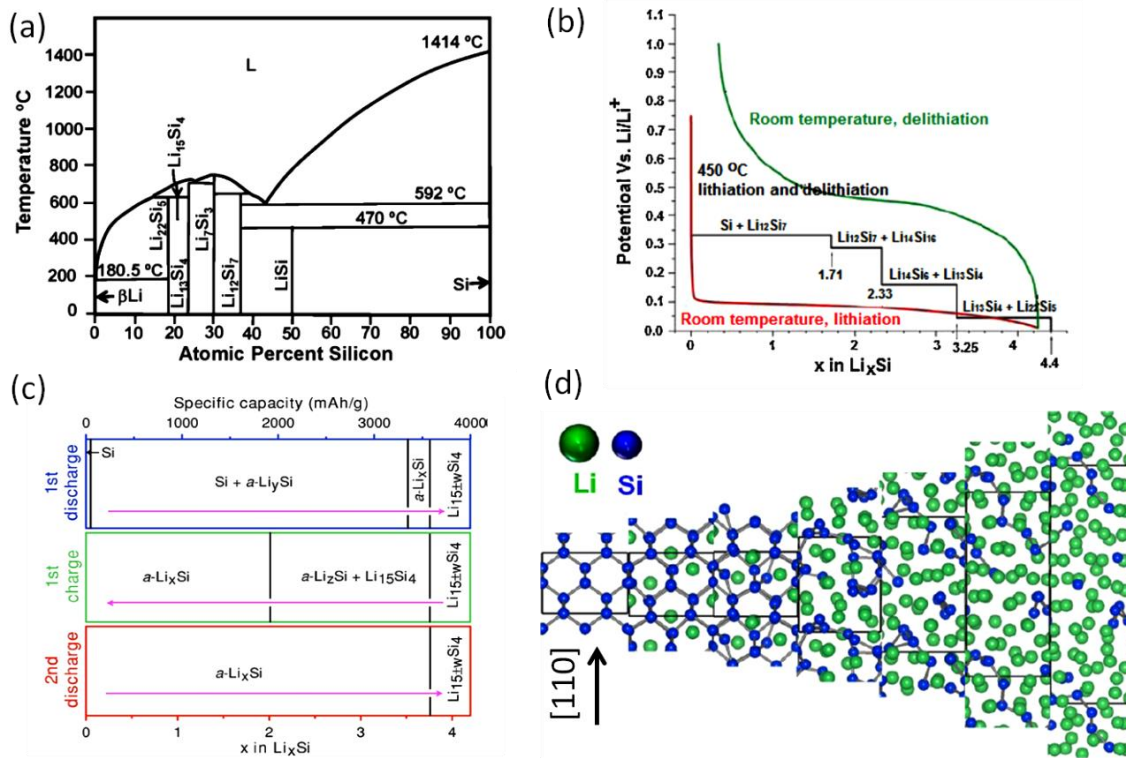


Fig. 3. (a) Si-Li phase diagram [13], (b) lithiation/delithiation curves of c-Si at room temperature (red and green) and high temperature (black) [15], (c) phases evolution obtained by *in-situ* XRD during charge/discharge cycles of a Li/Si battery between 0.05 and 0.9 V [19], (d) configurations from the lithiation algorithm for Si [110] model by first principles simulation [11]. (Reprinted with permission from [11,13,15,19], Copyright 2012 ACS, 1976, 2009 and 2012 Elsevier).

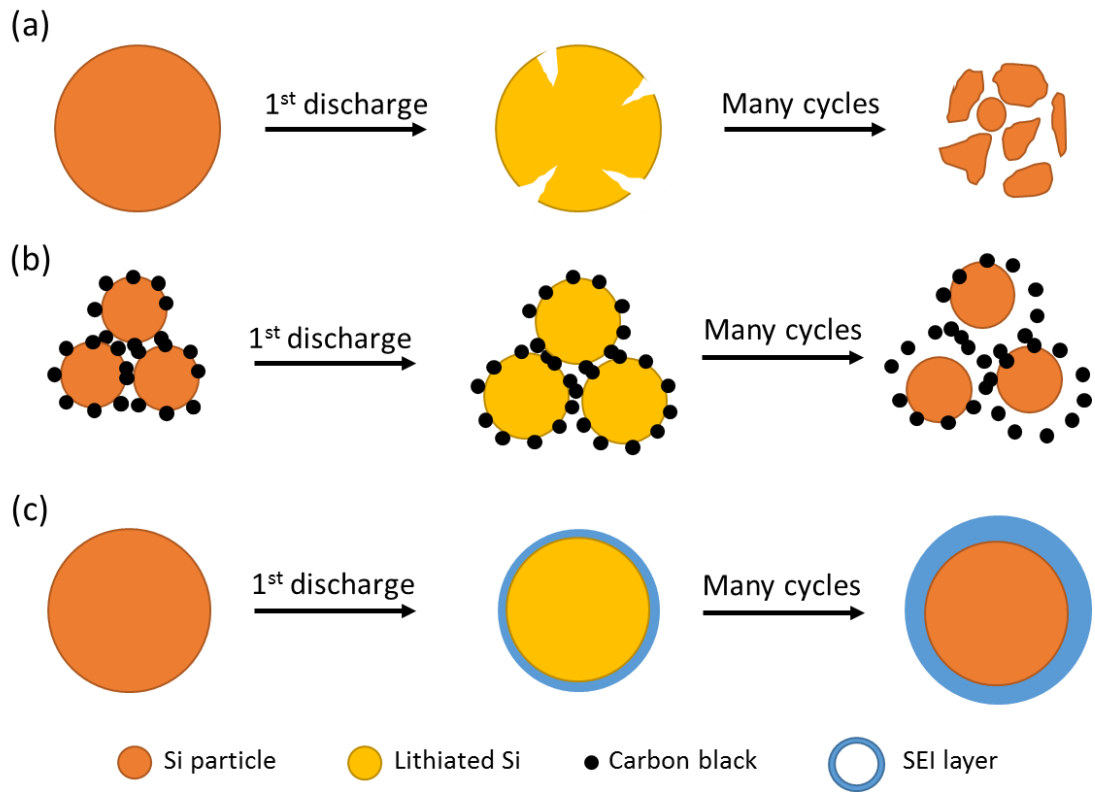


Fig. 4. Failure mechanisms of a Si electrode: (a) cracking and pulverization; (b) volume expansion and loss of electrical contacts and (c) formation of excessive SEI layer.

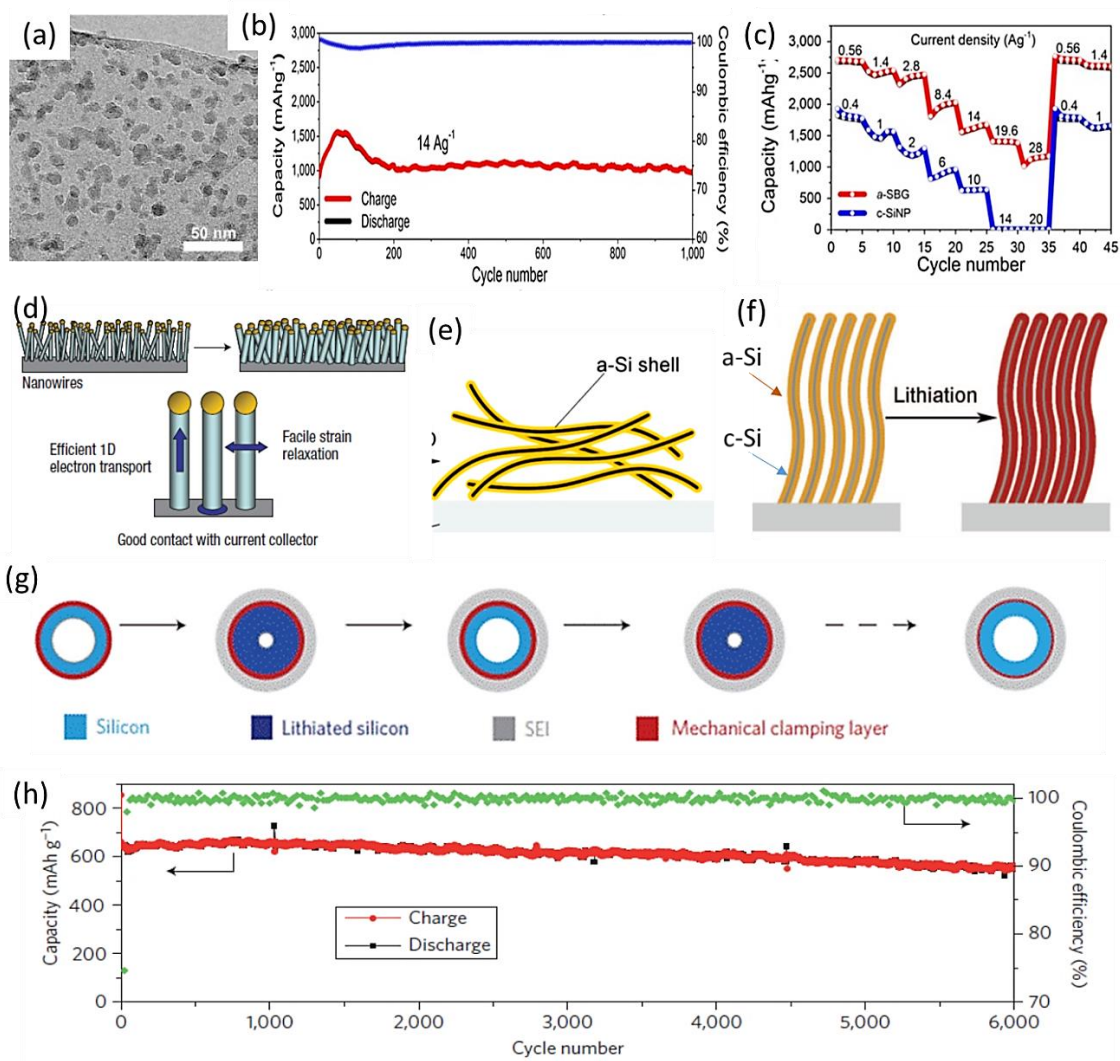


Fig. 5. (a) TEM image of a-Si NPs on graphene sheets (a-Si/G), (b) long term cyclic capacities and (c) rate capabilities of a-Si/G electrodes [67]; (d) Si NW electrode grown on stainless steel by CVD [69]; (e) CNF/a-Si core/shell NWs [70]; (f) c-Si/a-Si core/shell NW electrodes [71]; (g) schematic of a stable SEI layer on DWSiNTs and (h) exceptionally long cycle life of DWSiNT electrode [36]. (Reprinted with permission from [36,67,69–71] Copyright 2008, 2012 Nature, 2009, 2014 ACS).

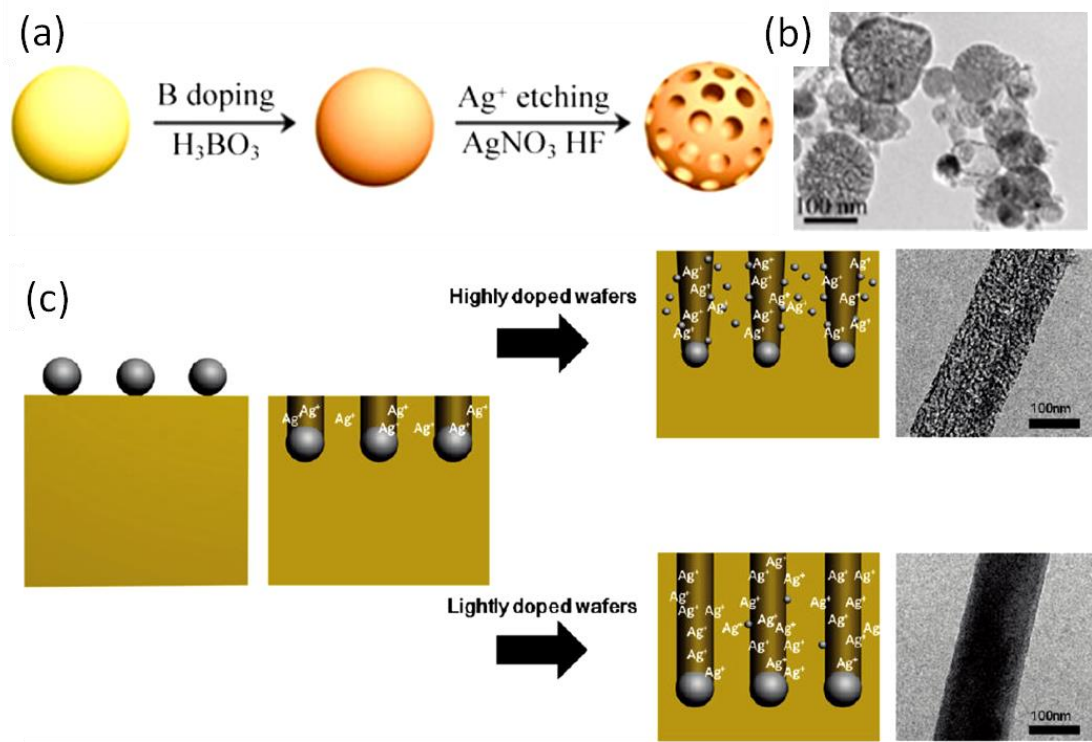


Fig. 6. (a) Synthesis procedure and (b) TEM image of porous Si NPs by MACE method [85]; (c) schematic and TEM images of formation mechanisms of porous Si NWs [86]. (Reprinted with permission from [85,86], Copyright 2013 Elsevier, 2011 ACS).

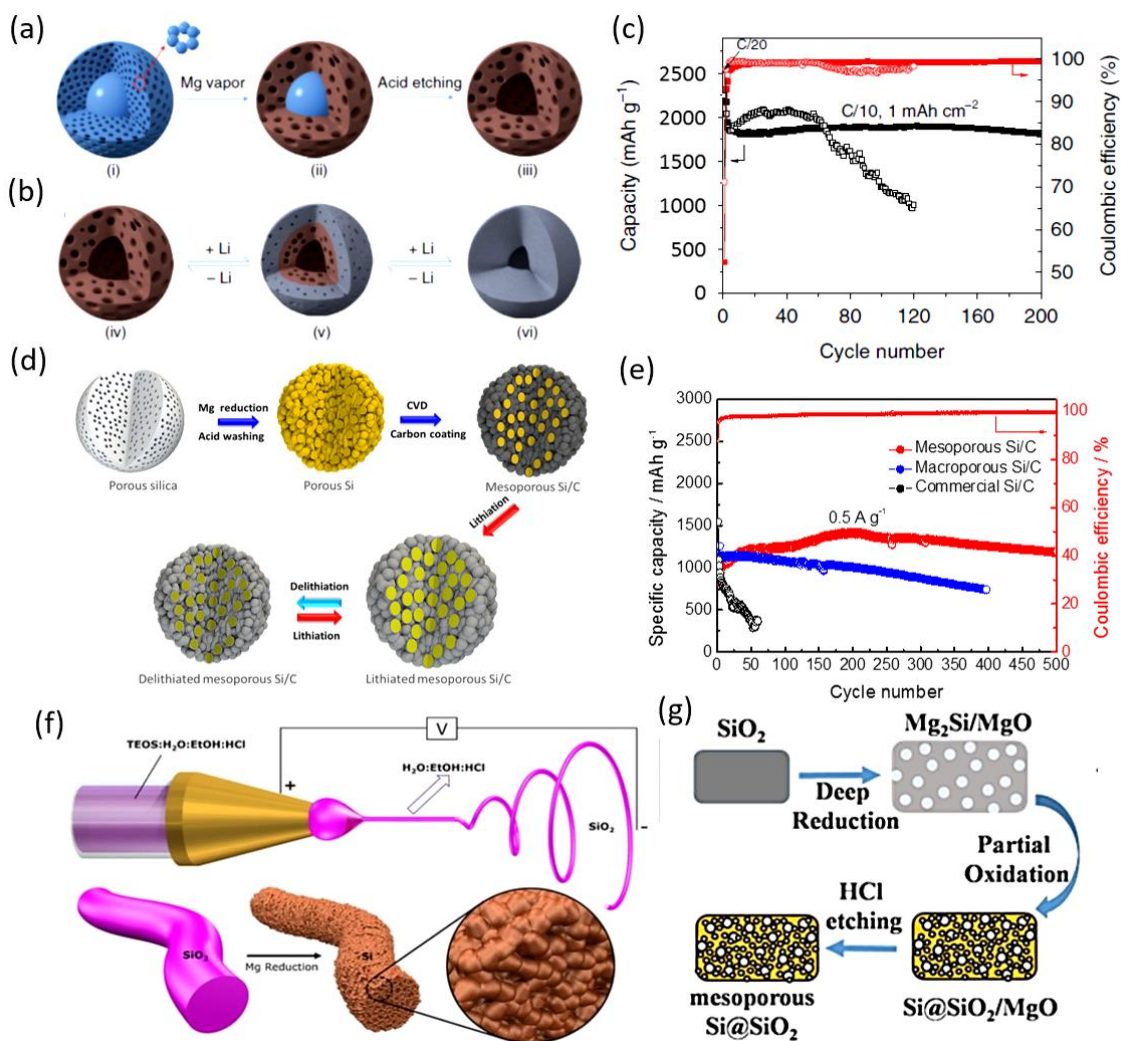


Fig. 7. Schematic of synthesis method (a), lithiation/delithiation processes (b) and electrochemical performance (c) of hierarchical porous Si NS electrodes [103]; (d) schematic of synthesis and lithiation/delithiation processes of mesoporous Si/C microspheres and (e) cyclic performance of mesoporous Si/C, macroporous Si/C and commercial Si/C electrodes [104]; (f) schematic of Si NF paper fabrication [108]; and (g) a deep reduction and partial oxidation strategy for fabricating mesoporous Si/SiO₂ with high conversion yield [116]. (Reprinted with permission from [103,104,108,116], Copyright 2015 Nature, 2016 RSC, 2016 ACS).

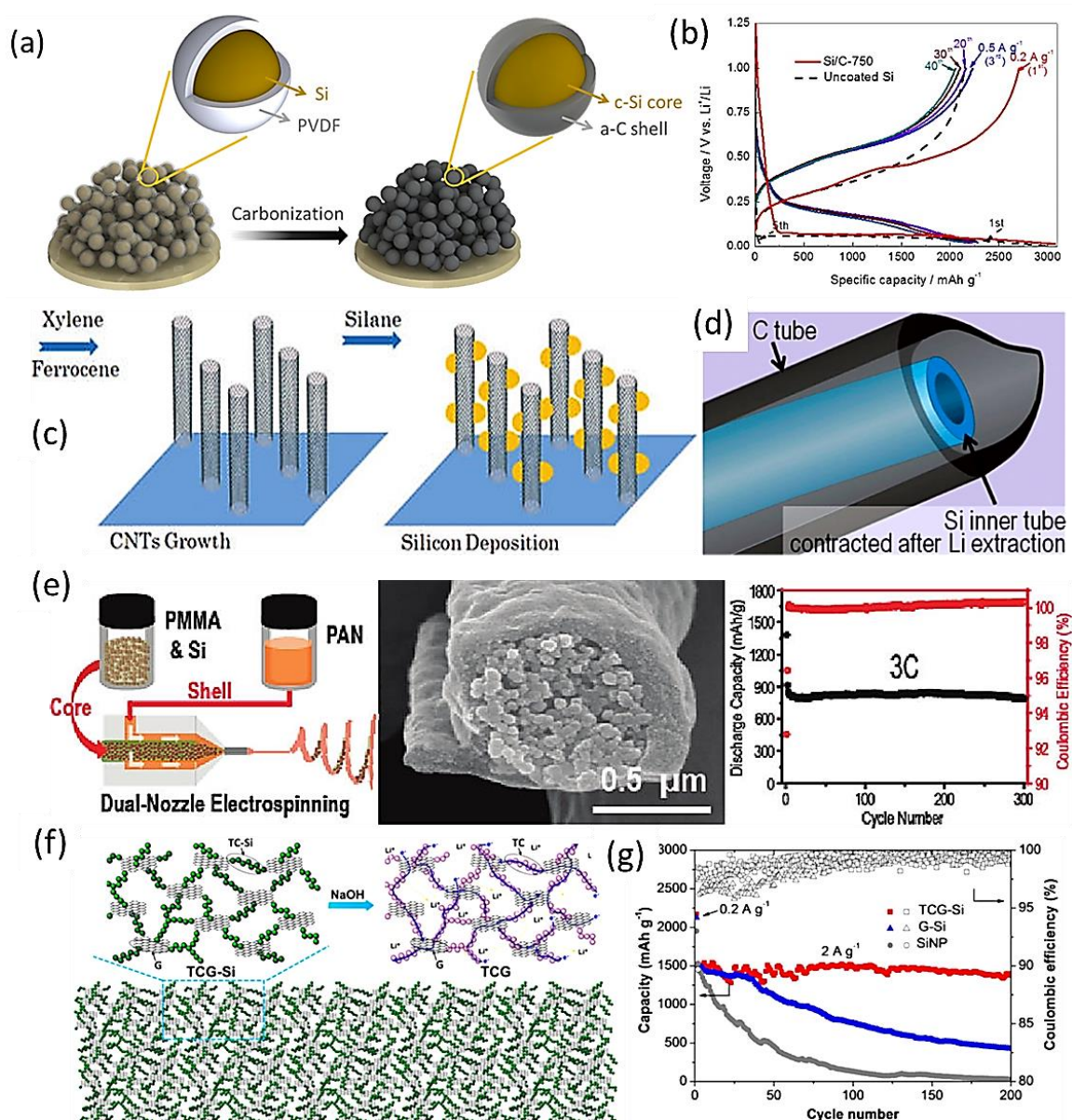


Fig. 8. (a) Schematic of fabrication and (b) electrochemical performance of Si/C electrodes [143]; (c) deposition of Si NPs on the surface of vertically aligned CNTs [149]; (d) schematic of a Si/CNT core/shell structure [150]; (e) fabrication process, morphology and electrochemical performance of electrospun core/shell Si/CNF composites [170]; (f) schematic of fabrication and (g) cyclic stability of Si NPs-impregnated assemblies of templated carbon bridged oriented graphene (TCG-Si) electrodes [187]. (Reprinted with permission from [143,149,150,170,187], Copyright 2016 Elsevier, 2010, 2012 and 2015 ACS).

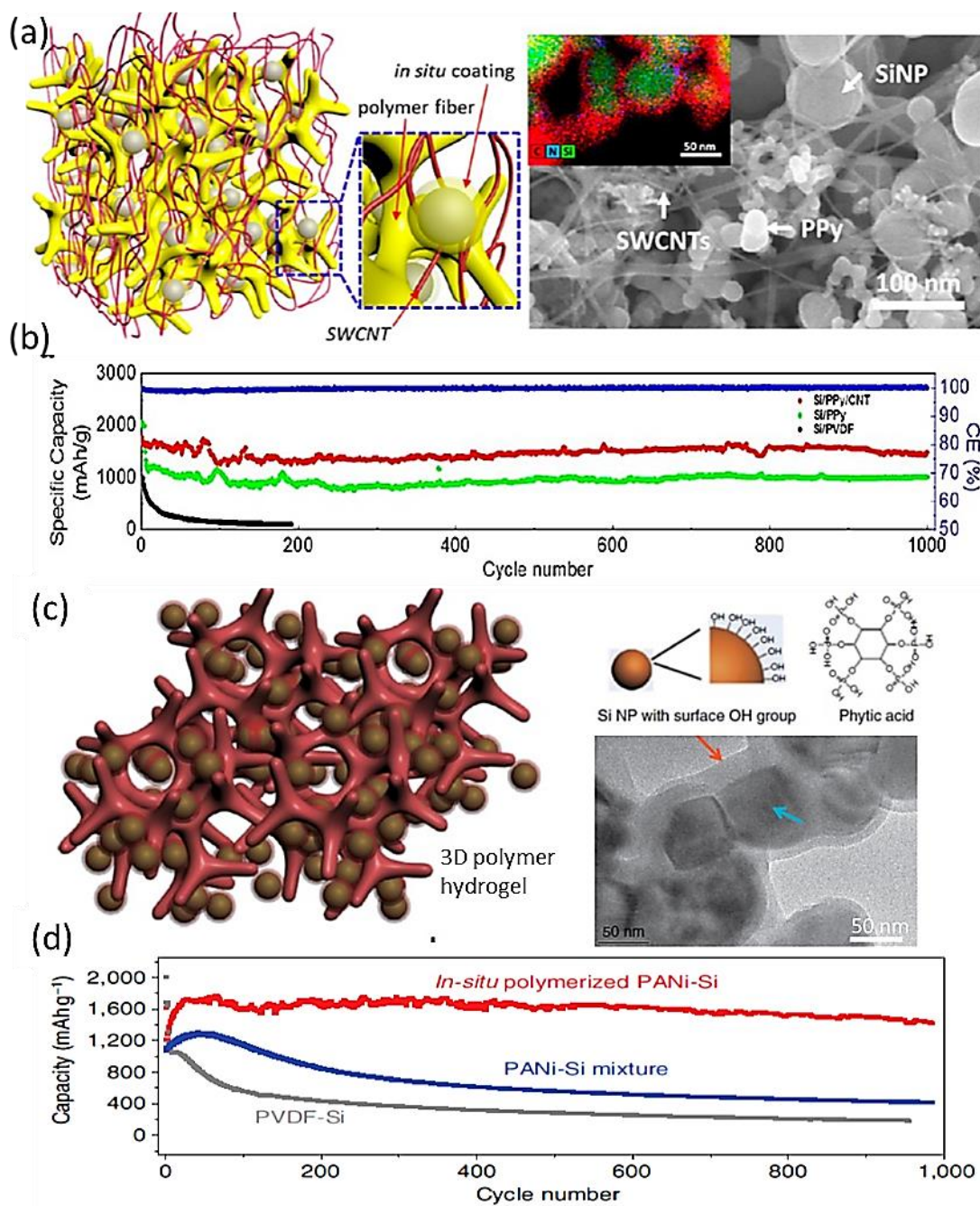


Fig. 9. (a) Schematic and SEM images of ternary Si NPs/PPy/CNT electrodes and (b) cyclic performance of Si/PPy/CNT, Si/PPy and Si/PVDF electrodes [192]; (c) schematic and morphologies of 3D porous Si-PANI electrodes and (d) cyclic performance of *in-situ* polymerized PANi-Si, PANi-Si mixture and PVDF-Si electrodes [193]. (Reprinted with permission from [192,193], Copyright 2013 Nature, 2013 ACS).

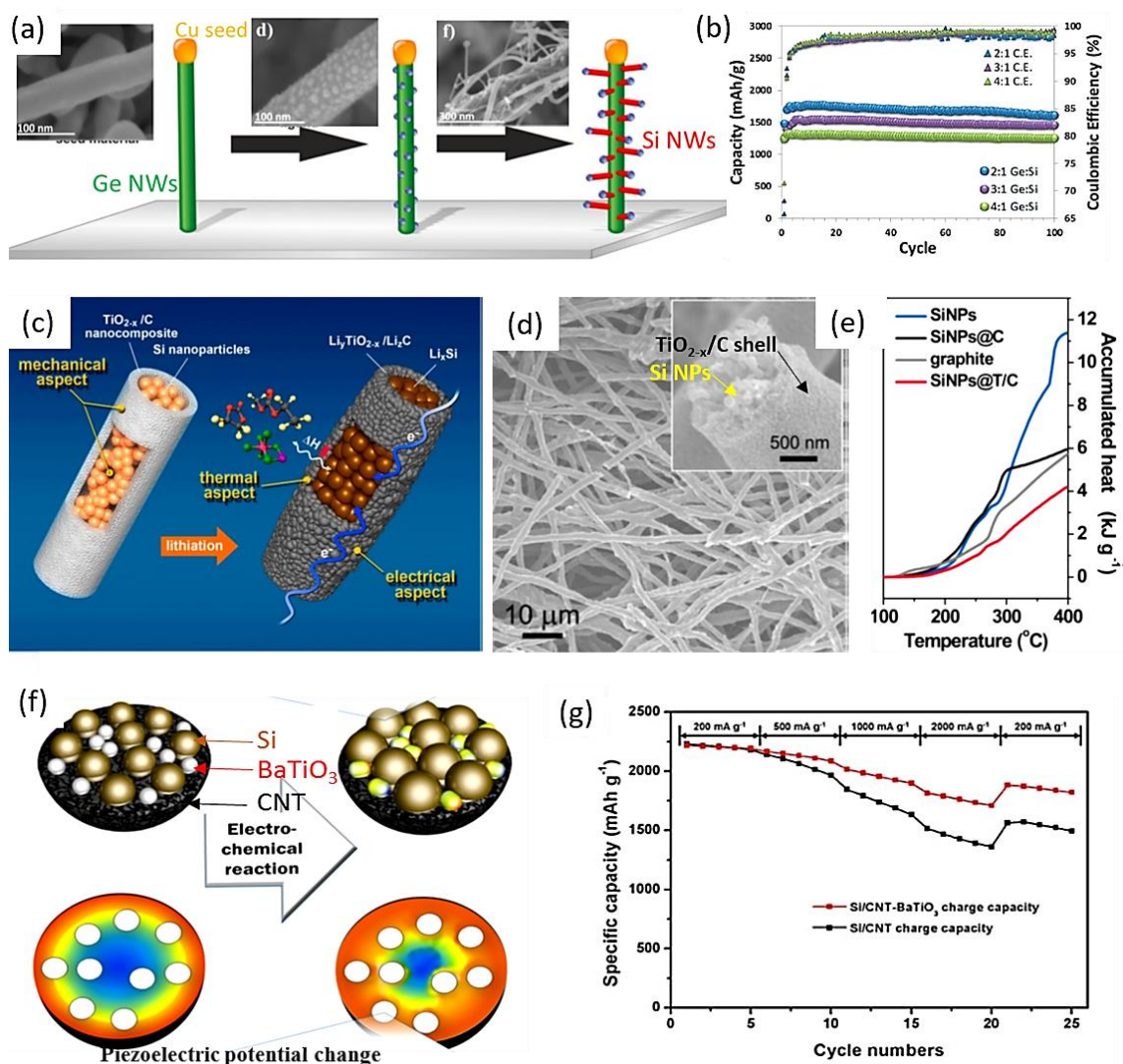


Fig. 10. (a) Schematic illustration of the fabrication process and the corresponding morphologies of Si-Ge branched NW heterostructure, (b) discharge capacities and Coulombic efficiencies of Si-Ge electrodes [207]; (c-d) schematic and morphologies of electrospun Si/TiO_{2-x}@C core/shell structure, (e) accumulated heat curves of various Si composites and graphite [209]; (f) schematic illustration of microstructures and local piezoelectric potential changes of Si/BaTiO₃/CNT composite, (g) rate capabilities of Si/BaTiO₃/CNT (red) and Si/CNT (black) electrodes [210]. (Reprinted with permission from [207,209,210], Copyright 2013, 2015 and 2016 ACS).

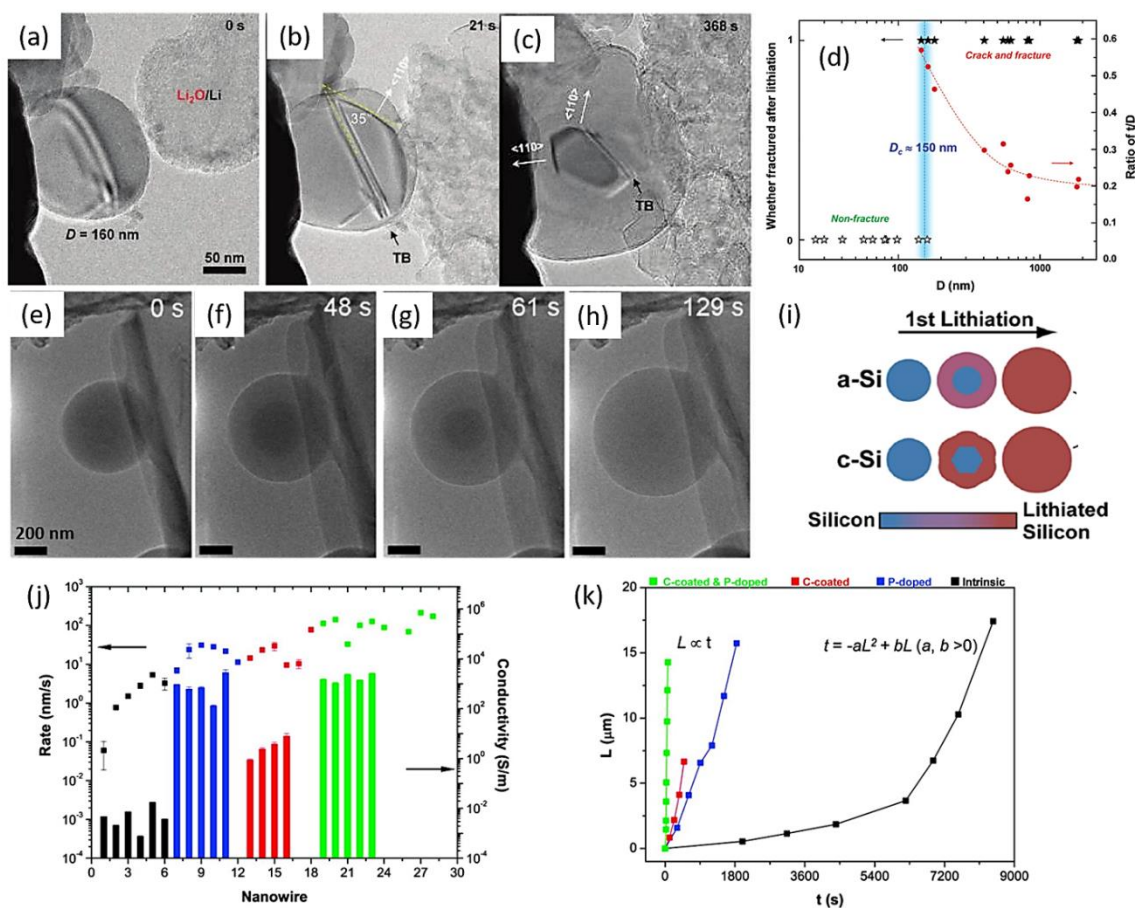


Fig. 11. (a-c) Time sequential *in-situ* TEM images of lithiation of an individual c-Si particle, (d) statistics of fracture showing the critical size of ~150 nm [226]; (e-h) time resolved *in-situ* TEM images of lithiation of an a-Si particle; (i) schematics of initial lithiation processes in a-Si and c-Si particles [228]; (j-k) lithiation speeds and conductivities of intrinsic (black), c-coated (red), P-doped (blue) and C-coated P-doped Si NWs (green) [235]. (Reprinted with permission from [226,228,235], Copyright 2011, 2012, 2013 ACS).

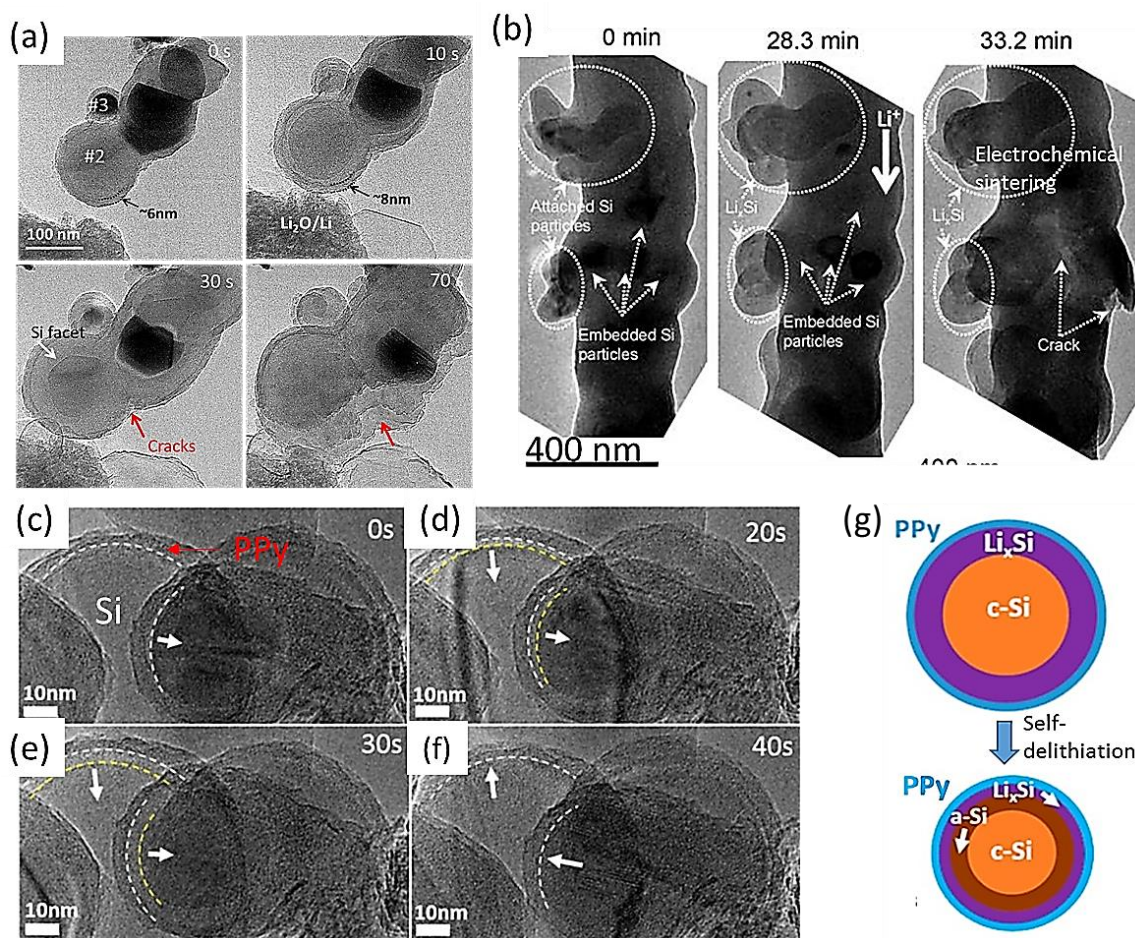


Fig. 12. (a) Structural evolution of Si/C NPs during the initial lithiation [143]; (b) lithiation characteristics of Si/CNF electrode under *in-situ* TEM [238]; (c-f) time resolved TEM images depicting the “fluctuation” of PPy coated Si NPs during lithiation; (g) schematic illustration of “self-discharge” process [244]. (Reprinted with permission from [143,238,244], Copyright 2016 Elsevier, 2012, 2015 ACS).

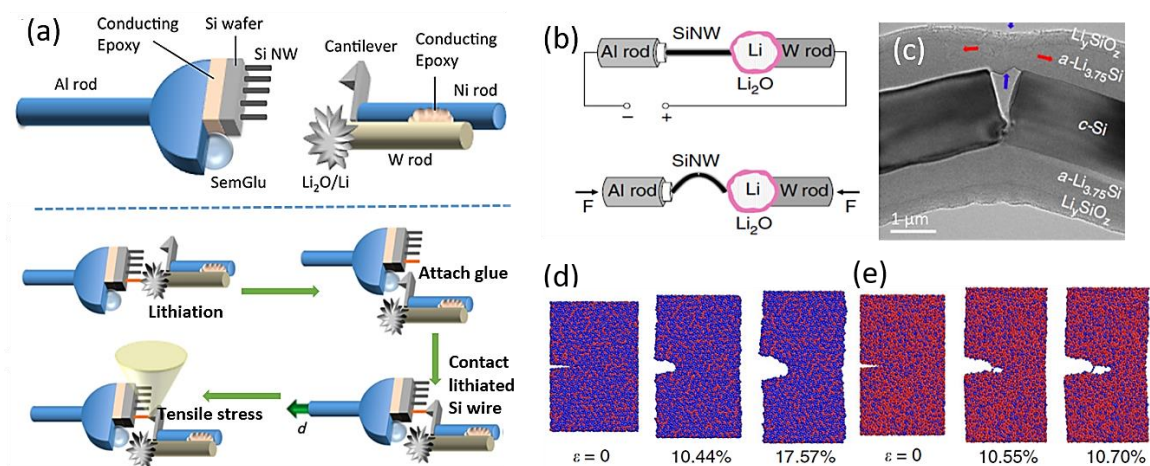


Fig. 13. (a) Schematic illustration of a tensile test setup within *in-situ* TEM (up image); experimental procedure of lithiation and *in-situ* tension of a Si NW (down image) [245]. (b) Schematic illustration of *in-situ* electrochemical and bending test of a Si NW; (c) TEM image showing the fracture of c-Si core and plastic deformation of lithiated Si shell; molecular dynamics simulation snapshots showing (d) the ductile response of Li-rich Si (a-Li_{2.5}Si) and (e) the brittle fracture of Li-lean Si (a-Li_{0.5}Si) [254]. (Reprinted with permission from [245, 254], Copyright 2012 ACS and 2015 Nature).

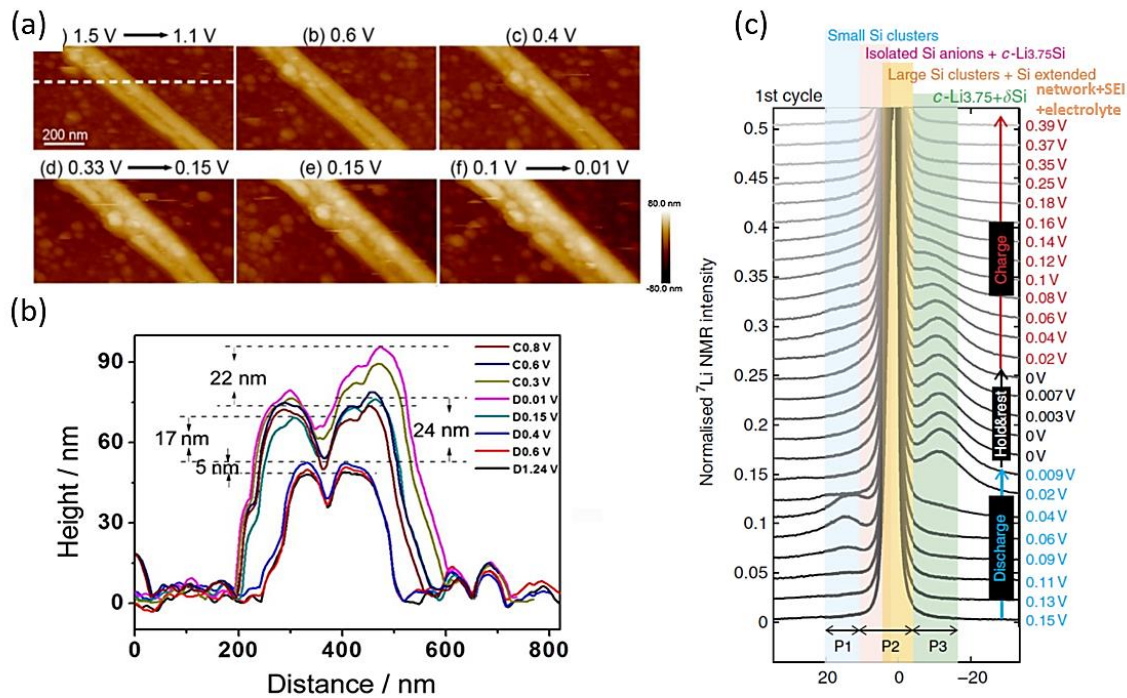


Fig. 14. (a) *In-situ* AFM height images of a single Si NW electrode during initial lithiation; (b) cross-sectional analysis of the height of the location marked by a dashed line in (a) [256]; (c) stacked *in-situ* ^7Li NMR spectra of Si NW electrodes obtained during the first discharge/charge cycle and enlarged to show the weaker, broader peaks [269]. (Reprinted with permission from [256, 269], Copyright 2014 ACS, 2014 Nature).

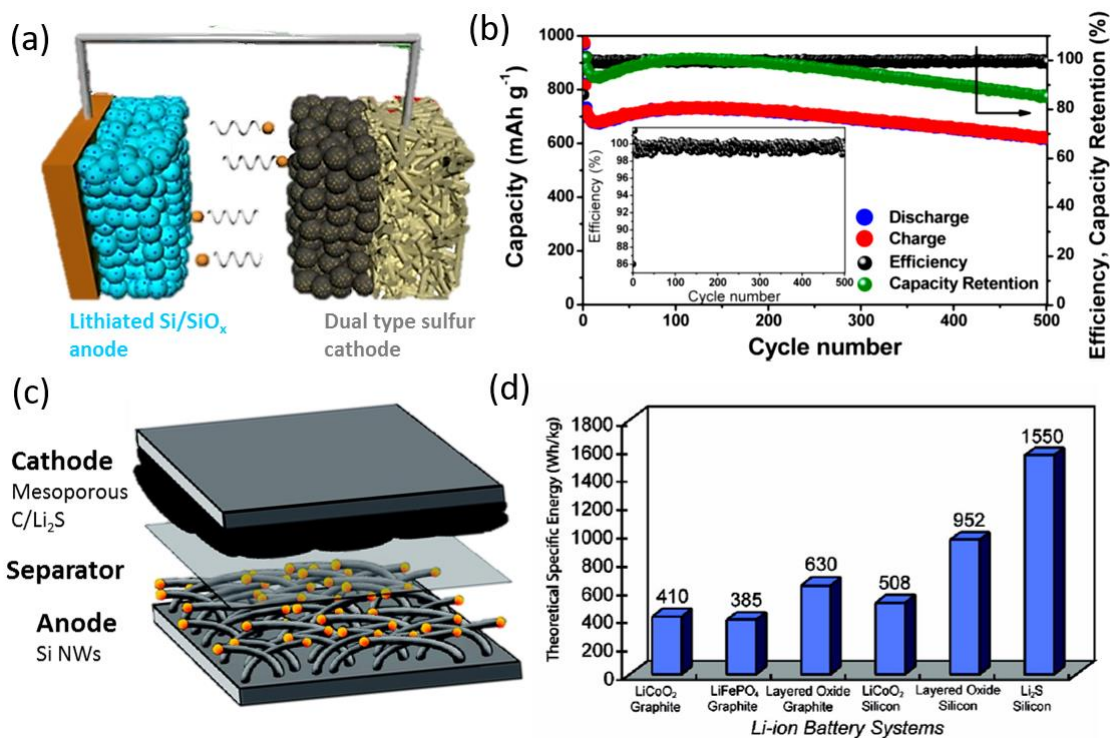


Fig. 15. (a) Schematic illustration and (b) cyclic performance at 1 C of the full cell consisting of a lithiated Si/SiO_x anode and a dual-type sulfur cathode [277]; (c) schematic of the full battery comprising a mesoporous C/Li₂S cathode and a Si NW anode; (d) comparison of theoretical specific capacities for different types of LIBs [281]. (Reprinted with permission from [277,281], Copyright 2010, 2015 ACS).

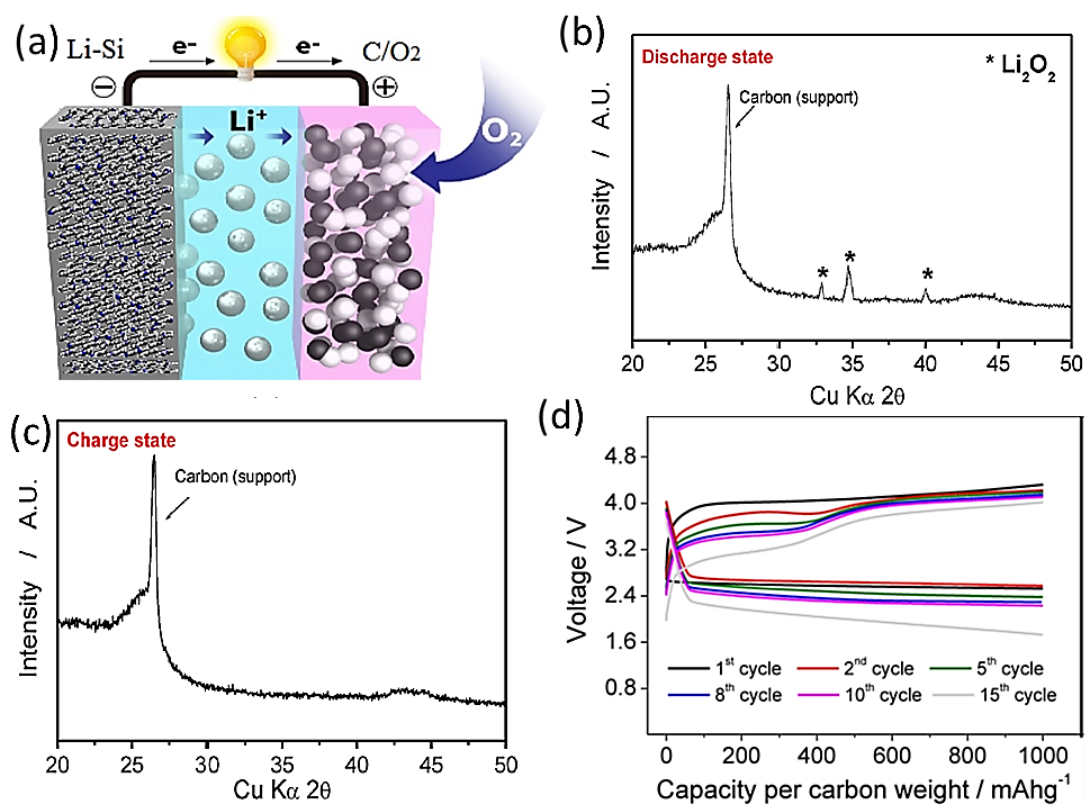


Fig. 16. (a) Schematic illustration of $\text{Li}_x\text{Si-O}_2$ full cell; XRD patterns of carbon oxygen cathode after full discharge (b) and charge (c); and (d) voltage profiles of $\text{Li}_x\text{Si-O}_2$ cell at 0.2 A g^{-1} for 15 cycles [284]. (Reprinted with permission from [284], Copyright 2012 ACS).

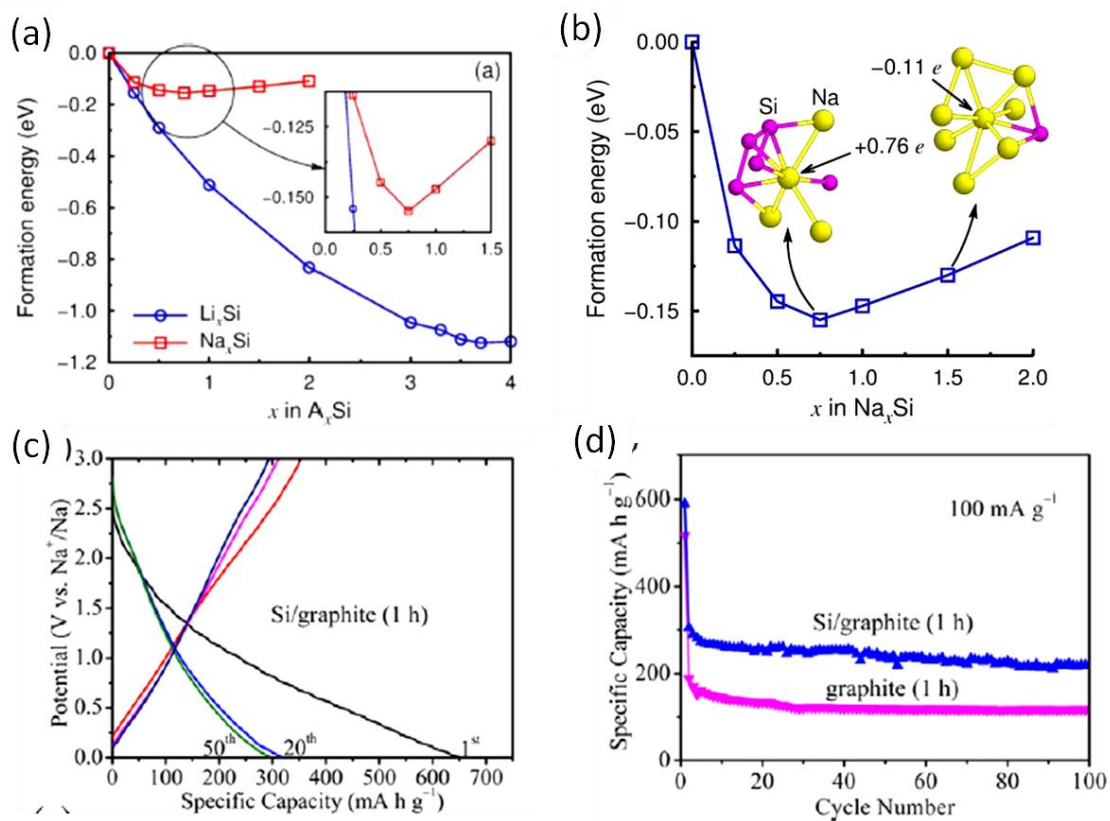


Fig. 17. (a) Formation energies of A_xSi (where $A = Li$ and Na) and (b) two representative structures of Na_xSi formed at different energies [291], (c) charge/discharge profiles and (d) cyclic capacities of Si/graphite anodes at $100 mA g^{-1}$ for SIB [294]. (Reprinted with permission from [291,294], Copyright 2014 ACS, 2016 Elsevier).

Table 1 Comparison of reaction mechanisms, densities, lithiation/delithiation processes, theoretical specific capacities (Scapacities), volume changes (ΔV) and potentials of various representative anode materials.

Reaction mechanisms	Anode materials	Density /g cm ⁻³	Lithiation/delithiation processes	Scapacity / mAh g ⁻¹	ΔV / %	Potential vs Li/Li ⁺ / V
Insertion	C	2.25	6C + Li \leftrightarrow LiC ₆	372	12	0.05
	Li ₄ Ti ₅ O ₁₂	3.5	LTO + 3Li \leftrightarrow Li ₇ Ti ₅ O ₁₂	175	1	1.6
Conversion	Fe ₃ O ₄	5.17	Fe ₃ O ₄ +8Li \leftrightarrow 3Fe + 4Li ₂ O	924	93	~0.8
	FeO	5.74	FeO + 2Li \leftrightarrow Fe + Li ₂ O	744	~90	~1.0
	Co ₃ O ₄	5.18	Co ₃ O ₄ +8Li \leftrightarrow 3Co + 4Li ₂ O	890	~100	~1.1
	NiO	6.67	NiO + 2Li \leftrightarrow Ni + Li ₂ O	718	~100	~0.6
Alloying	Si	2.33	Si + 4.4 Li \leftrightarrow Li _{4.4} Si	4200	~300	0.4
	Sn	7.29	Sn + 4.4 Li \leftrightarrow Li _{4.4} Sn	994	260	0.6
	Ge	5.32	Ge + 4.4 Li \leftrightarrow Li _{4.4} Ge	1600	370	0.4

Table 2 Crystal structure, space group, unit cell volume of Li-Si compounds.

Compound and crystal structure	Space group	Unit cell volume /Å ³	Volume per Si atom /Å ³
Si, cubic	Fd $\bar{3}$ m	160.2	20.0
Li ₁₂ Si ₇ , orthorhombic	Pnma	243.6	58.0
Li ₁₄ Si ₆ , orthorhombic	R $\bar{3}$ m	308.9	51.5
Li ₁₃ Si ₄ , orthorhombic	Pbam	538.4	67.3
Li ₂₂ Si ₅ , cubic	F23	659.2	82.4

Table 3 Comparison of processes, morphologies, production costs and advantages/disadvantages between different fabrication methods of nanosilicon. (Reprinted with permission from [38,86], Copyright 2013 Elsevier, 2011 ACS).

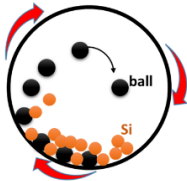
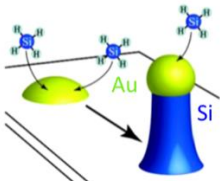
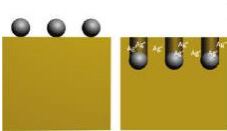
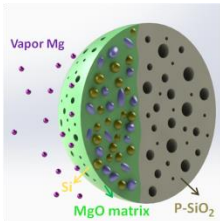
Methods	Process	Morphologies	Production; costs of raw materials	Advantages/disadvantages
BM [60,61]		Particle	~4 kg h ⁻¹ ; ~\$ 1 kg ⁻¹ of M-Si ~\$ 0.6 kg ⁻¹ of F-Si	High yield, scalable, cheap/ large particles
CVD [35,38,39,47]		Particle, NW/NT and thin film	0.75 mg h ⁻¹ ; ~\$ 100 kg ⁻¹ of SiH ₄	Controllable, diverse /expensive, low yield, dangerous
MACE [81–83,86]		Porous particle, NW, and 3D structure	0.1-10 g h ⁻¹ ; ~\$ 200 of P-Si (2" × 0.5mm wafer), M-Si	Controllable, diverse, scalable, simple/toxic
MR [65,93,94]		Particle, NW, NT, NF, and 3D structure	100-500 mg h ⁻¹ ; ~\$ 2 Kg ⁻¹ of Mg	Controllable, scalable, diverse, cheap, simple/ low efficiency

Table 4 Structures and electrochemical properties of representative nanosilicon anodes in LIBs prepared by four major methods (*CE= Coulombic efficiency).

Method	Structures	Electrochemical properties		Ref.	
		1 st cycle	Cyclic capacity		
BM	a-Si/SiO _x /C	1980 mAh g ⁻¹ with 77% CE*	1230 mAh g ⁻¹ after 100 cycles at 0.5 Ag ⁻¹	[59]	
	Si NPs	2500 mAh g ⁻¹ with 81 % CE	1600 mAh g ⁻¹ after 600 cycles at 0.48A/g	[60]	
	F-Si	2198 mAh g ⁻¹ with 72 % CE	1360 mAh g ⁻¹ after 100 cycles at 0.4 A/g	[61]	
CVD	Si/C granule	1950 mAh g ⁻¹ with 85% CE	~1500 mAh g ⁻¹ after 100 cycles at 1C	[66]	
	a-Si/G	2858 mAh g ⁻¹	1103 mAh g ⁻¹ after 1000 cycles at 14 A/g	[67]	
	Hollow Si NPs	2725 mAh g ⁻¹ with 77 % CE	1420 mAh g ⁻¹ after 700 cycles at 0.5 C	[64]	
	Hollow Si NPs	2367 mAh g ⁻¹ with 73 % CE	1650 mAh g ⁻¹ after 100 cycles at 0.1 Ag ⁻¹	[68]	
	Si NWs	3214 mAh g ⁻¹ with 73 % CE	~3500 mAh g ⁻¹ after 20 cycles at C/20	[69]	
	CNF/Si NWs	~2000 mAh g ⁻¹ with 90% CE	1600 mAh g ⁻¹ after 55 cycles at 2.5 Ag ⁻¹	[70]	
	Si NWs	1060 mAh g ⁻¹ with 85 % CE	1000 mAh g ⁻¹ after 100 cycles at 0.84 A/g	[71]	
	Si NTs	3247 mAh g ⁻¹ with 89% CE	~3000 mAh g ⁻¹ after 80 cycles at 3Ag ⁻¹	[72]	
	DWSiNTs	~640 mAh g ⁻¹ with 76 % CE	~570 mAh g ⁻¹ after 6000 cycles at 12C	[36]	
	C/Si/C NTs	2545 mAh g ⁻¹ with 61% CE	2200 mAh g ⁻¹ after 60 cycles at 0.18A/g	[74]	
	Hollow Si NTs	1970 mAh g ⁻¹ with 75% CE	~1000 mAh g ⁻¹ after 400 cycles at 2Ag ⁻¹	[75]	
	MACE	Porous Si NPs	~900 mAh g ⁻¹ with 75 % CE	1000 mAh/g after 100 cycles at 0.42 A/g	[84]
		Porous Si NPs	~2500 mAh g ⁻¹	1400 mAh g ⁻¹ after 200 cycles at 1A g ⁻¹	[85]
Porous Si NWs		3038 mAh g ⁻¹ with 90 % CE	2000 mAh g ⁻¹ after 250 cycles at 2A g ⁻¹	[87]	
Porous Si NWs		~2000 mAh g ⁻¹ with ~50% CE	2111 mAh g ⁻¹ after 50 cycles at 0.84 A/g	[88]	
Bulk 3D Si		2410 mAh g ⁻¹ with 91 % CE	2289 mAh g ⁻¹ after 70 cycles at 0.8 A g ⁻¹	[90]	
Porous bulk Si		2390 mAh g ⁻¹ with 94 % CE	2079 mAh g ⁻¹ after 50 cycles at 0.2 A g ⁻¹	[91]	
Si sponge		~750 mAh g ⁻¹ with 56 % CE	640 mAh g ⁻¹ after 1000 cycles at 1A g ⁻¹	[92]	
MR	Si sphere	1810 mAh g ⁻¹ with 80 % CE	550 mAh g ⁻¹ after 50 cycles at 0.1 A g ⁻¹	[95]	
	Ag/hollow Si NS	3146 mAh g ⁻¹ with 84 % CE	2925 mAh g ⁻¹ after 100 cycles at 0.5 Ag ⁻¹	[98]	
	PPy/hollow Si NS	1772 mAh g ⁻¹ with 68 % CE	~2000 mAh g ⁻¹ after 250 cycles at 1A g ⁻¹	[99]	
	Hollow Si NS	1850 mAh g ⁻¹ with 52 % CE	1800 mAh g ⁻¹ after 200 cycles at 0.36 A/g	[103]	
	Porous Si/C NS	1500 mAh g ⁻¹ with 87 % CE	990 mAh g ⁻¹ after 1000 cycles at 1A g ⁻¹	[104]	
	Si NFs	2846 mAh g ⁻¹ with 74 % CE	1214 mAh g ⁻¹ after 100 cycles at 2A g ⁻¹	[107]	
	Si NFs	2050 mAh g ⁻¹ with ~73 % CE	802 mAh g ⁻¹ after 659 cycles at 0.4 A g ⁻¹	[108]	
	Sand-based Si	3000 mAh g ⁻¹ with ~94 % CE	1024 mAh g ⁻¹ after 1000 cycles at 2A g ⁻¹	[110]	
	Rice husk-based Si	1615 mAh g ⁻¹ with 84 % CE	1554 mAh g ⁻¹ after 200 cycles at 2A g ⁻¹	[113]	
	Leave-based Si	2590 mAh g ⁻¹ with 87 % CE	1800 mAh g ⁻¹ after 100 cycles at 0.84 A/g	[114]	
	Reed leave-based Si	2435 mAh g ⁻¹ with 61 % CE	420 mAh g ⁻¹ after 4000 cycles at 10 C	[115]	
	Porous Si/SiO ₂	1782 mAh g ⁻¹ with 64 % CE	873 mAh g ⁻¹ after 1400 cycles at 1.8 A g ⁻¹	[116]	

Table 5 Structures, Si contents and electrochemical characteristics of representative nanostructured Si/C composite electrodes.

Sample	Structures, Si content	Electrochemical performance		Ref.
		1 st cycle	Cyclic capacities	
Si/C	Core/shell, 81 wt%	~1500 mAh g ⁻¹ with 65 % CE	~1800 mAh g ⁻¹ after 50 cycles at 0.1 A g ⁻¹	[137]
	Core/shell, 80 wt%	2734 mAh g ⁻¹ with 75 % CE	988 mAh g ⁻¹ after 100 cycles at 0.1 A g ⁻¹	[139]
	Core/shell, 87 wt%	1955 mAh g ⁻¹ with 78 % CE	1150 mAh g ⁻¹ after 500 cycles at 1.2 A g ⁻¹	[140]
	Porous C, 76 wt%	1461 mAh g ⁻¹ with 54 % CE	1018 mAh g ⁻¹ after 100 cycles at 0.5 A g ⁻¹	[144]
	Porous Si, 32 wt%	1375 mAh g ⁻¹ with 83 % CE	1053mAhg ⁻¹ after 100 cycles at 0.05A g ⁻¹	[145]
	Yolk/shell, 71 wt%	2833 mAh g ⁻¹ with 60 % CE	~2000 mAh g ⁻¹ after 50 cycles at 0.4 A g ⁻¹	[147]
Si/CNT	External Si, /	2049 mAh g ⁻¹ with 80 % CE	~2000 mAh g ⁻¹ after 25 cycles at 0.1 A g ⁻¹	[149]
	External Si, /	1954 mAh g ⁻¹	1260 mAh g ⁻¹ after 230 cycles at 0.23 C	[153]
	External Si, 60wt%	3127 mAh g ⁻¹ with 61 % CE	2912 mAh g ⁻¹ after 100 cycles at 0.2 C	[154]
	Internal Si, 33 wt%	2100 mAh g ⁻¹ with 75 % CE	~800 mAh g ⁻¹ after 100 cycles at 1.7 A g ⁻¹	[150]
	Internal Si, 22 wt%	1671 mAh g ⁻¹ with ~60 % CE	1475 mAh g ⁻¹ after 20 cycles at 0.1 A g ⁻¹	[151]
Si/CNF	Solid, 26 wt%	1550 mAh g ⁻¹ with 81 % CE	726 mAh g ⁻¹ after 40 cycles at 0.05 A g ⁻¹	[161]
	Solid, 26 wt%	962 mAh g ⁻¹ with 77 % CE	644 mAh g ⁻¹ after 50 cycles at 0.05 A g ⁻¹	[162]
	Solid, 30 wt%	~2000 mAh g ⁻¹ with 85 % CE	~900 mAh g ⁻¹ after 30 cycles at 0.05 A g ⁻¹	[163]
	Core/shell, 22 wt%	997 mAh g ⁻¹ with 65 % CE	603 mAh g ⁻¹ after 300 cycles at 0.5 A g ⁻¹	[166]
	Porous, 47 wt%	969 mAh g ⁻¹ with 71 % CE	872 mAh g ⁻¹ after 200 cycles at 1 A g ⁻¹	[169]
	Core/shell, 50 wt%	1305 mAh g ⁻¹ with 87 % CE	750 mAh g ⁻¹ after 300 cycles at 2.75 A g ⁻¹	[170]
	Porous, 50 wt%	1598 mAh g ⁻¹ with 60 % CE	1104 mAh g ⁻¹ after 100 cycle at 0.5 A g ⁻¹	[171]
	Multishell, 38 wt%	1883 mAh g ⁻¹ with 78 % CE	904 mAh g ⁻¹ after 100 cycles at 0.05 A g ⁻¹	[172]
Si/G	Paper, 60 wt%	~1900 mAh g with ~65 % CE	~900 mAh g ⁻¹ after 120 cycles at 1 A g ⁻¹	[174]
	Paper, 80 wt%	1866 mAh g ⁻¹ with 60 % CE	1153 mAh g ⁻¹ after 100 cycles at 0.2 A g ⁻¹	[175]
	Foam, 67 wt%	~2750 mAh g with 68 % CE	2050 mAh g after 200 cycles at 0.2 A g	[183]
	Sheets, 36 wt%	~1000 mAh g ⁻¹ with 85 % CE	890 mAh g ⁻¹ after 500 cycles at 2 A g ⁻¹	[185]
	Graphene trees, /	1528 mAh g ⁻¹ with 56 % CE	1021mAhg ⁻¹ after 150 cycles at 0.15A g ⁻¹	[186]
	Paper, 62 wt%	2170 mAh g ⁻¹ with 72 % CE	1390 mAh g ⁻¹ after 200 cycles at 2 A g ⁻¹	[187]

Table 6 Conducting polymers used in Si composites.

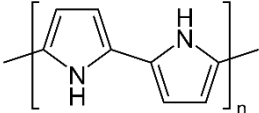
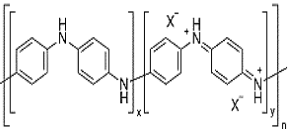
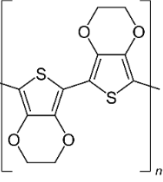
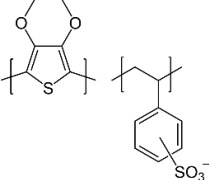
Polymers	Chemical structure	Fabrication methods	Electrical conductivity/ $S\text{ cm}^{-1}$	Functions
PPy [189–192]		Polymerization of pyrrole with FeCl_3 or $(\text{NH}_4)_2\text{S}_2\text{O}_8$ as oxidant	2-100	Conducting coating, substrate
PANi [193,195]		Mixture of aniline monomer with phytic acid	$10^{-5} - 6.7$	Conducting coating
PEDOT [196]		Electrochemical polymerization of EDOT monomer	~0.1	Conducting coating
PEDOT:PSS [197,198]		Polymerization of EDOT in a PSS aqueous solution	$10-10^3$	Conducting coating, carbon source

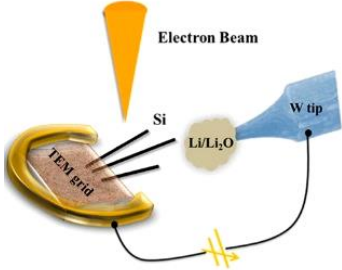
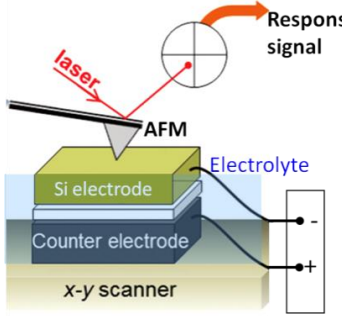
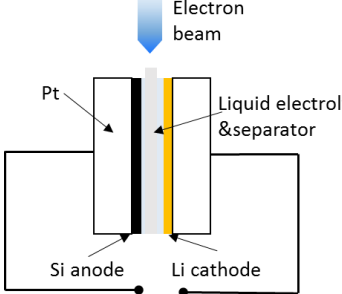
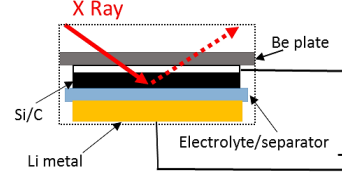
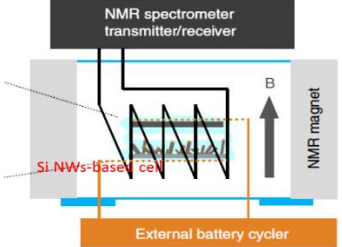
Table 7 Structures, preparation methods, Si contents and electrochemical properties of representative Si/conducting polymer composite electrodes.

Structure	Preparation, Si content	Electrochemical performance		Ref.
		1 st cycle	Cyclic capacities	
Si/PPy NPs	In-situ polymerization, 50 wt%	-	568 mAh g ⁻¹ after 10 cycles at 0.1 A g ⁻¹	[189]
Si/PPy fiber	In-situ polymerization, 34 wt%	901 mAh g ⁻¹ with 32 % CE	611 mAh g ⁻¹ after 200 cycles at 0.3A g ⁻¹	[190]
PPy/Si fiber	Electropolymerization, 70 wt%	3106 mAh g ⁻¹ with 82 % CE	2826 mAh g ⁻¹ after 100 cycles at 0.5 C	[191]
PPy/Si/CNT	In-situ polymerization, 70 wt%	2815 mAh g ⁻¹ with 78 % CE	1600 mAh g after 1000 cycles at 3.3 A g ⁻¹	[192]
Si/PANi NPs	In-situ polymerization, 75 wt%	~1250 mAh g ⁻¹ with 72 % CE	550 mAh g ⁻¹ after 5000 cycles at 6 A g ⁻¹	[193]
Si/PANi/SPA	Chemical polymerization, 70 wt%	2205 mAh g ⁻¹ with 70 % CE	950 mAh g ⁻¹ after 1000 cycles at 1.2 A g ⁻¹	[194]
Si/PEDOT	Electropolymerization, 90 wt%	3445 mAh g ⁻¹ with 89 % CE	2510 mAh g ⁻¹ after 100 cycles at 0.84 A g ⁻¹	[196]
Si/ PEDOT:PSS	Chemical polymerization, 51 wt%	936 mAh g ⁻¹ with 85.4 % CE	664 mAh g ⁻¹ after 20 cycles at 0.1 A g ⁻¹	[197]
Si/PEDOT: PSS/CNT	Gelation and filtration, 57 wt%	2180 mAh g ⁻¹ with 77 % CE	1802 mAh g ⁻¹ after 100 cycles at C/10	[198]

Table 8 Structures, Si contents and electrochemical characteristics of Si/metal (oxides) composite electrodes.

Structure	Si content	Electrochemical properties		Ref.
		1 st cycle	Cyclic capacities	
Ag/porous Si	92 wt%	2917 mAh g ⁻¹ with 81% CE	2391 mAh g ⁻¹ after 100 cycles at 0.2 C	[199]
Ag/Si NPs	97 wt%	1550 mAh g ⁻¹ with 80 % CE	1320 mAh g ⁻¹ after 100 cycles at 0.2 C	[200]
Si/Fe ₂ O ₃ /C	65 wt%	1911 mAh g ⁻¹ with 67 % CE	1980 mAh g ⁻¹ after 220 cycles at 0.75 A g ⁻¹	[202]
SnO ₂ /Si NWs	/	1.67 mAh cm ⁻² with 78 % CE	1.38 mAh/cm ² after 50 cycles at 0.38 mA/cm ²	[203]
Co ₃ O ₄ /Si NPs	60 wt%	1104 mAh g ⁻¹ with 42 % CE	850 mAh g ⁻¹ after 100 cycles at 0.1 A g ⁻¹	[204]
LTO/Si NPs	76 wt%	1032 mAh g ⁻¹ with 78 % CE	~650 mAh g ⁻¹ after 1000 cycles at 1C	[205]
Sn/Si NWs	89 wt%	90 % CE	1046 mAh g ⁻¹ after 100 cycles at 0.1 C	[206]
Si/Ge NWs	25 wt%	1255 mAh g ⁻¹ with 68 % CE	1459 mAh g ⁻¹ after 100 cycles at 0.2 C	[207]
Si/CNT/BaTiO ₃	49 wt%	2204 mAh g ⁻¹ with 86 % CE	1388 mAh g ⁻¹ after 100 cycles at 1.1 A g ⁻¹	[210]
SiO ₂ /Si NWs	/	2117 mAh g ⁻¹ with 92 % CE	1757 mAh g ⁻¹ after 50 cycles at 0.2 C	[211]
SiO _x /Si NPs	50 wt%	1914 mAh g ⁻¹ with 66 % CE	1500 mAh g ⁻¹ after 100 cycles at 0.2 A g ⁻¹	[212]
SiOC/Si NPs	84 wt%	2093 mAh g ⁻¹ with 72 % CE	1925 mAh g ⁻¹ after 200 cycles at 0.1 A g ⁻¹	[213]

Table 9 *In-situ* characterization techniques for studying Si-based electrodes. (Reprinted with permission from [234,269], Copyright 2014 ACS, 2015 Nature).

<i>In-situ</i> techniques	Set-up	Applications	Ref.
<i>In-situ</i> TEM		Lithiation mechanisms, reaction kinetics, effects of coatings and mechanical properties of lithiated Si	[224–228,233–237,239–244]
<i>In-situ</i> AFM		Formation and evolution of SEI layers, volume expansion of Si electrodes	[256–261]
<i>In-situ</i> SEM		Volume expansion of Si electrodes in real batteries for multiple cycles	[262,263]
<i>In-situ</i> XRD		Phase evolution of Si electrodes for multiple cycles	[264–266]
<i>In-situ</i> NMR		Reaction kinetics and structural evolution in real batteries for multiple cycles	[268–270]